Doctoral Dissertation

博士論文

Study of ion upflows in the low-altitude ionosphere and their effects on supply of terrestrial heavy ions to the magnetosphere

(低高度電離圏におけるイオン上昇流とそれらが磁気圏への地球起源重イオン供給に与える影響の研究)

A Dissertation Submitted for the Degree of Doctor of Philosophy
October 2022

令和 4 年 10 月博士(理学)申請

Department of Earth and Planetary Science,
Graduate School of Science,
The University of Tokyo

東京大学大学院 理学系研究科 地球惑星科学専攻

Masayoshi Takada

髙田雅康

Abstract

The space around the Earth is under the influence of the geomagnetic field and the region is called as the magnetosphere. The magnetospheric plasma originate from two source regions: the solar wind, which is the plasma flow from the Sun, and the terrestrial ionosphere, which corresponds to the layer of the ionized atmosphere ranging at the altitude from ~80 km to ~1000 km. It is important to understand the supply processes for each ion species from these regions into magnetosphere. In particular, molecular ions ($O_2^+/NO^+/N_2^+$) in the magnetosphere have been observed during the magnetic storms [Klecker et al., 1986; Seki et al., 2019] as well as atomic oxygen ions (O^+) [Daglis et al., 1999; Nose´ et al., 2005; Keika et al., 2013]. These molecular ions are supplied from the terrestrial ionosphere. The source of the molecular ions is low-altitude ionosphere (< 300 km) whereas O^+ is dominant in high-altitude ionosphere (> 400 km). These ions are transported upward in the ionosphere (ion upflow) before outflowing into the magnetosphere. Thus, understanding of properties of the ion upflows is important to reveal the supply processes of terrestrial heavy ions from the ionosphere to the magnetosphere.

The generation mechanisms of ion upflows is one of the important properties. Candidate mechanisms such as the ion frictional heating, particle precipitation, and small or large scale instabilities have been proposed and investigated for O^+ ion upflows in the high-altitude ionosphere. However, those mechanisms could not provide molecular ions with enough energy to escape overcoming the loss due to the dissociative recombination [Peterson et al., 1994] (Question 1). The dependence of the properties of ion upflows on the magnetic storms is also important. Ogawa et al. [2019] found that they have different dependences on CIR- and CME-driven magnetic storms at each magnetic local time and latitude in the polar high-altitude ionosphere. However, such dependences of ion upflows in the low-altitude ionosphere are still unknown even though many differences between low- and high-altitude ionosphere are considerable [e.g., Yamazaki et al., 2017] (Question 2). In this study, the author aim at comprehensive understanding of the ion upflows in the low-altitude ionosphere and their effects on supply of terrestrial heavy ions to the magnetosphere by solving those two outstanding questions via an event study for Question 1 and a statistical study for Question 2.

In the event study, the author analyzed an ion upflow event observed by the EISCAT radar at Tromsø on September 8, 2017 during a magnetic storm (Dst minimum ~ -100 nT). The magnetic storm started on September 7, 2017 and the Arase satellite continuously observed molecular ions in the inner magnetosphere. It means that there was a continuous supply of molecular ions during the magnetic storms. During the storm event, EISCAT observed the ion upflow in the low-altitude ionosphere. The upflow occurred with the ion velocity of more than 100 m/s and the enhancement of ion temperature and electric fields. A detailed estimation of dominant force in the transportation processes and remaining flux at higher altitude (~350 km) suggested that the ion frictional heating contributed to the rapid ion upflow, by which molecular ions could be supplied overcoming the dissociative recombination.

In the statistical study, the author investigated the effects of CIR- and CME-driven magnetic storms on ion upflows in the low-altitude ionosphere by using the long-term observational data obtained by the EISCAT radars at Tromsø and Svalbard from 1996 to 2015. The results show that ion upflows mainly occurred in dawn and nightside during both CIR- and CME-driven magnetic storms. Also, the author inferred the generation mechanisms by evaluating the enhancements of ion and electron temperatures. The results indicate that the frictional heating mainly caused upflows during CME-driven magnetic storms at both locations and possibly in dawnside during small CIR-driven storms at Svalbard and the particle precipitation mainly caused upflows during CIR-driven magnetic storms at both locations and possibly in nightside during small CME-driven storms at Tromsø.

By comparing the results from the statistical study with the previous study by Ogawa et al. [2019], this study shows the comprehensive understanding about ion upflows in the polar ionosphere during magnetic storms. In particular, the characteristics of the low-altitude ionospheric upflows leads to understandings about supply processes of molecular ions to the magnetosphere. It is concluded that the particle precipitation such as the electron precipitation with the energy of more than ~1 keV from the inner magnetosphere frequently contribute to the ion upflows around the nightside auroral oval during magnetic storms and the large magnetic storms resulted in the additional supply of molecular ions along with the enhancement of Joule heating (the frictional heating) caused by the developed convection electric fields. Even during small storms, molecular ions can be supplied from dawnside by the frictional heating and from nightside by the precipitation.

These results suggest that the magnetic storms are effective drivers of the ion escape from the collisional low-altitude ionosphere to space.

Contents

Chapter 1 General introduction

Section 1.1 The Earth's magnetosphere and ionosphere

1.1.1 Outer magnetosphere

The magnetosphere is a region where the geomagnetic field shapes the barrier to the solar wind, which is the flow of the plasma mainly composed of protons (H^+) and alpha particles (He^{++}) from the Sun. It is called the magnetosphere because the magnetic field plays a crucial role for plasma dynamics; in short, it is the sphere under the influence of geomagnetic field. The strong geomagnetic field extend ~10 Earth radii (RE) to the Sun direction and ~200 RE to the nightside shaping the cylindrical streamer. Note that, the distance is described on the magnetic equatorial plane. A plasma state or an intensity of the magnetic field can classify the magnetosphere into several areas; in particular, the outer magnetosphere is the region, where geomagnetic field unable to form dipole magnetic field due to the solar wind. The outer magnetosphere typically locate more than ~6 RE away from the Earth's surface.

Figure 1.1 represents the schematic structure of the terrestrial magnetosphere. The solar wind from the Sun, whose density is about ~10 cm^{-3} and velocity is ~400 km/s, come across the Bow Shock (~15RE) where the supersonic flow is decelerated and compressed by the magnetosphere. Then, the plasma forms the region called the magnetosheath. In the magnetosheath, there are complex state and many physical dynamics occur; for example, the magnetic reconnection and plasma instabilities [Kulsrud, 2001; Remya et al., 2013]. The solar wind completely stopped at the magnetopause (~10RE). There are many differences between dayside and nightside magnetosphere.

Inside the dayside magnetopause, there are low density plasma (~0.1 /cm^3) and the strong magnetic field which almost directs the northward and is enforced ~2 times more than in the dipole magnetic field model because the magnetic field is compressed by the effect of solar wind and there is a broad electric current across the magnetopause

called as Chapman-Ferraro current [c.f., Ghuratia et al., 2022 and there in]. The southward interplanetary magnetic field (IMF), which is the solar origin magnetic field, sometimes cause the magnetic reconnection [e.g., Burch et al., 2016].

Inside the nightside magnetopause, there is the lobe region, which consists of the very low density (~0.01 /cm^3) plasma. Inside the lobe region, the area called the plasma sheet spread out over ~6 RE. These regions are called the magnetotail. In the plasma sheet, the magnetic field is deformed from the dipole field and directs parallel to the magnetic equatorial plane. In the plasma sheet, the intensity of the magnetic field is ~5-20 nT, which is 2-4 times smaller than in the lobe region, whereas the density is ~0.1 cm^{-3}, which is ~10 times larger than there. Thus, the gas pressure gradient is in equilibrium with the magnetic pressure gradient in the magnetotail. The magnetic field is antiparallel between the north and south regions; thus, the magnetic reconnection is able to occur as in case of the dayside magnetopause. The strong flow reversal event occurs with the magnetic reconnection [Christon et al., 1994]. It is one of the important supply process of magnetospheric plasma from the outer magnetosphere into the inner magnetosphere.

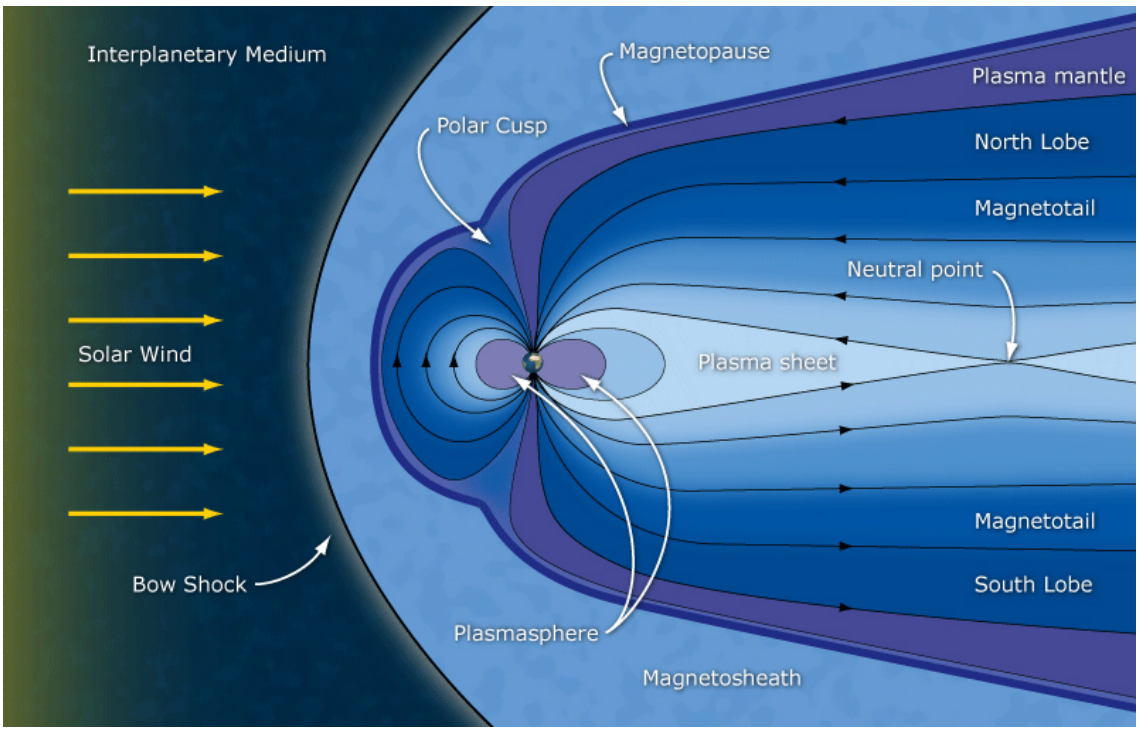

Figure 1.1: The schematic structure of the terrestrial magnetosphere [Nathan, 2014]. The outer magnetosphere is the region, where geomagnetic fields is under the effect of the solar wind and unable to form the dipole magnetic field (typically more than ~6 RE away from the earth). RE: Earth radii.

1.1.2 Inner magnetosphere

The inner magnetosphere is the region, where plasma is composed of charged particles trapped in the strong Earth's magnetic field. Figure 1.2 represents the schematic structure of the inner magnetosphere. As shown in Figure 1.2a, there are three populations of particles in three areas: Van Allen radiation belts, the plasma sphere, and the ring current. The most remarkable difference among those particles is involved in their energies. Figure 1.2b shows the more specific structures of the inner magnetosphere. There are many factors to cause the difference; for example, the source region of plasma, the diffusion process, and the interaction between waves and particles and so on.

In the inner magnetosphere, *L*-value (with distance measured in the Earth radii) is useful for representing the distance from the Earth because of the valid geomagnetic field as dipole magnetic field. *L*-value is defined as

$$L = \frac{1}{\cos^2(\Lambda)} \tag{1.1.1}$$

where Λ is the latitude of the point at which the magnetic field line intersects the Earth's surface.

The plasmasphere is the region, which consist of dense (~10^1-10^3 /cm^3) and cold (~1 eV) plasma. There are two distinctive motions around the plasmasphere: the co-rotational motion by convective electric field and the magnetospheric convection. Figure 1.3 shows the equipotential contour lines and arrows corresponding to the plasma flow velocity in the magnetic equatorial plane. The combination of two motions created the unique streamlines and the co-rotational motion is predominant in the plasmasphere. The boundary layer is called the plasmapause, where hot plasma exists which comes from the outer radiation belt or ring current. Depending on the magnetic local time (MLT) and magnetic activities, the position of the plasmapause change. The plasmapause is located at L~2 during magnetically active time whereas it is located at L~7 during magnetically quiet time [c.f., Ebihara and Miyoshi, 2011].

Van Allen radiation belts consist of the energetic electrons and ions from ~100 keV to ~10 MeV which is the highest energy particles in the magnetosphere. The electron radiation belts are divided into inner (*L*~1-2) and outer region (*L*~4-6). The proton radiation belt is a region which locates between the electron radiation belts.

The ring current region (L~3-6) is the intermediate region between the

plasmasphere and the radiation belts, which means there is moderately energized plasma (~1-100 keV). Figure 1.4 represents the schematic structure of the distinct regions and electric current systems in the magnetosphere. In the ring current region, the westward current exists caused by the curvature drift and pressure gradient associated with the geomagnetic disturbance. The "ring current" is named after the particle circular motions, which cause the westward current. Not only protons and alpha particles but also heavy ions such as O^+ and even molecular ions (O_2^+, NO^+ and N_2^+) are observed together with the westward electric currents in the region [e.g., Nose´ et al., 2005; Seki et al., 2019]. These molecular ions are transported into the ring current along with the geomagnetic disturbance phenomena such as substorms and magnetic storms [Daglis et al., 1999]. The relationship between the development of the ring current and substorm/magnetic storms is introduced in more detail in Section 1.1.4.

The ring current is important in terms of the evolutions of field aligned currents. There are signature field aligned currents called as Region 1 and Region 2 field aligned currents. Figure 1.5 is cartoon illustrations about the locations of Region 1 and Region 2 field-aligned currents. Region 1 field aligned currents flow into (out of) the polar and high-latitudinal (~70°-80°) regions on the Earth in dawnkside (duskside) from (to) the magnetosphere. Region 2 field aligned currents flow into (out of) the polar and low-latitudinal (~60°-70°) regions on the Earth in duskside (dawnside) from (to) the magnetosphere. In particular, the ring current, which often partially develop in duskside, directly connects with Region 2 field aligned currents, while Region 1 field aligned currents close across the magnetopause [c.f., Ganushkina et al. 2015; Milan et al., 2017].

(a)

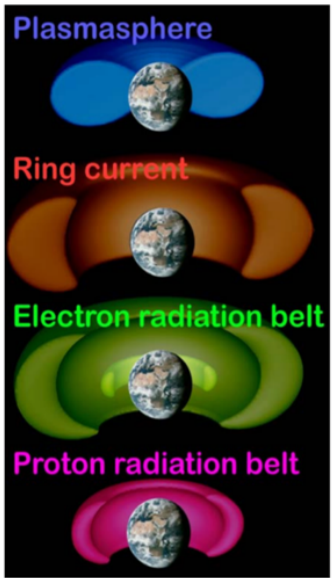

(b)

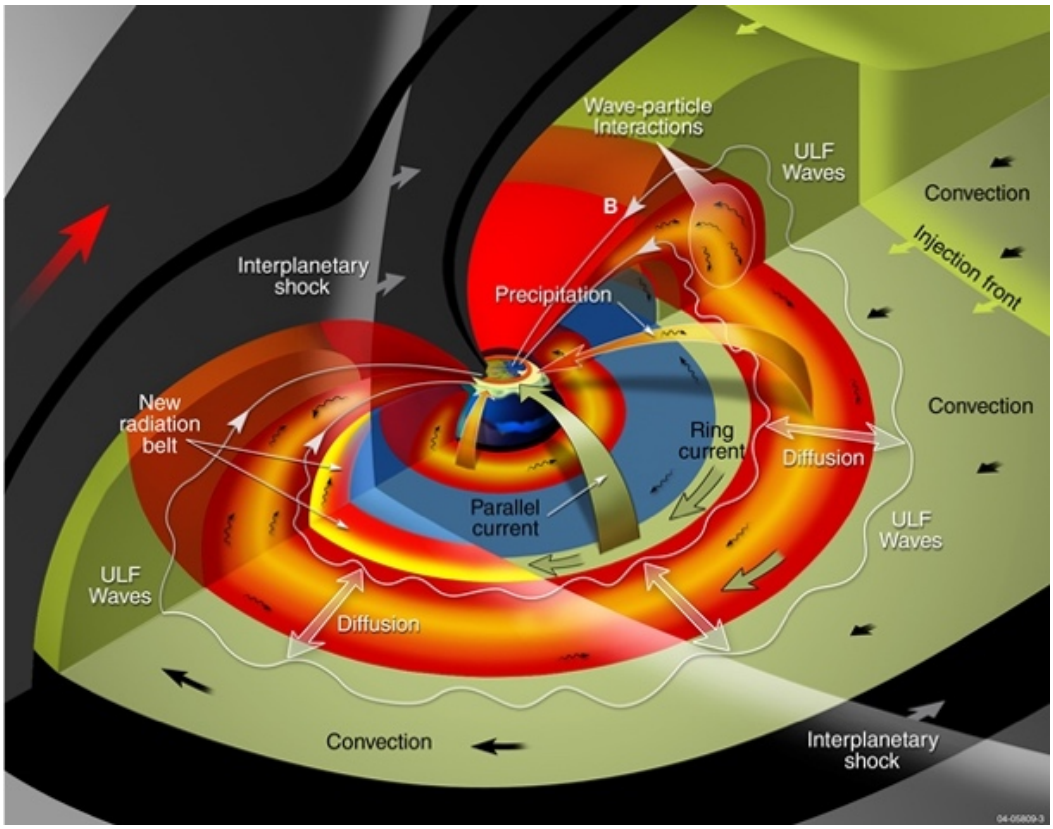

Figure 1.2: The schematic structure of the inner magnetosphere: (a) the overview [Ebihara and Miyoshi, 2011] and (b) the detail [https://ccmc.gsfc.nasa.gov/RoR_WWW/support/UAH_2013/Zheng_innermag_UAH.pdf].

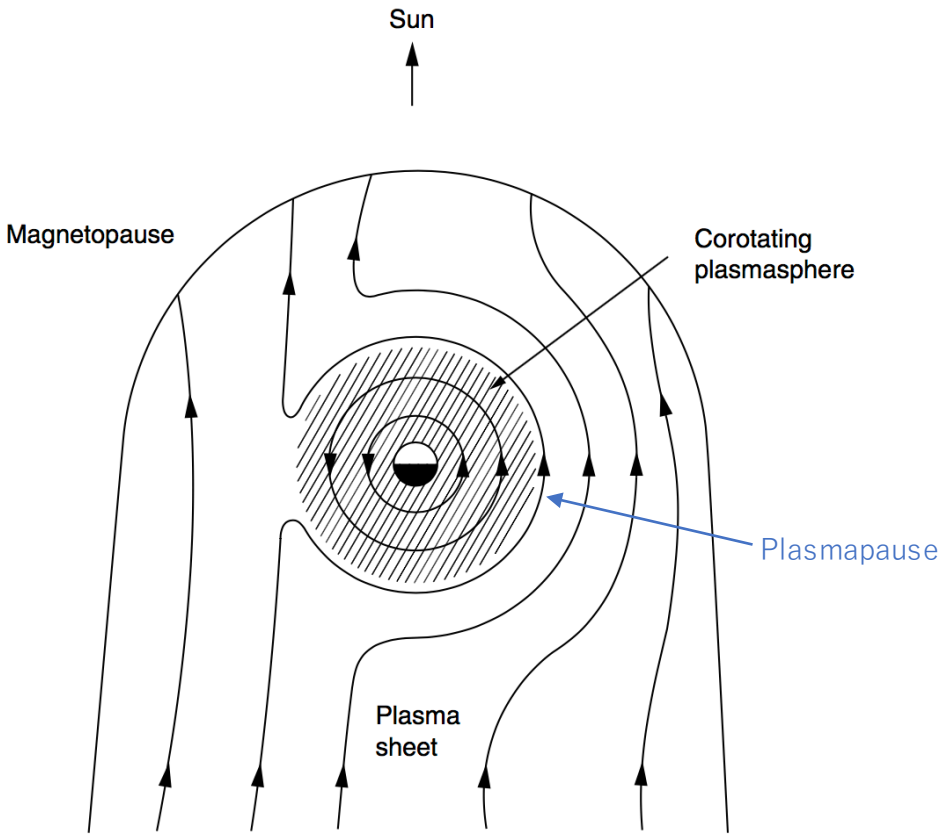

Figure 1.3: Equipotential contours and the streamline of plasma flow in the magnetic equatorial plane. The lines represent the contours and arrows represent the streamline. The flow pattern around the plasmasphere is not quite so simple due to the co-rotating motion. [modified from Figure 8.6 in Kelley, 2009]

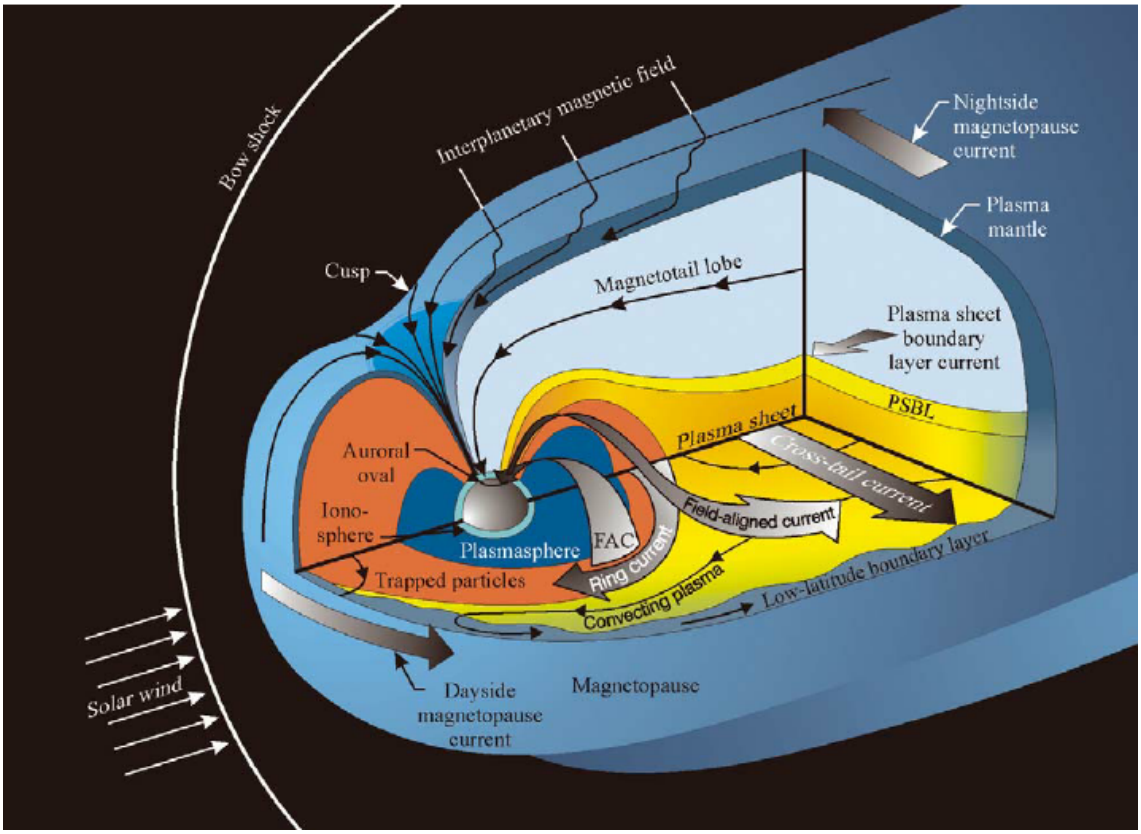

Figure 1.4: Schematic structure of the distinct regions and electric current systems in the magnetosphere [Pollock et al., 2003]. In particular, the ring currents in duskside notably develop during geomagnetic disturbance periods and the evolutions of fields aligned currents (FAC) are remarkable.

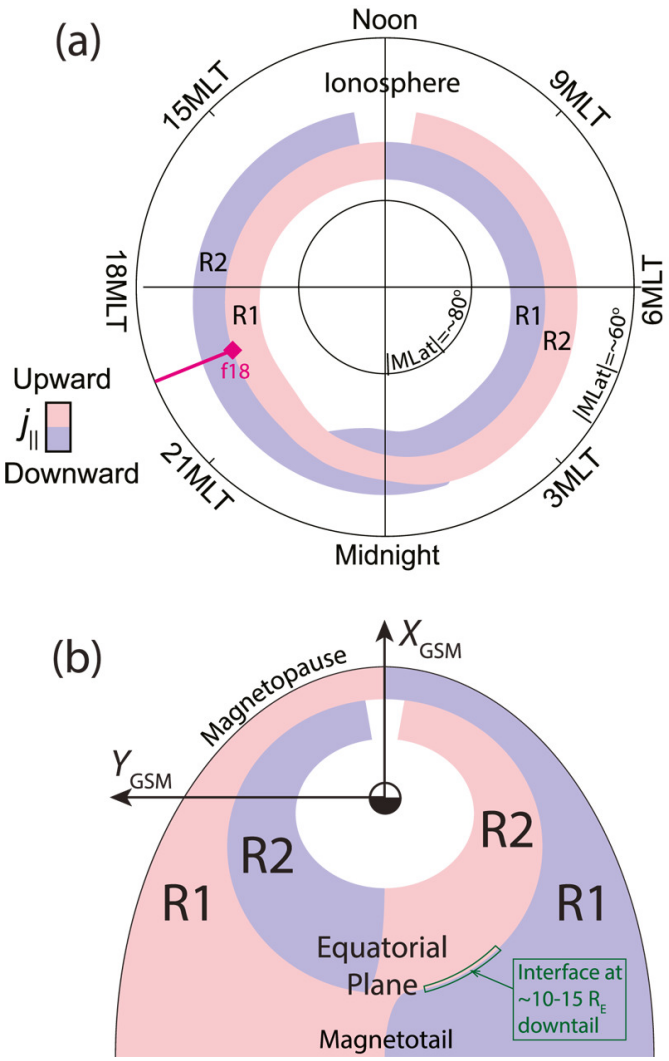

Figure 1.5: Cartoon illustrations about the locations of Regions 1 and Region 2 currents [Liu et al., 2021]. Light red/blue regions represent the upward/downward currents, that is, (a) flows out of / into the Earth and (b) flows to/from the magnetosphere. MLT: Magnetic Local Time; GSM: Geocentric Solar Magnetospheric coordinates.

1.1.3 Ionosphere

The ionosphere is an upper region of the Earth's atmosphere from ~80 to ~1000 km. It contains a high concentration of ions and electrons (>10^4 /cm^3). The component of the plasma is determined for each altitude. Figure 1.6 represents the typical density profile in the ionosphere under the geomagnetic quiet condition; proton (H^+) is the dominant component at the highest altitude (~1000 km); atomic oxygen ion (O^+) is the dominant component at the middle altitude (200-1000 km); molecular ions (O_2^+/NO^+) are dominant at the lowest altitude (~100 km). The neutral density is also remarkable in the low-altitude ionosphere (> ~10^8 cm^{-3}). It is considered that the ion composition change during geomagnetic disturbance periods such as magnetic storms. Figure 1.7 shows the density profile based on the International Reference Ionosphere (IRI) model [Bilitza et al, 2016] in the duskside ionosphere at Tromsø. Molecular ions are dominant at the altitude of more than 200 km and even at ~250 km. However, it is also considered that molecular ions rapidly decrease above 300 km because molecular ions undergo fast dissociative recombination reactions caused by the high electron concentration around the ~300 km altitude [c.f., Lin and Ilie, 2022].

The region between ~100-400 km is divided into three layers: D, E, and F (F1/F2) layer. The electron density change in each layer. Figure 1.8 shows the overview of the ionospheric electron density. The electron density in the ionosphere has several peaks. In particular, there are two peaks in the F layer in the dayside ionosphere called F1 and F2 layer. The nightside ionosphere is different from the dayside and has only one peak in the F layer due to low injection of the solar Extreme Ultraviolet (EUV). In other words, the efficiency of the ionization in the nightside is lower than dayside and the F layer is not separated into two layers. The electron density change due to the seasonal variations and solar activities as well because the efficiency of the ionization depends on them [e.g., Liu et al., 2009; Yamazaki et al., 2017].

We can define the polar ionosphere as four regions related to the magnetospheric structures: the cusp, polar cap, auroral oval, subauroral zone. Figure 1.9 shows the schematic drawing of the polar ionosphere. The cusp is the region where no geomagnetic field exists. Geomagnetic fields are separated between sunward and tailward magnetic fields at the cusp. The polar cap connects the open magnetic flux tube in the magnetosphere [Sergeev., 1990]. Around the auroral oval, energized particles (~ 0.1-

10keV) originating from the magnetosphere inside the closed magnetic fields boundary often precipitate and auroral brightening are detected. Note that, it is an important property that the auroral oval expands during magnetic storms [e.g., Xiong et al., 2014]. The subauroral zone locate at lower latitude than auroral oval and affected by the dynamics of the inner magnetosphere such as the ring current. Thus, the westward convection flow called Subauroral Polarization Stream (SAPS) is often observed in the duskside of the subauroral zone [c.f., Foster and Vo, 2002; Kataoka et al., 2017]. SAPS is the westward flow resulting from the $E\times B$ drift caused by enhanced global electric fields and often generated in the duskside ionosphere; the velocity reached > ~1 km/s. SAPS is closely related to the ring current and play important role to energize and transport ions into the subauroral zone.

The convective electric fields exist in the ionosphere. There are two kinds of conductivities in the perpendicular direction to the magnetic field. One is the Pedersen conductivity

$$\sigma_P = ne^2\left(\frac{\frac{\nu_{en}}{m_e}}{\nu_{en}^2+\omega_{ce}^2}+\frac{\frac{\nu_{in}}{m_i}}{\nu_{in}^2+\omega_{ci}^2}\right) \tag{1.1.2}$$

and the other is Hall conductivity

$$\sigma_H = ne^2\left(\frac{\frac{\omega_{ce}}{m_e}}{\nu_{en}^2+\omega_{ce}^2}-\frac{\frac{\omega_{ci}}{m_i}}{\nu_{in}^2+\omega_{ci}^2}\right) \tag{1.1.3}$$

where n is density; e is the elementary charge; m_e and m_i are mass, ω_{ce} and ω_{ci} are cyclotron frequency, ν_{en} and ν_{in} are collisional frequency of electron and ion. Now, ν_{en} is given by

$$\nu_{en} = 5.4\times10^{-10}n_nT_e^{0.5} \tag{1.1.4}$$

where n_n is the neutral density and T_e is the electron temperature and ν_{in} is given by

$$\nu_{in} = 2.6\times10^{-15}(n_n+n)m_n^{-0.5}\,. \tag{1.1.5}$$

where m_n is a neutral mass.

In general, collisional effects change at each altitude. The ion (electron) cycrotron frequency and collisional frequency are almost same at ~110 (~80) km in the auroral zone such as Tromsø [c.f., Brekke, 2013]. Below the altitudes, collisions are dominant and only thermal effects determine ion and electron motions. In the D layer (< ~100 km), ions, electrons and neutrals frequently collide and temperatures for all species

are almost same. In the E layer (< ~200 km), ions and neutrals frequently collide but electrons can move separately, thus the electron temperature is different from those species. In the F layer (< ~400 km), ions and neutrals can collide but the effect of collisions become less at the higher altitudes. Above the region (> ~400 km), ions and neutrals can move separately. Figure 1.10 shows the examples of the ionospheric altitude profiles at Tromsø. Pedersen conductivity is effective between 100-300 km whereas Hall conductivity has the steep peak at ~110 km for electrons as shown in Figure 1.10d. There is a different dependence of the Pedersen conductivity for each ion species (See Figure 1.10e). Collisional frequency also has different characteristics for ions in Figure 1.10f.

These conductivities cause the horizontal currents at the different altitudes. In particular, the large-scale convective electric field cause the convection motions in the wide area in the polar ionosphere during geomagnetic disturbance periods and the convection flow is known as two-cell convections. Figure 1.11 represents the distributions of two-cell convections and related electric fields in the polar ionosphere. The developments of these convective electric fields are closely involved in the evolutions of the Region 1 and 2 field aligned currents [c.f., Figure 1.5].

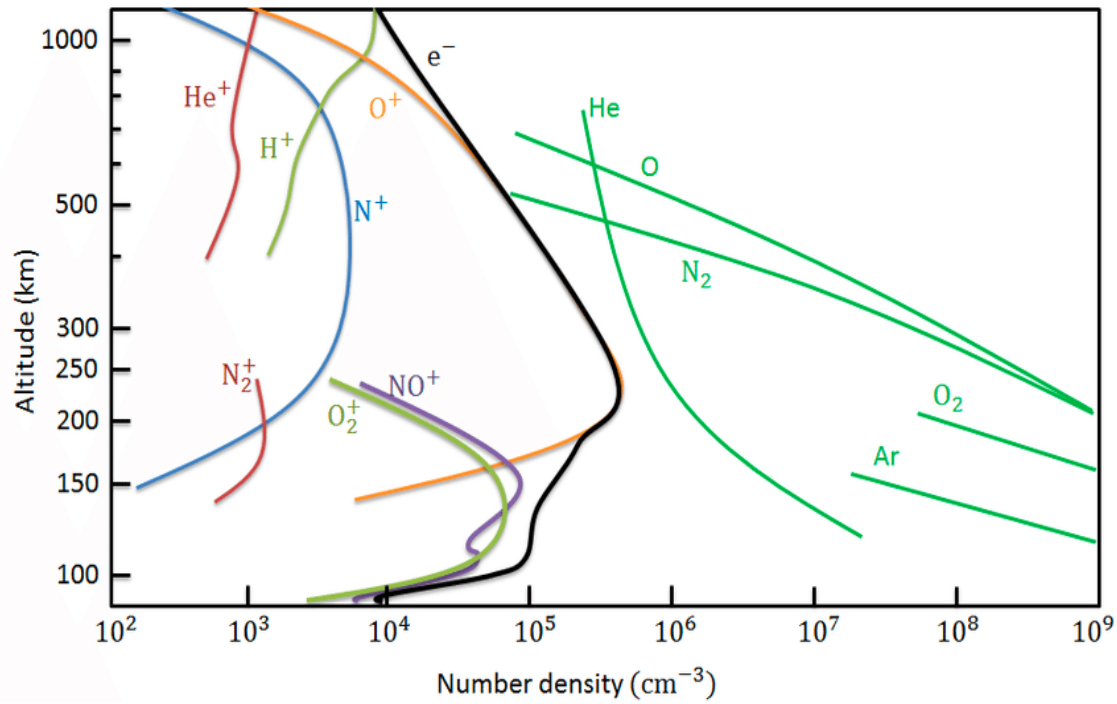

Figure 1.6: The typical density profile in the ionosphere under the geomagnetic quiet condition [Kelly, 1989 and reproduced by Akbari, 2015].

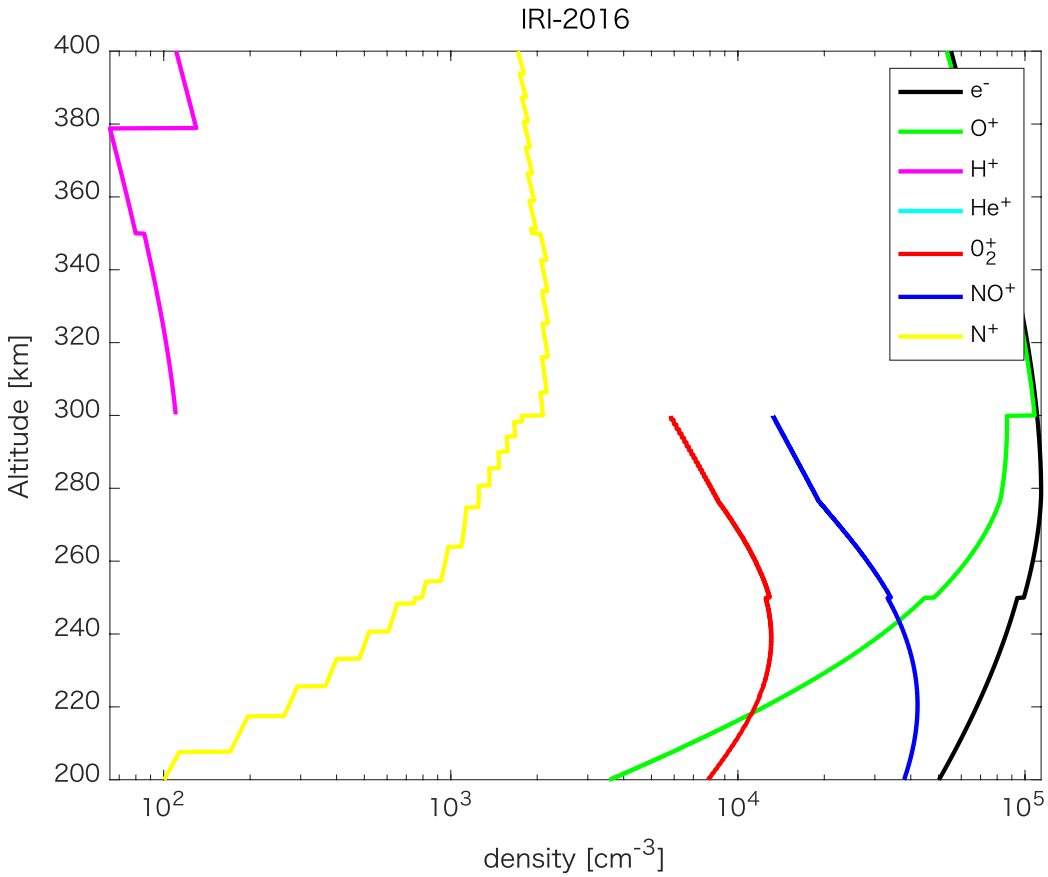

Figure 1.7: The density profile in the duskside ionosphere at Tromsø (Invariant Latitude: 66°12′ N) derived from the IRI model during a magnetic storm, which started on September 7, 2017. Each line represents the density profile of electron (black), atomic oxygen ion (green), atomic hydrogen ion (purple), atomic helium ion (light blue), molecular oxygen ion (red), nitric monoxide ion (blue) and atomic nitrogen ion (yellow). The molecular ions are dominant at the altitude of ~250 km. IRI model: International Reference Ionosphere model.

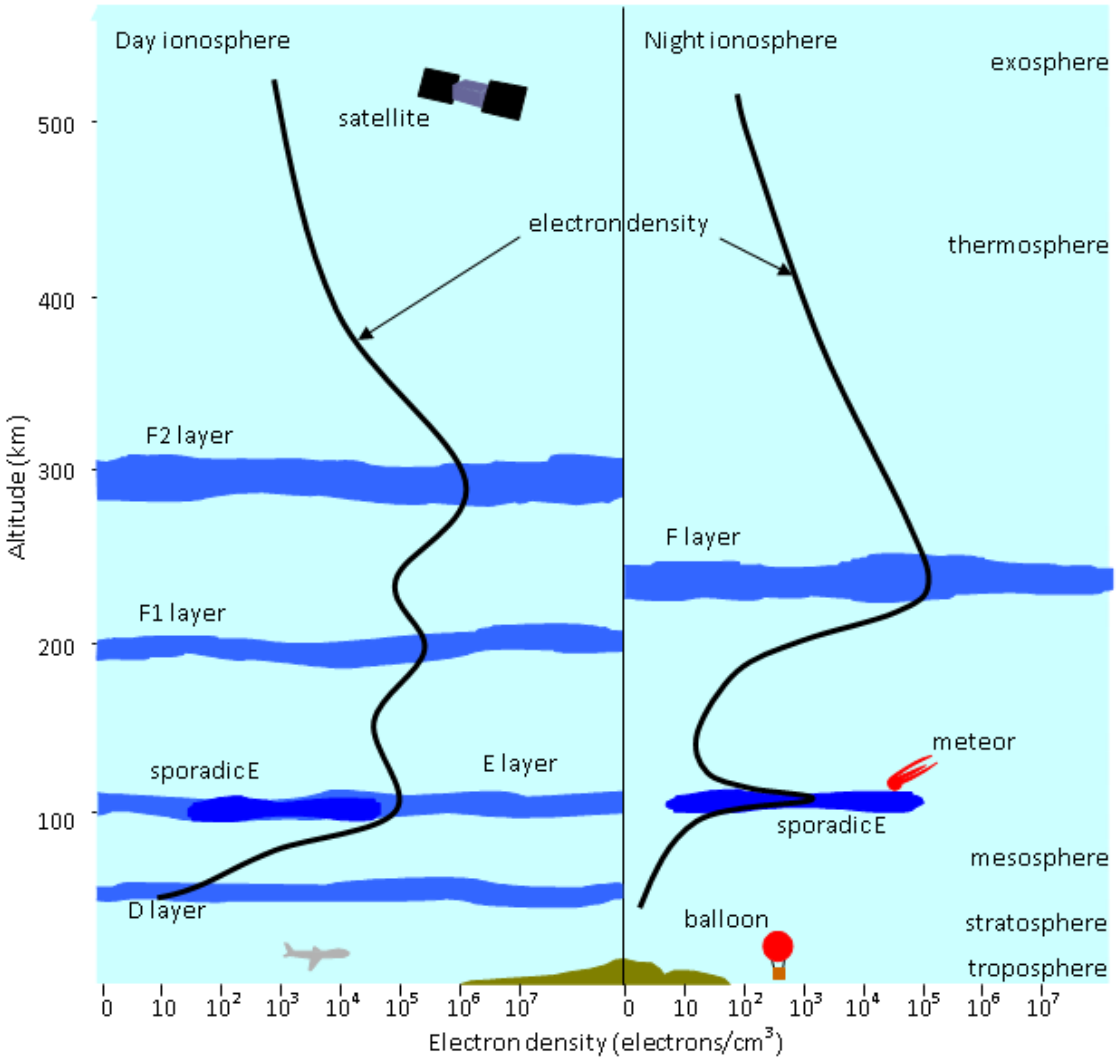

Figure 1.8: An overview of the electron density in the bottom ionosphere [https://www.sws.bom.gov.au/Educational/1/2/5]. There are peaks in the E and F (F1 and F2) layer in the nightside (dayside) ionosphere.

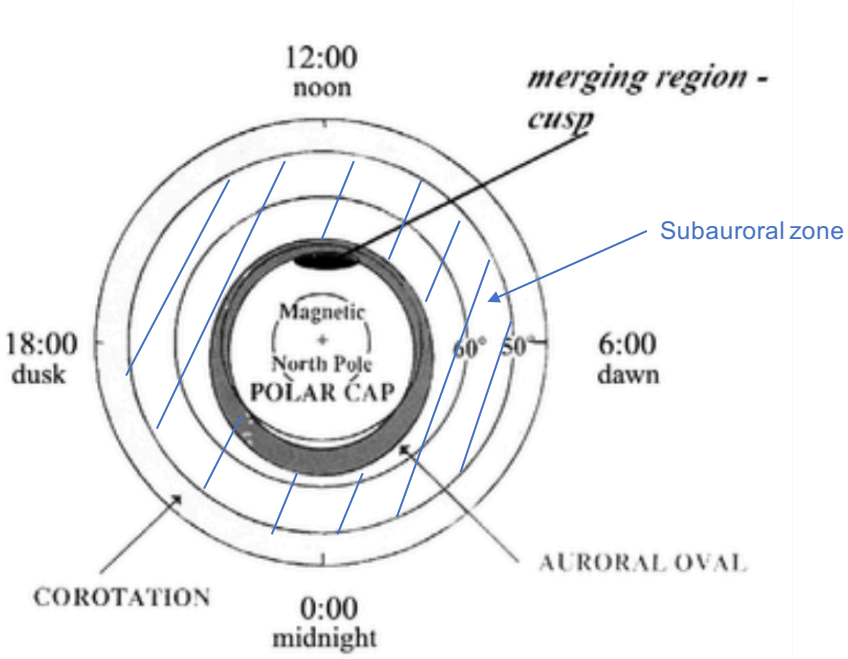

Figure 1.9: Schematic drawing about the terrestrial polar ionosphere [modified from Figure 1a in Hui et al., 2010]. There are four particular regions in the polar ionosphere: the cusp, polar cap, auroral oval, and subauroral zone.

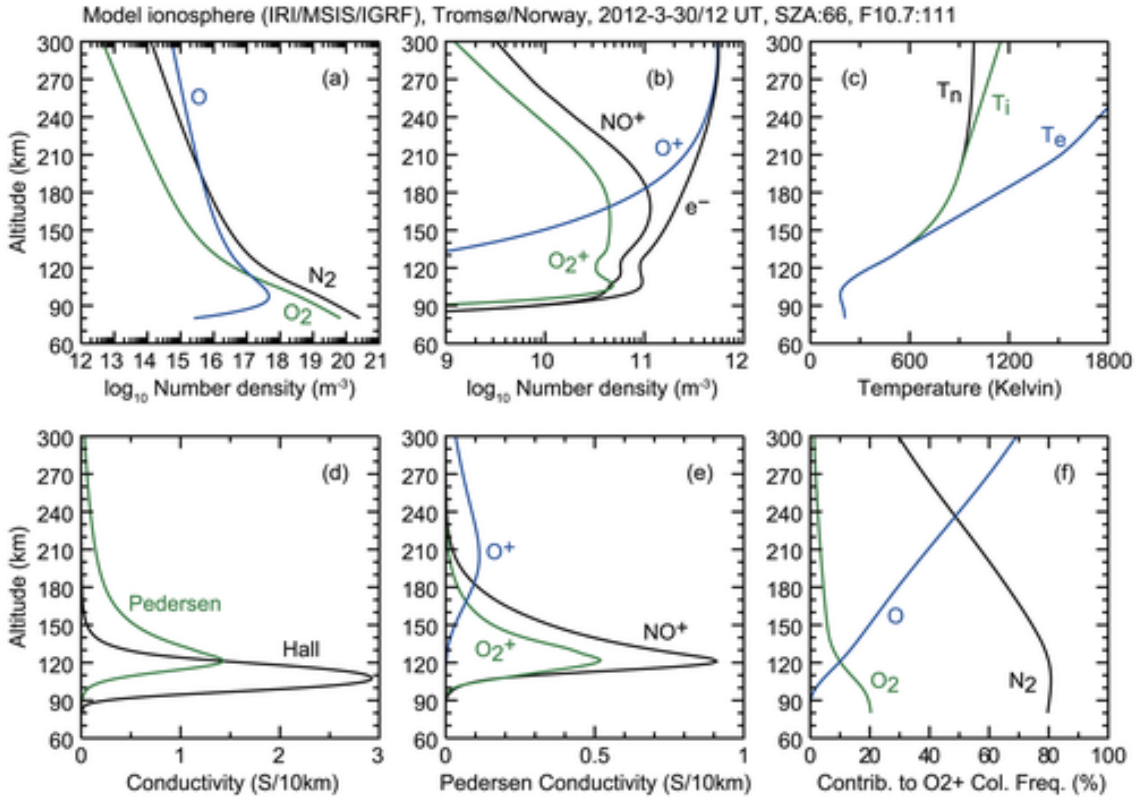

Figure 1.10: Examples of altitude profiles of model ionosphere at Tromsø (Invariant Latitude: 66°12′ N) [Ieda, 2019]. Each panel shows the result based on the IRI 2016 and MSIS model at 12 UT on 30 March 2012: (a) Number densities of neutral atmosphere (N_2, O_2, and O); (b) Number densities of ions (NO^+, O_2^+, and O^+) and electrons; (c) Neutral, ion, and electron temperatures; (d) Electric conductivity (Hall and Pedersen components); (e) Ion components (NO^+, O_2^+, and O^+) of the Pedersen conductivity; (f) Relative contribution of N_2, O_2, and O to the O_2^+ collision frequency. IRI model: International Reference Ionosphere model, MSIS model: Mass Spectrometer and Incoherent Scatter model.

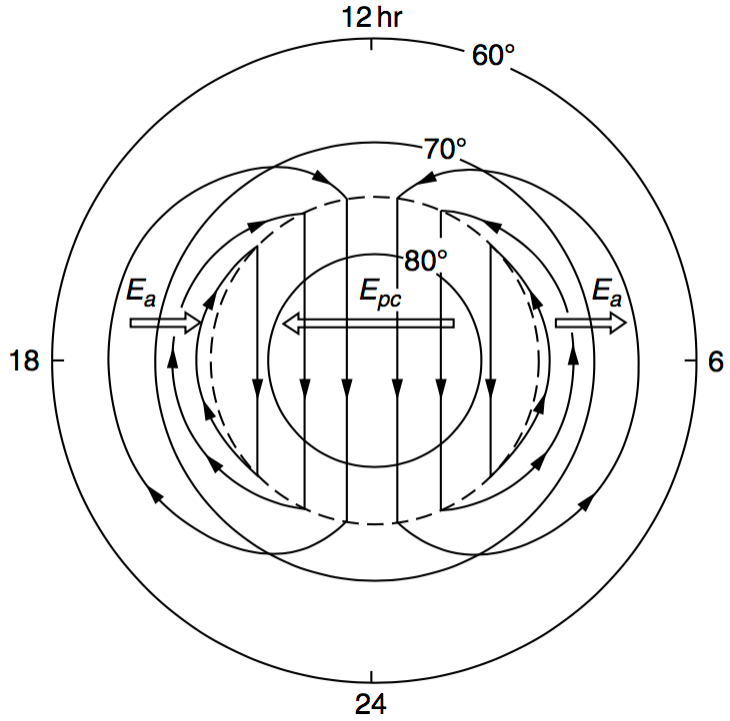

Figure 1.11: Representation of two-cell convection electric fields in the polar ionosphere [Kelley, 2009]. The lines and arrow show the streamline of convection flow. *Epc* is the electric fields in the polar cap and *Ea* is electric field in the auroral zone. The developments of these electric fields are related to the evolutions of Region 1 and 2 field aligned currents (c.f., Figure 1.5).

1.1.4 Magnetic storms and Substorms

The magnetic storm is disturbance of the geomagnetic field. It is defined by the Disturbance storm time (Dst) index:

$$Dst = \frac{1}{N}\sum_{n=1}^{N}\frac{H - H_q}{[\cos\varphi]} \tag{1.1.6}$$

where H is the horizontal component of the magnetic field observed by each mid/low latitude observatory which locates the magnetic latitude of φ and H_q is in the quiet time, $[\cos\varphi]$ is an average value of the $\cos\varphi$, N is the number of the observatories. Dst index is able to divide the magnetic storm into three steps: the initial phase, main phase and recovery phase. Dst index slightly increase in the initial phase and decrease rapidly in main phase. After the minimum value of Dst index, Dst index is increasing and return to the quiet conditions during the recovery phase. These characteristics are strongly related to the evolution process of the ring current because the developed westward current affect the Dst index. There is no generally particular and definitive value of minimum Dst index to define a magnetic storm, but the magnetic storm is often defined as the geomagnetic disturbance phenomena which have the above characteristics in time series of Dst index.

Auroral Upper (AU), Auroral Lower (AL), Auroral Electrojet (AE) and Auroral Oval (AO) indices are also good evidences of the magnetic storm. These parameters are defined based on the observational geomagnetic fields at 12 ground-based stations, which set apart in the high-latitude region (See Table 1.1). AU/AL index is the maximum/minimum variance among these stations when the northward direction is positive; thus, AU/AL index represents the variation of the eastward/westward electric current jet. AE and AO indices are defined as

$$AE = AU - AL \tag{1.1.7}$$

and

$$AO = \frac{(AU + AL)}{2}\ . \tag{1.1.8}$$

During magnetic storms, these indices strongly fluctuate; in particular, AE index reaches several thousand nT because it reflects the electric current jet associated with the development of the auroral brightening in the ionosphere. Figure 1.12 is an example of those indices during magnetic storm. Figure 1.12a represents the time variations of Dst

index in September, 2017. It is understood that magnetic storm started on the September 7, 2017 and continued for 4 or 5 days. Figure 1.12b represents the time variations of AU, AL, AE, and AO indices on September 8, 2017. In particular, AE index fluctuated between 1000 and 2000 nT every one hour around the Dst minimum, which means the strong geomagnetic disturbance continuously leads to evolution of the auroral electro jet and brightening in the main phase.

The substorm is often described as the fundamental unit of geomagnetic disturbance and frequently occurs during the magnetic storms, while the problem remains in the way to define as a formula. If we treat the substorm as the injection together with development of the ring current, the transportation process in the magnetosphere is described as below. When a substorm happens by some disturbance phenomena such as magnetic storms and simply southward IMF, the plasma which originates from the solar wind or the ionosphere is injected to the inner side of the magnetosphere by the magnetospheric convection from the magnetotail. The detailed transportation processes from those regions will be described in Section 1.2. The plasma composes the ring current and disturbs the geomagnetic field. If the disturbance is strong enough to inject more plasma continuously, the next substorm happens and transports plasma into inner magnetosphere. Such kind of substorms are called as the magnetospheric substorms. Simultaneously, the energy from the magnetospheric disturbance develop the significant electric currents in the polar ionosphere such as Region1 and Region2 field-aligned currents, and auroral electro jet along with geomagnetic disturbances. The development of such current systems causes particle precipitations in the polar ionosphere and the precipitations generate the aurora in the longitudinally wide area. Thus, the substorm onset can be defined as the longitudinally extended sudden auroral brightening [e.g., Ieda et al., 2018]. Such kind of substorms are called as auroral substorms and substorms are often defined as the auroral substorms by the auroral brightening or AE index.

There are two types of magnetic storms driven by different drivers: Corotating Interaction Region (CIR)-driven and Coronal Mass Ejection (CME)-driven magnetic storms. During a CIR-driven storm, the rotating IMF cause the geomagnetic storm, which is related to the velocity shear between the relatively slow solar wind in the interplanetary space and the fast flow coming from the coronal hole. The moderate geomagnetic activities continue over several days and substorms frequently occur because the magnetic field is incessantly disturbed in the coronal hole.

During a CME-driven storm, magnetized plasma injects into the interplanetary space from the Sun. The fast CME make the shock front and it is one of the source of the protons which is accelerated and permeate into the magnetosphere via the magnetic reconnection driven by the strong southward IMF. Dst index tend to be smaller value during the CME-driven storm than during the CIR-driven storm; in short, large magnetic storms often occur and the ring current develops well during CME-driven storms. There are many other differences between CIR- and CME-driven magnetic storms [c.f., Borovsky and Denton, 2006].

Table 1.1: List of AE (12) Stations [https://wdc.kugi.kyoto-u.ac.jp/aedir/ae2/AEObs.html].

Observatory	IAGA Code	Geographic Coord.		Geomagnetic Coord.	
		Lat.(°N)	Long.(°E)	Lat.(°N)	Long.(°E)
Abisko	ABK	68.36	18.82	66.04	115.08
Dixon Island	DIK	73.55	80.57	63.02	161.57
Cape Chelyuskin	CCS	77.72	104.28	66.26	176.46
Tixie Bay	TIK	71.58	129.00	60.44	191.41
Cape Wellen	CWE	66.17	190.17	61.79	237.10
Barrow	BRW	71.30	203.25	68.54	241.15
College	CMO	64.87	212.17	64.63	256.52
Yellowknife	YKC	62.40	245.60	69.00	292.80
Fort Churchill	FCC	58.80	265.90	68.70	322.77
Poste-de-la-Baleine	PBQ	55.27	282.22	66.58	347.36
Narsarsuaq (Narssarssuaq)	NAQ	61.20	314.16	71.21	36.79
Leirvogur	LRV	64.18	338.30	70.22	71.04

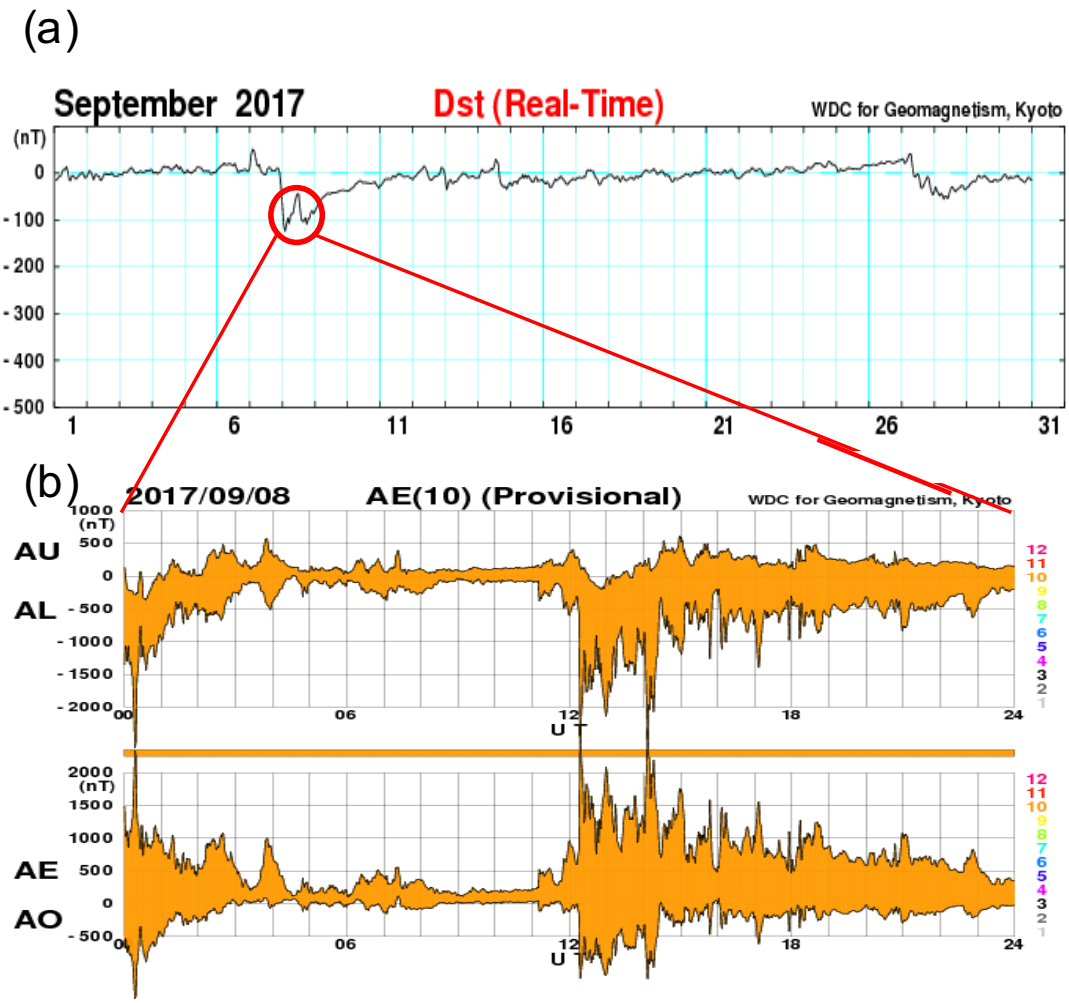

Figure 1.12: (a) Dst indices in September, 2017; (b) the AU and AL / AE and AO indices on September 8, 2017. Available data set was prepared by World Data Center for Geomagnetism, Kyoto. Dst and AE indices are good parameters to describe the magnetic storm and substorms.

Section 1.2 Source of magnetospheric ions

1.2.1 Solar wind origin ions

Solar wind is one of the important source regions for magnetospheric plasma. Solar wind ions consist almost protons (~ 96%) and alpha particles (~ 4%) [Wurz, 2005]. The heavy ions such as O^{6+} are extremely minor component and rarely detected in the solar wind. These ions are mainly transported from the magnetotail into inner magnetosphere via some transportation processes along with magnetic reconnections: plasma injections, development of field-aligned currents, and the plasmoid [Sergeev et al., 1996; Milan et al., 2017]. Figure 1.13 represents the schematic diagram of the transportation process by the magnetospheric convection from the solar wind into the magnetosphere. In the Magnetohydrodynamics (MHD) scheme, ions frozen-in the magnetic field from the solar wind are transported to the tail region and penetrate into magnetosphere via magnetic reconnection. After that, ions moved earthward by the $E \times B$ drift. In addition to that, ions precipitate directly from the dayside magnetosheath into the ionosphere along the open magnetic field involved in the southward IMF [Woch and Lundin, 1992].

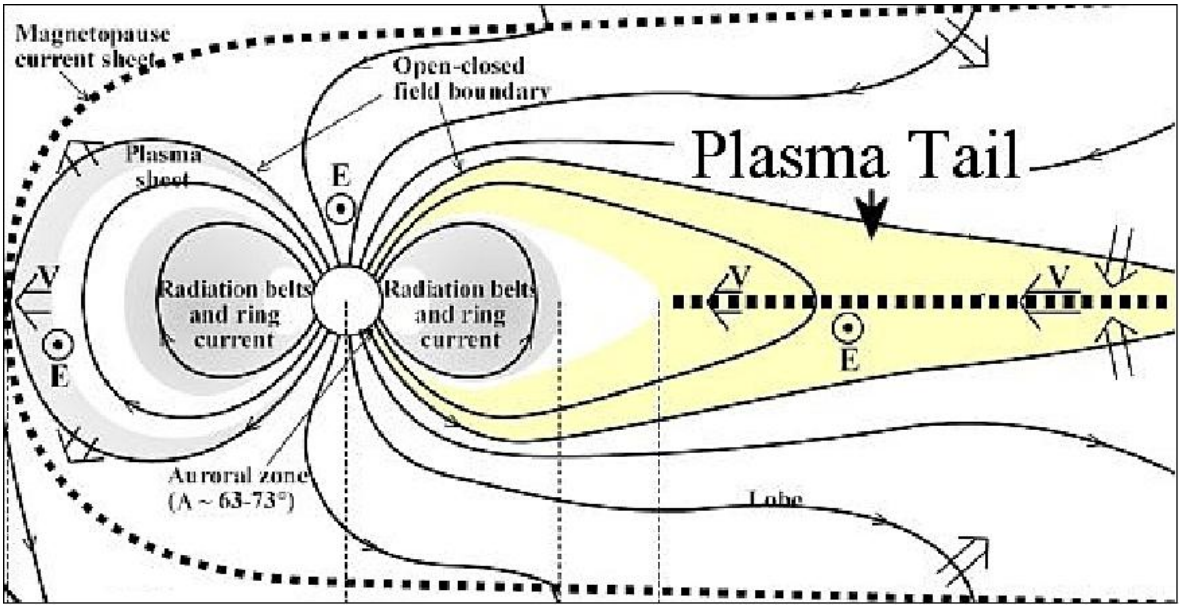

Figure 1.13: Schematic diagram of the plasma transportation by the convection flow in the magnetosphere [http://www.xearththeory.com/images/spacequakes/earths-plasma-tail-spacequakes-circuit-magnetosphere-diagram.jpg]. Ions and electrons are mainly supplied from the magnetotail to inner magnetosphere.

1.2.2 Terrestrial ions

The other source of magnetospheric plasma is the ionosphere. As introduced in Section 1.1.3, not only protons (H^+) but also heavy ions such as atomic oxygen (O^+) and molecular ions (NO^+/O_2^+) composed ionospheric plasma. These heavy ions once escape from the top side ionosphere into the magnetotail and mostly composed magnetospheric heavy ions especially during magnetic storms. After mixing with solar wind origin ions as collisionless plasma and transportation from the tail region, heavy ions from the ionosphere are finally supplied into the inner magnetosphere and often observed as the component of the ring current. The first escape process from the ionosphere into the magnetosphere is called “ion outflow”.

The ion outflow is the ion upward flow observed in the top side ionosphere. The ions are accelerated by at least the same order velocity of the escape velocity (~10 eV) to supply heavy ions into the magnetosphere against the gravitational force. Several candidate mechanisms to escape are classically categorized in terms of the region where ion outflow occur and characteristics of ion velocity [Yau and Andre, 1997]: Polar wind (PW), ion beam, ion conic, transversely accelerated ion (TAl), and upwelling ion (UWl), and Auroral Bulk outflow (AB).

The polar wind is the low energy bulk outflow (~1eV for H^+ and ~10 eV for O^+) and become faster at the higher altitude. PW is driven by hydrodynamics force such as the ambipolar electric fields and ion pressure gradient near open magnetic field line around the polar cap. Oxygen ions compose the polar wind as well as proton and helium ions.

The ion beam and conic, which are kind of ion outflow with strong and narrow peak at the energy of ~10-1000 eV in the phase space density, are also important mechanisms to supply heavy ions into the magnetosphere. The ion beam is ejected into the parallel direction to the magnetic field, while the conic is not into just a parallel direction but almost along the magnetic field line. The parallel electric field can cause the ion beam. The ion conics are caused by the transverse ion heating such as the particle precipitation or the resonance between waves and particles.

TAI has the same energy as the ion conic but peak pitch angle close to the direction of perpendicular to the magnetic field. The ion conic is sometimes interpreted as TAI resulted from the transportation with accelerations by magnetic mirror forces.

UWI causes the asymmetry towards the magnetic field in the phase space density. The UWI is not completely distinct from the TAI because the peak energy is almost same and the distribution is overlapped. The difference between UWI and TAI is mean velocity. UWI has the faster upward mean velocity than TAI.

AB occur in the bottom side ionosphere and include heavy atomic and molecular ions; thus, it is often associated with the ion upflow process (See Section 1.3). It is caused by some heating mechanisms such as the ion frictional heating and particle precipitation [c.f., Section 1.3.2 in detail].

There are many observations and studies for terrestrial O^+ ions both in the ring current and ion outflow [e.g., Daglis et al., 1999; Nose´ et al., 2005; Keika et al., 2013; Shelley et al., 1972; Yau et al., 1997; André et al., 1997; Ogawa et al., 2008]. In fact, the O^+ ions observed as a main component in the ring current during magnetic storms [e.g., Nose´ et al., 2005]. Also, molecular ions compose the magnetospheric plasma via the same escape process as O^+ ions from the top side ionosphere. However, the observations of molecular ions are very limited due to the small amount for composition. Figure 1.14 shows the observational result on molecular ions in the magnetosphere during a magnetic storm reported by Klecker et al. [1986]. Figure 1.14a shows the count number of each ion species and the Figure 1.14b shows the ratio of molecular ions to O^+. From these results, it is revealed that molecular ions can be actually supplied into the magnetosphere during storm time but the ratio of molecular ions to the O^+ reached several percentage, which means the molecular ions are very minor component to H^+, He^{2+}, and O^+. This result is just one example of the classical reports but many observational facts on molecular ions shows the scarcity of molecular ions [Lin M-Y and Ilie R, 2022 and there in].

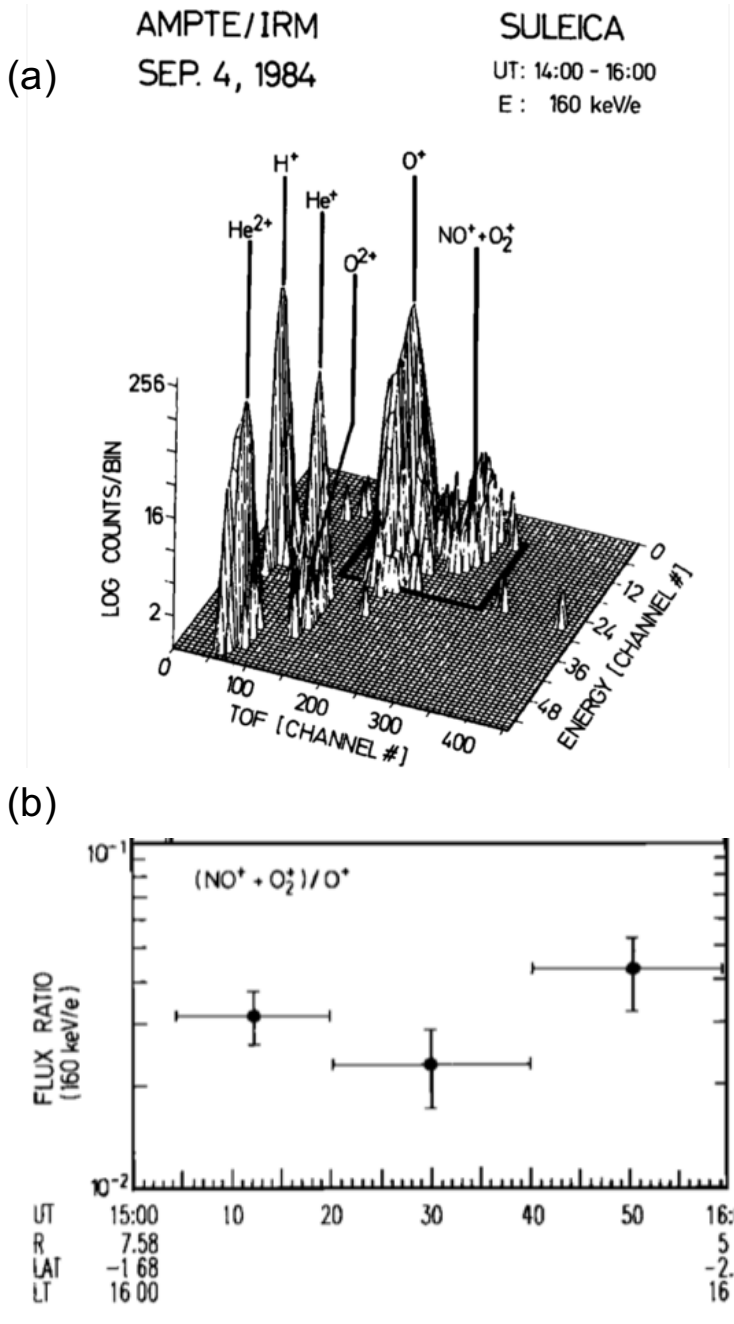

Figure 1.14: (a) The energy versus time-of-flight distribution of energetic ions at 160 keV/e and (b) the flux ratio of molecular ions (O_2^++NO^+) to atomic oxygen ions (O^+) at 160 keV/e [Klecker et al., 1986]. This result is important as an observational fact on existence of molecular ions in the magnetosphere but simultaneously indicates the scarcity of molecular ions.

1.2.3 Meaning of molecular ions

Is there any role of the molecular ions in space plasma? In fact, molecular ions are not able to affect the hydro dynamics due to very minor species even during the magnetic storms and there are not too many studies coupled with the observational limitations. However, a recent study by Seki et al. [2019] revealed that molecular ions are detected even during small magnetic storms (Dst ~ -30 nT) based on the observations by the Arase satellite, which provides high-resolution time-of-flight (TOF) data [c.f., Section 2.1 in detail]. The result suggests that the molecular ions in the magnetosphere are more important than we expected before. They also mentioned about the possibility of molecular ions as a tracer to detect the deep ionospheric outflow. The source of molecular ions is low-altitude ionosphere and usually gravitational forces binds the ions. The upward transportation is needed from bottom to top side of the ionosphere to observe the ions in the magnetosphere. That is, molecular ions in the magnetosphere indicate the geomagnetic disturbance and ion outflow from the deep ionosphere. Molecular ions could be a tracer of the altitude where the ions start escaping.

Section 1.3 Ion upflows

1.3.1 Characteristics of ion upflows

Heavy ions, especially molecular ions, exist low-altitude ionosphere (< 300 km); thus, the upward transportation called "ion upflow" is necessary in the ionosphere before outflowing to the magnetosphere. An ion upflow is often interpreted as a set of flow events with ion upward velocity or flux along the geomagnetic field in the ionosphere.

Many previous studies investigated the properties of ion upflows in the polar ionosphere and most of them mainly focused on the high-altitude ionosphere (> 400 km), where O^+ is dominant. For example, Kosh et al. [2010] investigated the generation mechanisms of ion upflows caused by artificial heating experiments by the EISCAT radar. They revealed that the enhanced upward electron pressure gradient by ionized and energized electrons could contribute to the ion upflows at the altitude of 400-500 km by evaluating each term in the momentum equation. There is another study which reveal the formation of ion upflow in terms of the precipitation energy. Caton et al. [1996] estimated necessary energy for generating the ion upflow by auroral electron precipitations. The results indicate that soft electron precipitations (< ~1 keV) can cause the ion upflow at the high altitudes (> ~400 km) and also suggest that it is difficult to drive upward flows by such soft precipitations in the low-altitude ionosphere (< ~300 km). The convection motion is also important. SAPS, which is westward flow caused by convective electric field (briefly introduced in Section 1.1.3), possibly contributed to ion upflows via Joule heating (the frictional heating) between ions and neutrals [Zhan et al., 2020].

The dependence of the properties on the magnetic storms is also important. Ogawa et al. [2019] investigated the dependence of the ion velocity and flux on CIR-/CME- driven magnetic storms based on the long-term observations by EISCAT from 1996 to 2015. They focused on the high-altitude ionosphere (400-500 km) during magnetic storms. Table 1.2 represents a summary table on the investigation. During both CIR- and CME- driven storms, upward ion flux around duskside and nightside was pronounced at Tromsø. The difference between CIR- and CME- storms is intensity of the flux. CME-driven storms resulted in the large upward ion flux. On the other hand, ion flux was enhanced around dawnside and dayside at Svalbard during CIR-driven storms and small CME-driven storms, while it was enhanced around midnight during large

CME-driven storms. Also, they suggested the candidate mechanisms based on the ionospheric empirical Weimer model [Weimer, 2005]. Figure 1.15 represents the summary drawing on the properties of ion upflows in the high-altitude ionosphere (400-500 km) presented by Ogawa et al. (2019). Developed Region 1 field aligned currents cause the significant upflows in the dayside during CIR-driven storms and increase of the ion temperature with Joule heating (the frictional heating) was remarkable in nightside during CME-driven storms. Both CIR-/CME-driven storms cause particle precipitations and stronger precipitations occurred during CME-driven storms than CIR-driven storms around the auroral oval.

Table 1.2: Summary table on averaged ion flux from 400 to 500 km at Tromsø and Svalbard during CIR-/CME- driven magnetic storms [Ogawa et al., 2019].

Table 1
Summary of Ion Upflow Flux at Each Region on the First Day of Magnetic Storm

		CIR		CME	
66.2° mlat. (Tromsø)		Small storm	Large storm	Small storm	Large storm
	Dawnside	~0	~0	0.2	-
	Daytime	~0	~0	0.2	~0
	Duskside	0.2	0.2	0.2	0.5
	Nighttime	0.3	0.2	1.2	3.3
		CIR		CME	
75.2° mlat. (Longyearbyen, Svalbard)		Small storm	Large storm	Small storm	Large storm
	Dawnside	0.3	0.1	~0	0.2
	Daytime	1.2	0.5	0.9	−0.2
	Duskside	0.1	~0	−0.3	−0.2
	Nighttime	0.1	~0	~0	1.5

Note. The unit of the ion flux is ($\times 10^{13}$ $m^{-2}s^{-1}$).

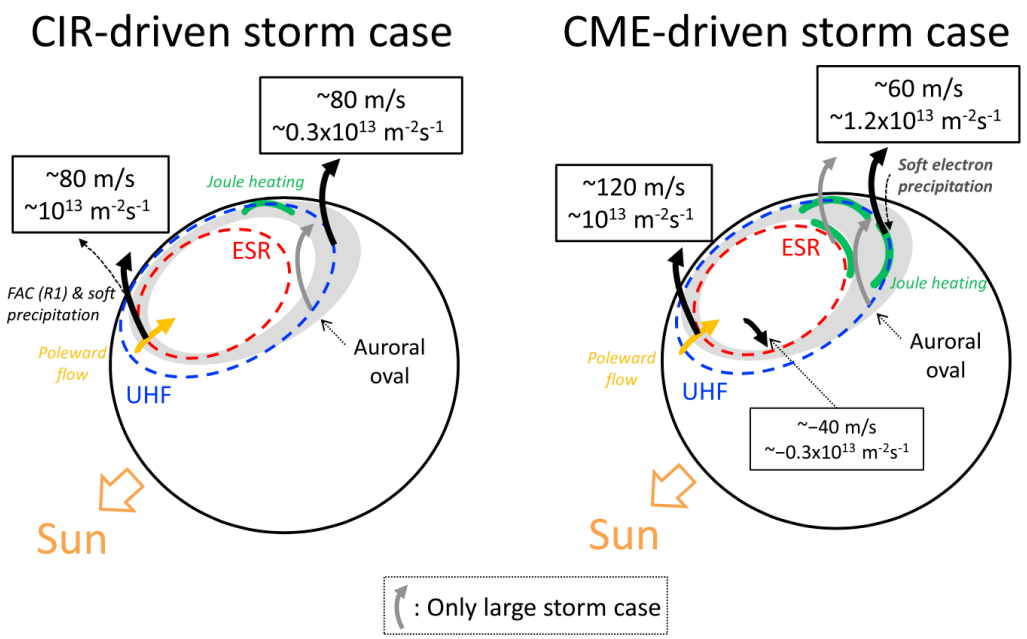

Figure 1.15: Schematic drawing of the ion upflows in the high-altitude ionosphere (400-500 km) based on the EISCAT observations and the mechanisms estimated by the empirical Weimer model in each MLT sector: dawnside (03-09 MLT), dayside (09-15 MLT), duskside (15-21 MLT), nightside (21-03 MLT) [Ogawa et al., 2019]. There are different properties during CIR- and CME- driven storms. MLT: Magnetic Local Time.

1.3.2 Formation mechanism of ion upflows

Some mechanisms have been proposed to explain how to generate the ion upflow: the ion frictional heating (Joule heating), particle precipitation, and ion heating caused by small or large scale plasma instabilities [Ji et al., 2019 and there in].

The ion frictional heating occurs when collisions between ions and neutrals convert the energy associated with the convection motion of the ions into the thermal energy. Therefore, the convective electric field is important. The convective electric field is associated with the current or conductivity and drives ion flow known as $E \times B$ drift. Then, the frictional force is generated because the ion bulk velocity differs from the neutral velocity. Thus, the neutral particles diffuse the ions in phase space and the ion temperature increases. The enhancement of the ion temperature results in enhancement of the ion pressure gradient and upward pressure gradient generate ion upflow. Ion upflows driven by the frictional heating are defined as Type1 ion upflows.

The particle precipitation can give energy to ions via the ambipolar electric field. The precipitating particles such as high-energy electrons from the nightside inner magnetosphere ionize the upper neutral atmosphere and create energized electrons in the low-altitude ionosphere. These electrons sometimes overcome the restriction by the gravitational force and move upward. Those electrons lead to the charge separation and created electric field called ambipolar electric field. Then, ions move upward by the ambipolar electric field. Note that, the ambipolar electric field caused by the charge separation is balanced with the enhanced electron pressure gradient itself. Ion upflows driven by the particle precipitation are defined as Type2 ion upflows.

Ion heating caused by small or large scale plasma instabilities are resulted from the interaction between ions and waves: ion cyclotron resonance, lower hybrid wave, ULF wave and so on. It is also driven by field aligned current in large scale plasma instabilities. One of the candidate examples other than Type1 and Type2 upflows is velocity-shear related ion upflows, which are caused by the electrostatic turbulence due to the sheared flows transverse to the magnetic field [c.f., Liu and Lu, 2004]. It is easier to cause the field-aligned currents instabilities and electrostatic waves in the ionosphere when such transverse flows exist, and then glowing waves with vortices become potential sources to accelerate ions. However, it is difficult for present ground based observations to observe waves in the ionosphere. Thus, most of them are suggested based on the simulations.

1.3.3 Differences between low-altitude and high-altitude upflows

Ion upflows are indispensable phenomena, which supply not only O^+ ions but also molecular ions such as O_2^+, NO^+ and N_2^+ from the low-altitude ionosphere into the magnetosphere. The dominant species change at each altitude in the ionosphere; Thus, it is important to consider the difference between low-altitude (< 300 km) and high-altitude (> 400 km) ionosphere in order to discuss the difference on supply processes between O^+ and molecular ions.

1. Force balance

In the low-altitude ionosphere, the important forces are different from high-altitude case. The direction of the plasma pressure gradients is important to determine the direction of the ion velocity. Yamazaki et al. [2017] revealed that the direction of the averaged ion velocity changed around ~350 km during the low solar activity and ~450km during the high solar activity. It is considered that the variation of the peak altitude for the electron density resulted in the change of the plasma pressure gradients and the direction of the velocity in the dayside ionosphere. In addition to that, the drag force by neutrals is not negligible in the low-altitude ionosphere due to the dense neutral atmosphere. Yamazaki et al. [2017] also suggested that the effect of neutral wind was important especially in the nightside low-altitude ionosphere.

2. Reaction efficiency of the dissociative recombination

Molecular ions rapidly decrease due to the dissociative recombination, which is one of the chemical reaction between ions and electrons [c.f., Table B1 in Terada et al., 2009]. Molecular ions are divided into atomic components; For example, NO^+ is divided into atomic N and O. The electron density reached more than 10^{11} and even 10^{12} m^{-3} in F layer. Thus, the reaction efficiency of the dissociative recombination is high and molecular ions decrease more rapidly in the low-altitude ionosphere than high-altitude ionosphere. Peterson et al. [1994] estimated time for the energy transfer to overcome the dissociative recombination based on the observational data from the Akebono satellite. They

concluded that any heating mechanisms such as frictional heating cannot provide enough energy and a remaining candidate might be small-scale plasma instabilities.

Section 1.4 Objective of this study

The ionosphere is one of the important parts of planetary plasma and atmosphere. The ionospheric plasma escape from a planet due to the effect of the stellar wind and it is important source of the space plasma around the planet. This escape process is told in the context of atmospheric evolution and one of the essential scientific targets to understand the origin of the planet. However, it is difficult to always observe the whole planetary ionospheric conditions, even if we aim at the terrestrial ionosphere with all ground based observations. Thus, studies of subjects are important, which can reveal escape mechanisms in atmospheric evolution from the limited observations. Heavy ions such as O^+, O_2^+, NO^+ are one of the most useful subjects. Heavy ions usually exist in the bottom side of the ionosphere because of their mass. Those ions are sometimes transported into the space due to the effect of stellar wind and could be a good tracer of the ionospheric disturbance and escape process. In particular, heavy ions are often observed during geomagnetic disturbance periods around the Earth.

During magnetic storms, it is known that both the atomic oxygen ions (O^+) [e.g., Daglis et al., 1999; Nose´ et al., 2005; Keika et al., 2013] and molecular ions (O_2^+/NO^+) [e.g., Klecker et al., 1986; Seki et al., 2019] exist in the ring current. These heavy ions in the ring current originate from the terrestrial ionosphere. With regard to O^+, many scientists have studied since the first discovery of significant O^+ fluxes escaping from the ionosphere [Shelley et al., 1972]. It is generally agreed that most of the O^+ observed in the ring current originate from the ionosphere because of the lack of heavy ions in the solar wind and many observational results in outflow processes as introduced in Section 1.2.1 and 1.2.2. In fact, strong field-aligned bulk ion outflows, which can transport O^+ into the magnetosphere, were observed by incoherent scatter radars in the high latitude auroral ionosphere [e.g., Ogawa et al., 2008] and these ions were also observed with the magnetospheric convection flow such as flow-reversal events in the plasma sheet [Christon et al., 1994]. These results suggest the supply mechanisms into the

magnetosphere about O^+ quantitatively.

On the other hand, observations of molecular ions in the magnetosphere are rather limited when compared with those of the O^+ ions. One of the reasons why there are few observations is that molecular ions exist much less than O^+ in the ring current. Molecular ions in the inner magnetosphere have been observed since the first report by AMPTE/IRM [Klecker et al., 1986] and also recently observed by the Arase(ERG) satellite during geomagnetically active periods [Seki et al., 2019]. Any study about observational molecular ions indicated that the ratio of molecular ions to the O^+ ions reached several percentage at most as described in Section 1.2.2. It makes difficult to discuss quantitative assessments especially for in-situ observations in the magnetosphere.

However, Seki et al. [2019] simultaneously revealed that molecular ions were observed even during small magnetic storms (Dst ~ -30 nT) and suggested the importance of molecular ions as a tracer of outflows from the deep ionosphere, as explained in Section 1.2.3.

Regarding the source region, molecular ions exist in the low-altitude ionosphere (< 300 km) although O^+ exist in the high-altitude ionosphere (> 400 km) and even top side ionosphere (~ 1000 km). Thus, it is necessary to transport molecular ions upward (ion upflows) in the low-altitude ionosphere before outflowing into the magnetosphere. There are many studies to reveal the characteristics of ion upflows focusing on the high-altitude ionosphere as described in Section 1.3.1.

The generation mechanism of ion upflows is one of the most important properties. As introduced in Section 1.3.2, the ionospheric ions can be transported upward against the gravitational force by some acceleration mechanisms caused by the ion frictional heating (Joule heating), particle precipitation, and small or large scale plasma instabilities. There are, however, many differences between low- and high-altitude ionosphere. In particular, it is serious problem how much molecular ions are supplied into the high-altitude ionosphere overcoming the decrease due to the dissociative recombination as described in Section 1.3.3. Peterson et al. [1994] reported that any candidate heating mechanisms could not provide molecular ions with enough energy to escape, as results of the estimations with observational data obtained by AKEBONO satellite. They finally suggested that the small-scale plasma instabilities might contribute. However, it has not been clearly revealed what mechanisms actually generate the rapid ion upflow, which can supply sufficient flux of molecular ions from low-altitude ionosphere into high-altitude

ionosphere and even into the magnetosphere (Question 1).

As introduced in Section 1.3.1, Ogawa et al. [2019] reported that ion upflows and their generation mechanisms in the high-altitude ionosphere (400-500 km) during CIR- and CME-driven storms have different dependence on magnetic local time in each storm. Such properties of ion upflows in the low-altitude ionosphere is also important because any magnetospheric molecular ions cannot be supplied and observed without low-altitude ionospheric upflows, which can transport these ions at the beginning. However, it has not been revealed how the properties and generation mechanisms of the low-altitude ion upflows change with the size and types of the magnetic storms (Question 2).

In this study, the author aims at comprehensive understanding of ion upflows in the low-altitude ionosphere and their effects on supply of terrestrial heavy ions to the magnetosphere by solving the outstanding questions as mentioned above (Question 1 and Question 2) throughout an event study and a statistical study.

This thesis is organized as follows: The instrumentation and method used in this study are described in Chapter 2. Chapter 3 describes the event study about an ion upflow observed by the EISCAT Tromsø UHF radar on September 8, 2017 and observations of molecular ions by Arase (ERG) satellite in the inner magnetosphere during the magnetic storm started on September 7. This chapter is written based on the contents in the published paper [Takada et al., 2021]. Chapter 4 describes a statistical study about the effects of CIR-/CME- driven magnetic storms on properties of ion upflows and their mechanisms in the low-altitude ionosphere based on the long-term observations by the EISCAT radars. The general discussion is described in Chapter 5 and the general conclusion is summarized in Chapter 6.

Chapter 2 Instrumentation & method

Section 2.1 Arase(ERG) satellite

Arase (ERG) satellite was launched with perigee of 460 km and apogee of 32,110 km on December 20, 2016 [Miyoshi et al., 2018c]. One of the main purposes of this probe is to observe the Van Allen radiation belts and another target is the ring current during magnetic storms conjugating with ground-based observations. There are five instruments to observe particles for each energy. Extremely High-Energy Electron Experiment (XEP) observed energetic electrons (0.4-20 MeV). Medium-Energy Particle Experiments - Ion Mass Analyzer (MEP-i) and Low-Energy Particle Experiments - Ion Mass Analyzer (LEP-i) observe the ions (10-184 keV/q and 0.01-25 keV/q). In particular, MEP-i and LEP-i have the time of flight (TOF) mode in which they can distinguish the ion species by using the time difference due to the mass per charge (M/Q). The time difference between the “start” electrons and “stop” electrons corresponds to the time-of-flight of the ions. We can know the energy of those ions. Thus, we can get the M/Q information by combining them. In particular, TOF mode can detect the minor species such molecular ions because of the high-resolution time-of-flight data instead of the angular resolution. For example, using TOF mode of MEP-i, we can obtain the count number and differential flux data for each ion every 16 seconds from 4 circularly aligned anodes based on the 512 channel TOF data. [Yokota et al., 2017].

Section 2.2 EISCAT radars

2.2.1 EISCAT radars

European Incoherent Scatter Scientific Association (EISCAT) radars observe the earth's polar ionosphere over more than 20 years. The EISCAT radars at Tromsø (69°35′ N, 19°14′ E, Invariant Latitude: 66°12′ N) observe the ionosphere with two incoherent scatter systems: Ultra High Frequency (UHF) and Very High Frequency (VHF) radar (933 MHz and 224MHz). The EISCAT radars at Svalbard (78°09' N, 16°03' E, Invariant Latitude: 75°10' N) observe the ionosphere with 32m and 42m antennas and the 42m antenna radar usually directs the magnetic field line. EISCAT Svalbard radars (ESR) locate higher latitude than EISCAT Tromsø UHF and VHF radars. Each location of EISCAT radar is mapped on the panel (a) in Figure 2.1. These EISCAT radars are operated in several experiment modes depending on the target altitudes. The panel (b) in Figure 2.1 represents examples of the experiment modes. The "beata" mode in the EISCAT Tromsø UHF radar focus on the altitudes of 49-693 km and useful to analyze phenomena in F layer, although the "manda" mode focus on 19-209 km and useful for D layer. In principal, EISCAT radars receive pulse signals as Power Spectral Density function (PSD), which is converted from Auto Correlation Function (ACF) by Fourier transformation. Integrating the PSD in a particular time resolution and fitting the result, we can derive the time variations of physics parameters with error values at each altitude.

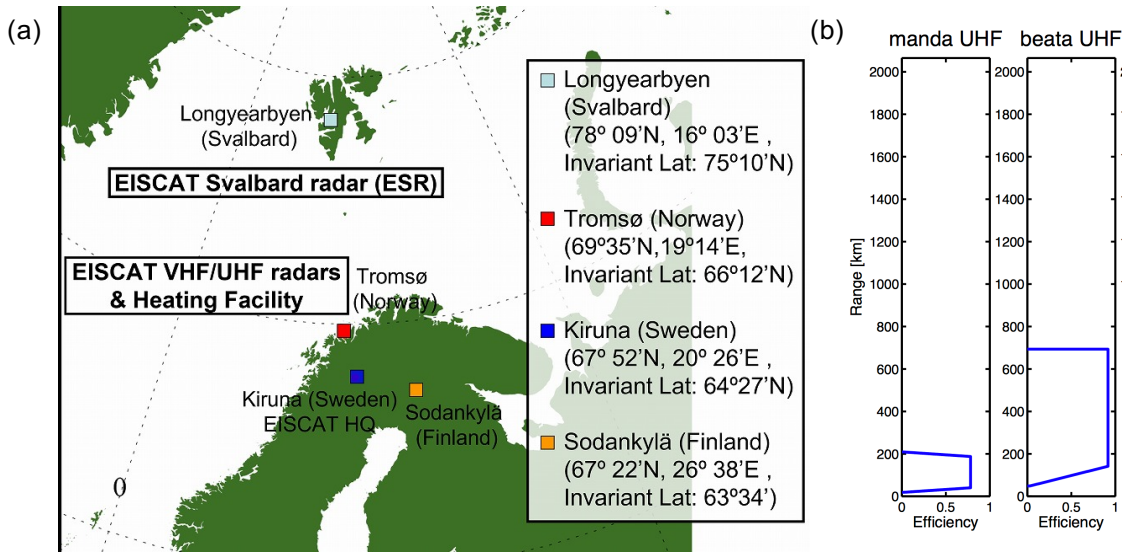

Figure 2.1: (a) EISCAT radar sites [https://polaris.nipr.ac.jp/~eiscat/en/gi/] and (b) examples of the current experiment modes [https://eiscat.se/wp-content/uploads/2017/04/Experiments.pdf].

2.2.2 Principles of the Incoherent Scatter radar observation

The Incoherent Scatter (IS) radar succeeds in observing the ionospheric plasma parameters by the Thomson scattering of electrons in the ionosphere. The typical density n_e is $\sim 10^{11}\, m^{-3}$ and the electron temperature T_e is ~ 2000 K in the ionosphere, so that Debye length is

$$\lambda_D = \sqrt{\frac{\varepsilon_0 k_B T_e}{n_e e^2}} \cong 69\sqrt{\frac{T_e}{n_e}} \approx 0.01 \text{ [m]} \tag{2.1}$$

where ε_0 is the dielectric constant of vacuum, k_B is Boltzmann constant and e is the elementary charge. When Incoherent Scatter radar sends waves, which are longer than the Debye length, the radar receives the signals which are sensitive to the ion motion because the electrons are moving much faster in the ionosphere to meet the quasi-neutral state. For example, EISCAT Tromsø ULF and VHF radar send waves which correspond to the waves length of ~0.32 m or ~1.3 m, which are longer than the Debye length in the ionosphere.

The IS radar receives the signals as PSD function from the ionosphere. The transmission frequency ν_0 is shifted by the ion bulk motion in the ionosphere (Doppler shift). The relationship between the ion velocity along the line-of-sight direction V_i and the Doppler shifted frequency ν is described as

$$\nu = \frac{2V_i}{\lambda_0} \tag{2.2}$$

where λ_0 is the transmission wavelength.

The effects of existence ions in the ionosphere appear in the ion acoustic line,

$$V_+ = \sqrt{\frac{k_B T_i}{m_i}\left(1 + \frac{T_e}{T_i}\right)} \ . \tag{2.3}$$

Scattered wave interferes with the electron density fluctuation of the half wavelength of the transmission wavelength λ_0 and the IS radar receives the upshifted and downshifted

spectrum by enhanced back-scattering as ion acoustic line at the frequency,

$$\delta\nu_{\pm} = \pm\frac{2}{\lambda_0}\sqrt{\frac{k_B T_i}{m_i}\left(1+\frac{T_e}{T_i}\right)} \quad . \tag{2.4}$$

An IS radar equation is derived from the quasi-incoherent model when the ratio of the transmission wavelength to the Debye length is more than 1. In the model, the electron and ion charge density (δN_e and δN_i) fluctuations are defined by

$$e\,\delta N_e^{(e)} = -\left(1-\frac{\chi_e}{\epsilon}\right)\rho_e \tag{2.5}$$

$$e\,\delta N_i^{(e)} = \frac{\chi_e}{\epsilon}\rho_i \tag{2.6}$$

$$\epsilon = 1+\chi_e+\chi_i \tag{2.7}$$

where e is the elementary charge, χ_e is the electron dielectric constant, ρ_e is the electron charge density, ρ_i is the ion charge density. Combining Eq. (2.5) and Eq. (2.6), we can obtain the total charge fluctuations δN_e:

$$e\,\delta N_e \equiv e\,\delta N_e^{(e)} + e\,\delta N_i^{(e)} = -\left(1-\frac{\chi_e}{\epsilon}\right)\rho_e + \frac{\chi_e}{\epsilon}\rho_i \quad . \tag{2.8}$$

The electronic oscillation spectrum is derived as

$$< \delta N_e^*(\boldsymbol{k},\omega)\,\delta N_e(\boldsymbol{k},\omega) > = \left|1-\frac{\chi_e}{\epsilon}\right|^2 \mathcal{N}_e(\boldsymbol{k},\omega) + \left|\frac{\chi_e}{\epsilon}\right|^2 \mathcal{N}_i(\boldsymbol{k},\omega) \tag{2.9}$$

$$q_{e,i}\mathcal{N}_{e,i}(\boldsymbol{k},\omega) = < \delta\rho_{e,i}^*(\boldsymbol{k},\omega)\,\delta\rho_{e,i}(\boldsymbol{k},\omega) > \tag{2.10}$$

where $\mathcal{N}_{e,i}$ means the spectrum of the normal mode for each particle (an ion or electron). Introducing the Dressed particle theorem of Hubbard and Rostoker [e.g. Ichimaru, 2004] and assuming the Maxwellian distribution function, Eq. (2.9) is finally solved,

$$P_r = \frac{Cc_0 G\lambda^2}{2}\frac{P_t\tau_P}{r^2}\frac{\sigma_e n_e(r)}{\{1+(k\lambda_D)^2\}\{1+(k\lambda_D)^2+T_r\}} \tag{2.11}$$

where C is the system constant such as aperture area and status of the pulse code, c_0 is the speed of light, G is the gain, λ is the radar wave length, P_t is the transmitted power, τ_P is the pulse length, σ_e is the scattering cross section of one electron, r is the range or altitude, k is the wave vector, $n_e(r)$ is the electron density at r, $T_r = \frac{T_e}{T_i}$ is the temperature ratio of the electron to ion. P_r means the reception intensity and Eq. (2.11) is the IS radar equation.

The spectrum is affected by Landau damping because it depends on the ion and electron temperature. Now, if we assume the Maxwellian plasma, and the phase velocity is much higher than ion velocity and much higher than ion thermal velocity, and quasi-incoherent model, we can obtain the attenuation rate γ ($\omega = kc_s + i\gamma$) which corresponds to the amount of the damping:

$$\gamma \propto \left\{ \sqrt{\frac{m}{M}} + (T_r)^{\frac{3}{2}} e^{-2\,T_r} \right\} \tag{2.12}$$

where m is the electron mass, M is the ion mass. The first term corresponds to the Landau damping driven by electron and the second term corresponds to it by ion. Therefore, we can estimate the T_r considering the Landau damping. Note that, the explanation was simplified to clarify the physical interpretations. In fact, the fitting algorithm of EISCAT given by Grand Unified Incoherent Scatter Design and Analysis Package (GUISDAP) [Lehtinen and Huuskonen, 1996] include the complex conditions and estimations of the instrumental errors such as Signal to Noise Ratio (SNR).

We can derive the data from the PSD which the IS radar accepted based on those physical mechanisms. Figure 2.2 shows the cartoon illustration of obtained PSD and correspondences of each mechanisms to the variations on PSD. In the obtained PSD diagram, the Doppler shifted frequency determined by the ion bulk velocity along the line-of-sight direction corresponds to the shift in the horizontal axis; the reception intensity mainly determined by the electron density corresponds to the size of the expanding area; and ion acoustic line and the effect of Landau damping mainly determined by ion and electron temperatures contribute to the shape of the PSD function with two peaks.

Identification of the target signals is also important because of very weak signals from the ionosphere. The one-dimensional range-amplitude ambiguity function W_t^A is

$$W_t^A(S) = \int_{-\infty}^{+\infty} h(t-\tau) env(\tau - t)\, d\tau \tag{2.13}$$

$$= (h * env)\,(t - S) \tag{2.14}$$

where S is the propagation time ($S = \frac{2r}{c_0}$), t is the time when IS radar receives the first signal, h is the impulse response of the receptor, env is the envelope. Figure 2.3a represents schematic diagrams on the range-amplitude ambiguity function. The transmission wave returns at t and the peak of the range-amplitude ambiguity function is seen at $t - T$, where T is the characteristic parameter in the definition of the h and env as the step functions. When the delay caused by the modulation envelope is δT, we defined the fundamental pulse signal in $\delta T + 2T$ as the step function between $t - 2T - \delta T$ and t at the IS radar; then, the signal shapes a trapezoid against S. We set δT as 0 and it is most efficient in ideal, but we are not able to do so because too high time resolution means the too big SNR to identify the true signal. Figure 2.3b represents the cartoon illustration of the observational system of the IS radar. An emission with a particular signal pattern propagate with the light speed and return from the ionosphere after a while. Then, we can obtain the altitudinal information from the elapsed time and the signal amplitude is finally obtained by weighted average based on the Range-amplitude ambiguity function and spherical effect, which depends on $\frac{1}{r^2}$.

The EISCAT radar contrive some pulse coding methods to improve the signal amplitude. One of the representative methods is multi pulse code and another is Barker code. In these codes, we treat 1 bit packet which is created by using the fundamental pulse signal and opposite phase signal. The multi pulse code is the simple code. By using multi pulse codes, we can obtain signal amplitude depending on the linear summation of fundamental pulse signals; the signal amplitude is several times larger than by using the fundamental signals. On the other hand, the n-bit Barker code enables us to obtain the signal amplitude n^2 times larger than the fundamental pulse signal at the targeting altitude,

which is n times larger than using the multi pulse codes. Figure 2.4 represents the cartoon illustration about the observational system of IS radar by using Barker codes and its example especially in case of the 13-bit Barker code. It is important that the initial set of the bit combination enables to distinguish between unnecessary and the target regions in the Barker codes. The n-bit Barker code is useful in the actual observations.

It is important to obtain ACFs with different Lag profiles. IS radars use random signals caused by random plasma fluctuations and the signals from different plasma region, i.e., different altitudes in the terrestrial ionosphere, do not correlate. Thus, the signals with time Lag are needed to obtain a PSD at a particular altitude from the corresponding ACF. To obtain several ACFs with different Lag profiles, Alternating code is useful and effective. The Alternating code is composed of the long pulses, which have different phase code. The n-bit Alternating code provide range ambiguity functions at n-1 altitudes for first lag by combining each envelope during one cycle. The Alternating code is 2 times more efficient than multi pulse code. On the other hand, Barker code can create the strong amplitude but needed other pulse codes such as multi pulse code to obtain Lag profiles. For example, 4-bit Alternating code consists of 8 envelopes as shown in Figure 2.5. In this thesis, the author used “beata” mode data of EISCAT to analyze the ion upflow in detail. The “beata” mode is one of the Alternating code. The ”beata” uses the 32-bit Alternating code for the Tromsø UHF radar. The lag step and sampling rate is 10 micro seconds for ion line measurement. The minimum time resolution is 5 seconds and range gate is 1.5 km. The targeting altitude is 49 to 693 km along the magnetic field line.

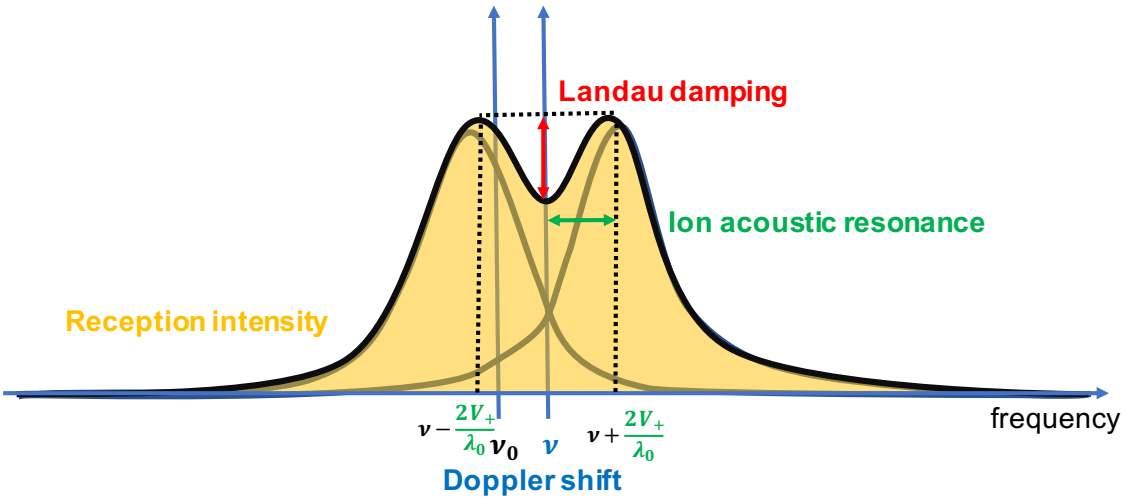

Figure 2.2: Cartoon illustration of obtained PSD and correspondences of each mechanisms to the variations on PSD.

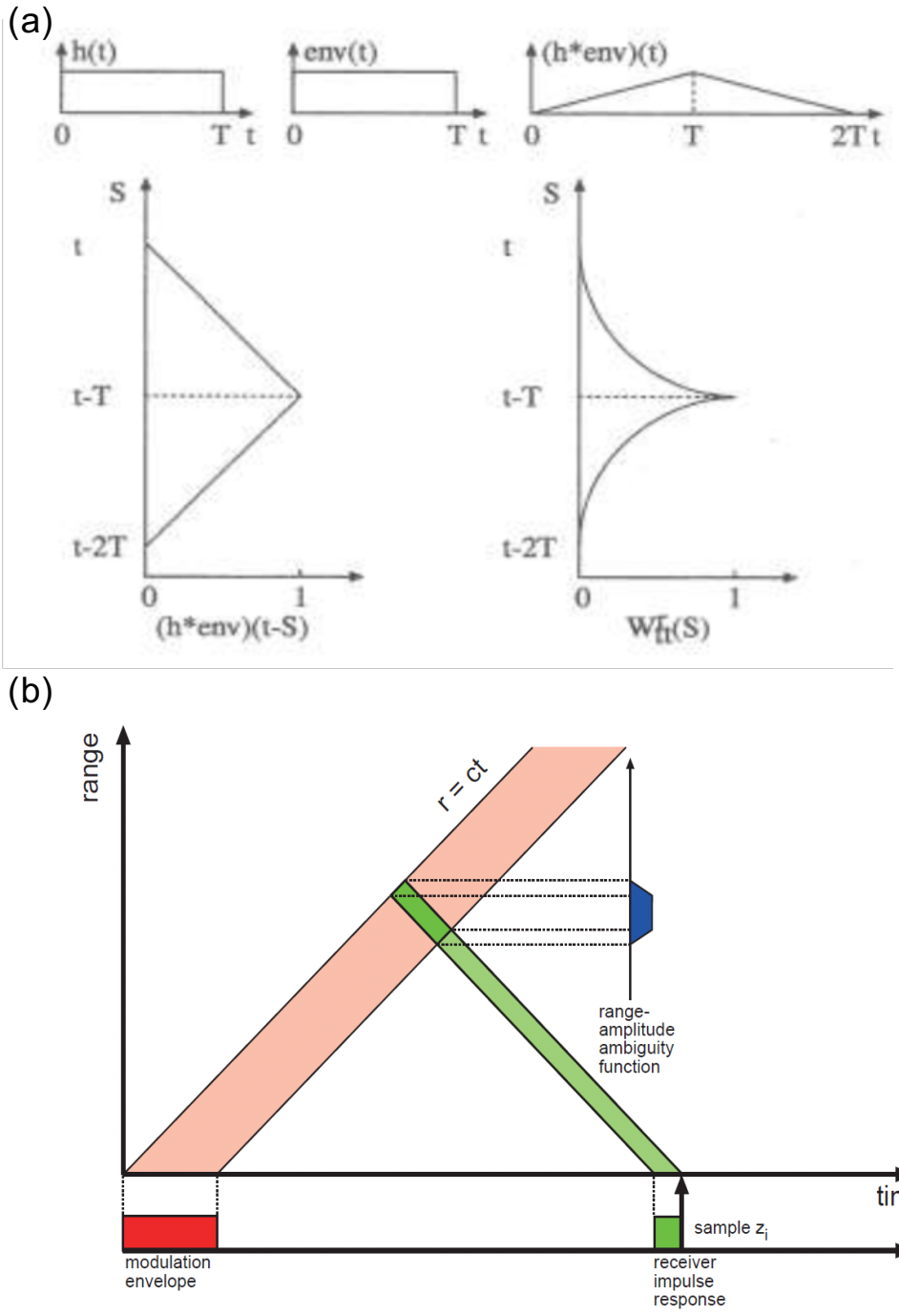

Figure 2.3: (a) schematic diagrams on a range-amplitude ambiguity function and (b) a cartoon illustration of the observational system of IS radar [Nygrén, 1996].

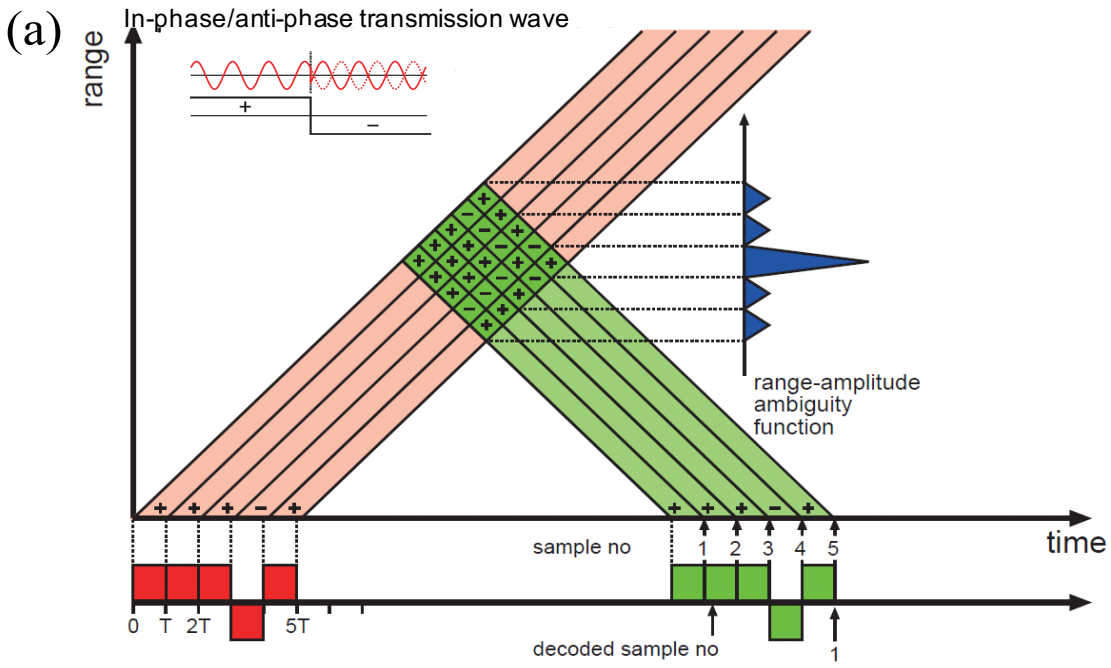

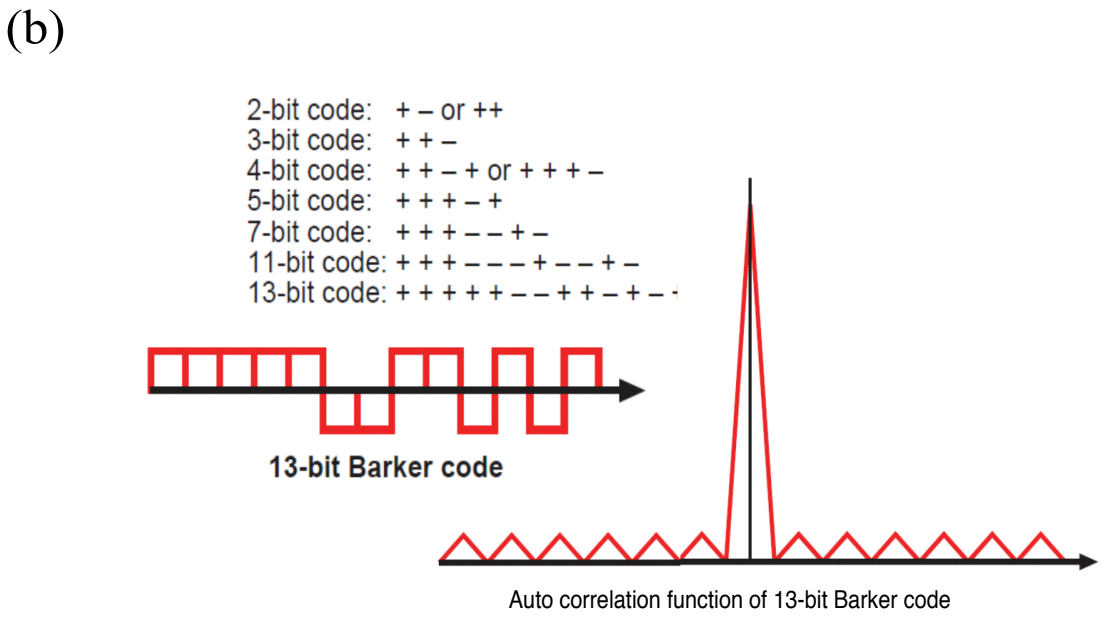

Figure 2.4: (a) the cartoon illustration about the observational system of IS radar by using Barker codes and (b) its example especially in case of the 13-bit Barker codes [Nygrén, 1996].

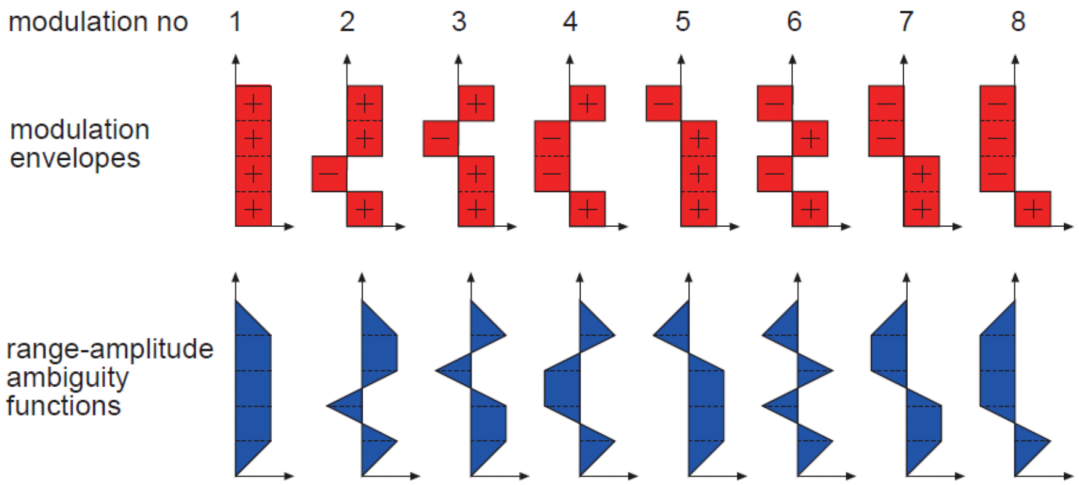

Figure 2.5: A cartoon illustration about 4-bit Alternating code [Nygrén, 1996].

2.2.3 Convective electric fields

It is important to estimate strength of electric fields. However, it is difficult to observe it directory by EISCAT. Thus, we use the relationship between enhancement of convective electric fields and the electron temperature at the low conductivity layer. In the previous study [J. A. Davies and T. R. Robinson, 1997], they reported that the convective electric field and the electron temperature at the altitude of 111 km have the almost monotonic dependence as shown in Figure 2.6. In order to evaluate the strength of the convective electric fields, the author translated the electron temperature at the altitude of ~110 km into an amplitude of the electric fields based on the result of the previous study [J. A. Davies and T. R. Robinson, 1997] or directly assumed the electron temperature at ~110 km without such a translation.

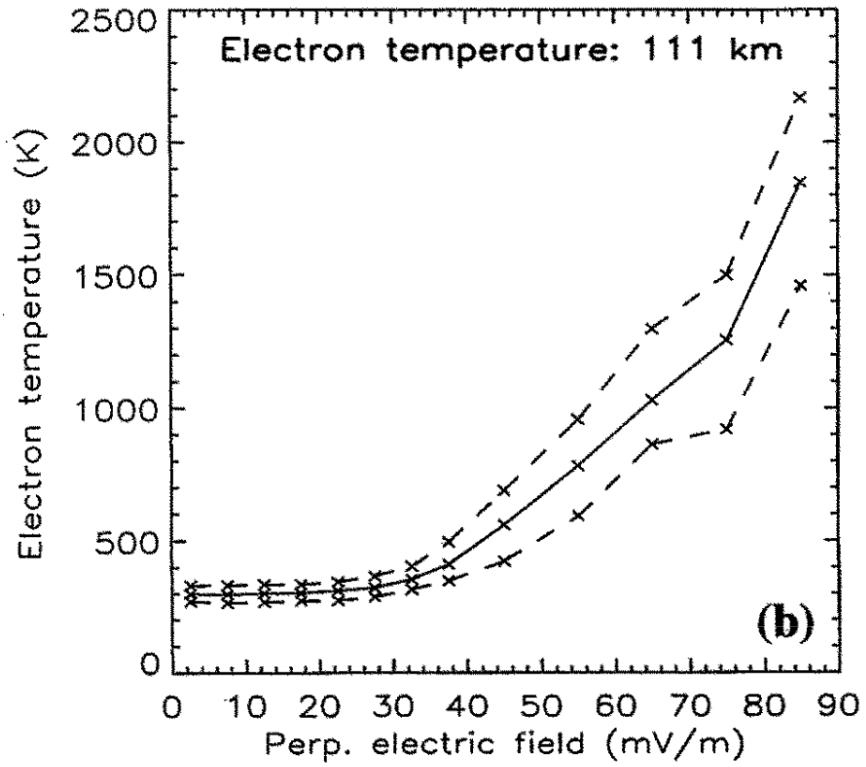

Figure 2.6: The relationship between the convective electric field and the electron temperature at the altitude of 111 km reported by Davies and Robinson [1997].

Section 2.3 Method for an event study

2.3.1 Instrumentation and data set

The Arase (ERG) satellite was launched on December 20, 2016 to investigate dynamic variations in the geospace environment as described in Section 2.1. The author used the MEP-i omni flux data in TOF mode provided as the summation of 4 directional fluxes to detect molecular ions on September, 2017. The data have been corrected for O^+ contamination following the method presented in Seki et al. [2019]. The author used the 512 channel TOF data (10-184 keV/q) accumulated over 30 minutes and fitted them by using the equation described in Seki et al. [2019] to obtain the actual count of molecular ions: $A_0 e^{-\frac{1}{2}\left(\frac{x-A_1}{A_2}\right)^2} + A_3 + A_4 x$. The baseline and linear functions fitted the slope of the contamination from O^+ and high-energy electrons and Gaussian part could catch the peak and expansion of O^+ counts. Then, the author obtained energy density (ED) ratio profile of molecular ions to O^+ ions.

EISCAT UHF radars at Tromsø (69°35′ N, 19°14′ E, Invariant Latitude: 66°12′ N) observe the polar ionosphere as described in Section 2.2.1. The author derived ionospheric plasma parameters from PSD of the EISCAT Tromsø UHF radar data by using GUISDAP. Here, the author obtained observational data with the EISCAT Tromsø UHF radar in 'beata' mode along the magnetic field line, as the resolution was 1 minute for time and 3 km (70-120 km), 10 km (120-150 km), 20 km (150-250 km) and 30 km (250-600 km) for altitude. The electric field was derived from the electron temperature at the altitude of ~110 km, which is based on the previous study by Davies and Robinson (1997) [cf., Section 2.2.3].

2.3.2 Estimations of the molecular ion flux

To estimate molecular ion loss due to the dissociative recombination during the course of the ion upflow, the author used the following method. Molecular ions are composed mainly of O_2^+ and NO^+ in the low-altitude ionosphere, decrease due to the dissociative recombination and almost disappear at higher altitudes (>300 km) in the

ionosphere. To estimate the minimum amount required for molecular ions to be the source of magnetospheric molecular ions, the author interpolated the field-aligned velocity data and calculated loss by the dissociative recombination based on the steady-state continuity equation for gyrotropic and quasi-neutral plasma in the field aligned direction:

$$\frac{\partial \left(n_{O_2^+ (NO^+)} V_i \right)}{\partial s} = -n_{O_2^+ (NO^+)} n_e \nu_{diss} \tag{2.14}$$

where $n_{O_2^+ (NO^+)}$ is the density of O_2^+ (NO^+), V_i is the ion bulk velocity, n_e is the electron density and ν_{diss} is the reaction rate of each dissociative recombination. Here, ν_{diss} was estimated based on the following model with the observational electron temperature T_e [Terada et al., 2009]:

$$O_2^+ + e^- \rightarrow O + O: \ \nu_{diss} = 7.4\times10^{-8} \left(\frac{1200}{T_e}\right)^{0.56} \ [cm^3\ s^{-1}] \ (T_e > 1200\ K) \tag{2.15}$$

$$NO^+ + e^- \rightarrow N + O: \ \nu_{diss} = 4.0\times10^{-7} \left(\frac{300}{T_e}\right)^{0.50} \ [cm^3\ s^{-1}]. \tag{2.16}$$

The author set the initial O_2^+ (NO^+) density and flux at an altitude of 280 km using the observed electron density and ion velocity. The author also used the IRI 2016 model [Bilitza et al, 2016] to determine the ratio of $n_{O_2^+ (NO^+)}$ to n_e.

2.3.3 Evaluation of the ions' momentum equation

The author quantitatively evaluated each term in the momentum equation of ions to assess its contribution to the formation of low-altitude ion upflow. The ion momentum equation in the direction parallel to the magnetic field in the low-altitude ionosphere (250-400 km) is the same expression as in the previous study [Kosch et al., 2010]:

$$\frac{\partial V_i}{\partial t} = -\nu_{in}(V_i - V_n) - \frac{1}{n_e m_i}\frac{\partial (n_e k_B T_i)}{\partial s} - \frac{1}{n_e m_i}\frac{\partial (n_e k_B T_e)}{\partial s} - g\cos\alpha \tag{2.17}$$

where V_i and V_n are the bulk velocity components parallel to the magnetic field for ions and neutrals, respectively; ν_{in}, n_e, m_i, and k_B represent the ion-neutral collision frequency, the electron density, the mean ion mass, and the Boltzmann constant, respectively. T_i and T_e indicate the ion and electron temperatures, respectively; and s, g, and α represent the upward distance projected along the field-aligned direction, the

gravitational acceleration, and the angle between the magnetic field line and vertically downward direction, respectively. At the location of the EISCAT observation, α was $\sim 12°$. The author assumed $V_n = 0$ because of no observational data in the following assessment.

In this study, the author assumed that only O^+ and molecular ions (O_2^+ and NO^+) composed the ions in the low-altitude ionosphere based on the IRI 2016 model [Bilitza et al, 2016]. The author calculated the O^+ ion density ratio n_{O^+}/n_e using the IRI model and determined the molecular ion density n_M as the difference between electron density and the O^+ ion density,

$$n_M = n_e \left(1 - \frac{n_{O^+}}{n_e}\right). \tag{2.18}$$

ν_{in} was estimated based on the ion-neutral collisional model (Schunk and Nagy, 2009):

$$\nu_{in} = \left\{3.67\times10^{-11} n_{\mathrm{O}} \left(\frac{(T_i + T_n)}{2}\right)^{\frac{1}{2}} \left(1 - 0.064 \log_{10} \frac{(T_i + T_n)}{2}\right)^2 + 6.82\times10^{-10} n_{\mathrm{N_2}}\right\} \frac{n_{\mathrm{O^+}}}{n_e} \tag{2.19}$$
$$+\left\{2.31\times10^{-10} n_{\mathrm{O}} + 4.13\times10^{-10} n_{\mathrm{N_2}}\right\} \frac{n_M}{n_e} [\,\mathrm{s^{-1}}]$$

where n_{O}, $n_{\mathrm{N_2}}$, and $n_i\ (\sim n_e)$ indicate the densities of neutral O, N_2, and ions, respectively. T_i and T_n show the ion and neutral temperatures, respectively. Neutral density and temperature were estimated by using the neutral upper atmosphere model: the Naval Research Laboratory Mass Spectrometer and Incoherent Scatter Radar Exosphere (NRLMSISE-00) model [Hedin, 1991; Picone et al., 2002]. Based on the model, the author considered only O and N_2 as neutral species that could affect molecular ion density in this altitude range. Each reaction coefficient was set for the O_2^+ case in the above equation of ν_{in}. In the NO^+ case, the factors in the last term of the equation were changed from 2.31 to 2.44 and from 4.13 to 4.34.

Section 2.4 Method for a statistical study

2.4.1 Instrumentation and data set for examples

The author used two EISCAT radars: The EISCAT Ultra High Frequency (UHF) radar at Tromsø ($69°35'$ N, $19°14'$ E, Invariant Latitude: $66°12'$ N) and the EISCAT

Svalbard 42m antenna (ESR) radar at Svalbard (78°09′ N, 16°03′ E, Invariant Latitude: 75°10′ N), which are introduced in Section 2.2.1.

To show an example on Type 1 and Type 2 ion upflows in the lower ionosphere observed by the EISCAT Tromsø UHF radar, the author derived ionospheric plasma parameters such as the electron density, ion and electron temperature, and ion velocity from the autocorrelation function of the EISCAT UHF radar data by using the Grand Unified Incoherent Scatter Design and Analysis Package (GUISDAP) [Lehtinen and Huuskonen, 1996]. The author obtained observational data with the EISCAT UHF radar in 'beata' mode along the magnetic field line, as the resolution was 1 min for time and 3 km (70-120 km), 10 km (120-150 km), 20 km (150-250 km) and 30 km (250-600 km) for altitude.

2.4.2 Super epoch analysis

For a statistical analysis based on the EISCAT long-term observations, the author selected data obtained by the EISCAT UHF radar and the ESR42m radar at the altitudes from 250 to 350 km while the EISCAT radars looking along the local magnetic field line during geomagnetic storms between 1996 and 2015. The author integrated autocorrelation function data and obtained PSD for 5 min. After the derivation of ionospheric physical parameters from PSD every 5 minutes, the author averaged those parameters between 250 km and 350 km for altitude. In order to exclude unrealistic values, the author also screened the data before taking the average with following criteria: Absolute value of the ion velocity was less than 1500 m/s, the ion and electron temperatures were less than 10000 K, the electron density was more than 10^{10} m^{-3} and less than 10^{13} m^{-3}, error values of the ion temperature and electron temperature were less than 50 %, and the quality value was 0, which means available data. The author prepared all data set which was the same as the previous study [Ogawa et al., 2019] for the period and magnetic storms, but not for the altitude range and the criteria of screening data because the ionospheric conditions are different between lower and higher altitudes.

Chapter 3 Event study

Section 3.1 Introduction

Molecular ions in the inner magnetosphere have been observed since the first report by AMPTE/IRM [Klecker et al., 1986]. They showed that the flux ratio of the molecular ions to O^+ was approximately a few percent (2-4%). Recently, a statistical study of molecular ions in the ring current observed by the Arase (ERG) satellite has shown that molecular ions almost always exist during geomagnetically active periods of the Dst index less than -40 nT [Seki et al., 2019]. It is considered that molecular ions in the ring current are transported mainly throughout the magnetotail region, as with O^+ ions. However, the supply mechanisms of these molecular ions to the ring current are far from understood especially in the deep ionosphere, which is the source region of molecular ions.

Molecular ions usually exist only in the low-altitude (< 300 km) ionosphere. If there is no rapid upward transport due to ion upflows [e.g., Wahlund et al., 1992; Ogawa et al., 2009, 2013; Ji et al., 2019], the contribution of molecular ions remains less than ~0.1% of O^+ at ~300 km as shown in the IRI 2016 model [Bilitza et al, 2016]. The ion species ratio is less than that observed in the magnetosphere. As pointed out by Peterson et al. (1994), the rapid upward transport of ionospheric ions from the low-altitude ionosphere against the loss by dissociative recombination is needed to make the molecular ions escape to the magnetosphere. How to cause rapid ion upflows from the low-altitude ionosphere is one of the critical issues to understand the supply mechanisms of the molecular ions to the magnetosphere.

For the formation of the rapid ion upflow from the low-altitude ionosphere, the ionospheric ions need to be transported upward against the gravitational force by heating mechanisms: ion frictional heating (Joule heating), particle precipitation, small or large scale plasma instabilities [e.g., Peterson et al., 1994; Liu et al., 1995; Davies and Robinson, 1997; Kosch et al., 2010; Kistler et al., 2019]. The necessary upflow velocity becomes large below 300 km altitude since the transport should be fast enough to overcome a large dissociative recombination rate, which causes rapid loss of molecular ions in this altitude range [Wilson et al., 1999]. Assessment of each candidate

heating process by Peterson et al. [1994] showed that none of the heating processes can provide enough energy. They suggested that a remaining candidate might be small-scale plasma instabilities as introduced in Section 1.3.3.

To understand the supply mechanisms of the molecular ions to the magnetosphere, the author reports observations of molecular ions in the inner magnetosphere by the Arase (ERG) satellite during a magnetic storm starting on September 7, 2017 and a rapid ion upflow in the low-altitude ionosphere (250-350 km) by the EISCAT radar on September 8, 2017 during the magnetic storm. The explanation of instrumentation and the data analysis method are introduced in Section 2.3, the observational results are shown in Section 3.2, followed by discussion in Section 3.3 and our conclusions in Section 3.4.

Section 3.2 Result

3.2.1 Arase(ERG) satellite observation

The instrumentation and data set are described in Section 2.3.1.

Figure 3.1 shows the time variations of the geomagnetic indices and the Arase satellite observations between 8:00 UT on September 7 and 00:00 UT on September 10, 2017. As shown in Figure 3.1a-b, the geomagnetic activities were high, and the double peak of the Dst index corresponds to the first and second main phases of the magnetic storm. MEP-i was operated in the TOF mode. The energy-time spectrograms for all ion species indicate periodic energy dispersions, suggesting continuous ion injections into the inner magnetosphere. The author can confirm a clear peak of the molecular ion population during each period. One of the confirmed results is shown in Figure 3.1g. After subtraction of the O^+ contamination by the fitting method presented in Seki et al. [2019], the energy density (ED) ratio of molecular ions to O^+ was calculated. The ED ratio shown in Figure 3.1f indicates that the molecular ions were intermittently observed by Arase in four orbits during this magnetic storm, when TOF mode was operated from 4 UT on September 8 to 17 UT on September 9, 2017. This suggests that there was a continuous molecular ion supply from the low-altitude ionosphere during the magnetic storm. In particular, the molecular ions were equivalent to approximately a few percent of O^+ from

14:00 to 18:00 UT on September 8 (displayed by the red box), which corresponds to the second main phase of the magnetic storm. In this period, the Arase satellite moved from Lm ≈ 2.2 to 8.0, MLT ≈ 14.3 to 19.9 hours and MLAT ≈ 5.7 to 29.2 degrees and observed molecular ions mostly in the ring current. Note that Lm was calculated as the Mcllwain-L value [Mcllwain, 1961] based on the International Geomagnetic Reference Field (IGRF) model [Thébault et al., 2015]. Geomagnetic disturbance was also considered to be significantly active during the period, and many molecular ions were supplied from the ionosphere. In fact, EISCAT observed an ion upflow in the low-altitude ionosphere.

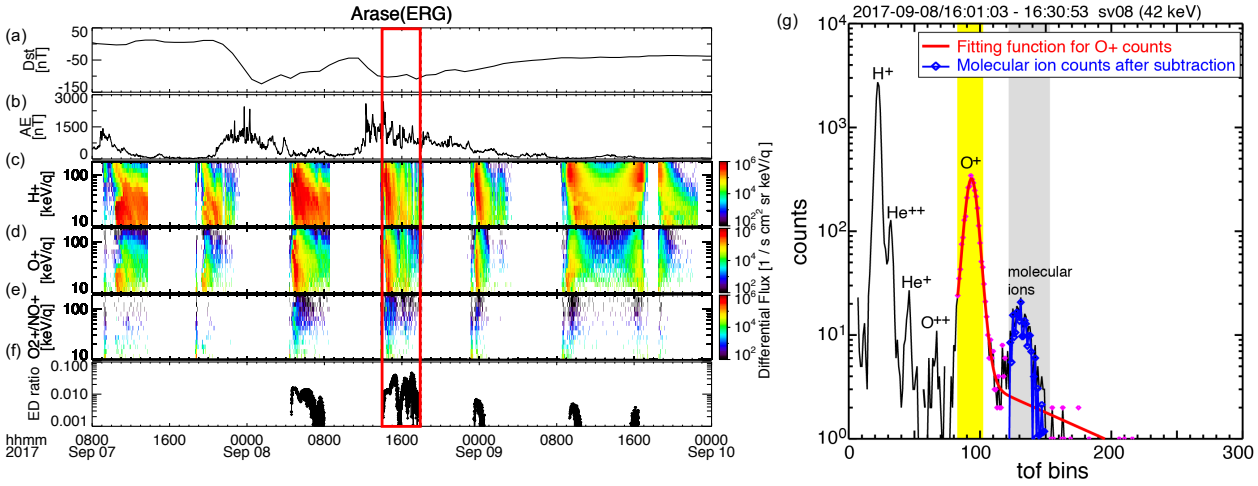

Figure 3.1: Summary plots of time variations of the Dst index, AE index, and ion differential flux observed by the Arase (ERG) satellite during the magnetic storm started on September 7, 2017. From top to bottom, each panel shows the (a) Dst index, (b) AE index, energy time diagrams for (c) H^+, (d) O^+, and (e) molecular ions (O_2^+, NO^+, N_2^+) observed by MEP-i, and (f) energy density ratio of the molecular ions to O^+. (g) Raw TOF (time-of-flight) count data at an energy of 42 keV/charge are shown in the same format as Figure 2 in Seki et al. [2019]. The red line shows the fitting function for O^+ counts derived from several data points (magenta symbols). After subtraction of O^+ contamination, the blue symbols with lines are derived. MEP-i = medium-energy particle experiments-ion mass analyzer.

3.2.2 EISCAT radar observation

The instrumentation and data set are described in Section 2.3.1.

As shown in Figure 3.2d, an ion upflow from 200 km to 400 km was observed by EISCAT between 16:15-16:18 UT on September 8, 2017. Figure 3.2b-c indicate that the electron temperature was enhanced by ~1500 K at ~110 km altitude and that ions were heated to >2000 K in the 200-400 km altitude range. The electron temperature usually has the largest error among the four parameters. Figure 3.2e indicates that the physical parameters were determined within the ~10% errors at the altitudes of interest: ~110 km and 250-350 km. The effect of noise was almost negligible because of the sufficiently high electron density as shown in Figure 3.2a. Thus, these parameters were well defined, and the author concluded that the upflow and accompanied features are significant enough even if error bars are considered. During the upflow event between 16:15-16:18 UT, a pronounced feature is the strong ion heating and resultant temperature increase in the wide altitude range from the low altitude. Another remarkable feature during the upflow event is the electron temperature enhancement at an altitude of approximately 110 km. The author can estimate the strength of convection electric fields from the electron temperature enhancement on the magnetic flux tube based on an empirical relation between the electron temperature and the electric field based on the statistical study by Davies and Robinson [1997]. As described in details in Davies and Robinson [1997], the convection electric field can be estimated from the electron temperature enhancement at an altitude of ~110 km, where the increase in electron temperature is almost proportional to the perpendicular electric field strength above 20 mV/m. The altitude corresponds to the E-region where the electron heating is most pronounced. However, the convection electric field itself was induced from the magnetosphere and enhanced at whole altitudes, including the region of the upflow. As shown in Figure 3.2f, the estimated convection electric field reached ~80 mV/m during the upflow event. This means that there was enhancement of the convection electric field by a factor of 2 during the event. The upflow event started at altitudes less than 250 km, where the molecular ions are abundant in the ionosphere. Thus, the low-altitude ion upflow can potentially contribute to the supply of molecular ions to the magnetosphere observed by Arase.

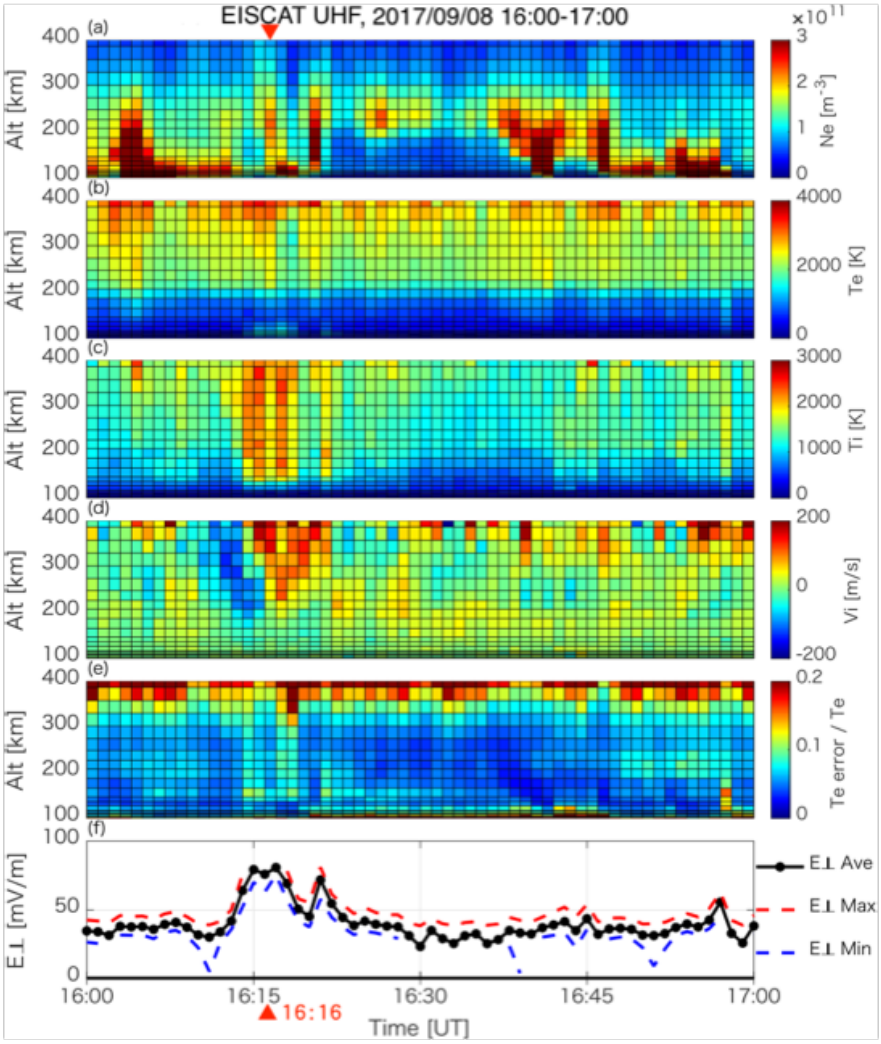

Figure 3.2: EISCAT observations during 16-17 UT on September 8, 2017. From top to bottom, each panel shows (a) electron density, (b) electron temperature, (c) ion temperature, (d) ion velocity, (e) error ratio of electron temperature, and (f) electric field perpendicular to the magnetic field derived from electron heating at 111 km altitude based on empirical relations reported by a previous statistical study [Davies and Robinson, 1997].

3.2.3 Estimations of the molecular ion flux

The analysis method is described in Section 2.3.2

Next, the author estimated the density and flux decreases of molecular ions (O_2^+ and NO^+) due to the dissociative recombination during the ion upflow from the low altitude observed at 16:16 UT as indicated by the red arrow in Figure 3.2. EISCAT observed the fast ion upflow (Vi > ~100 m/s) along the magnetic field line from the low-altitude ionosphere (< 300 km). In addition to that, the data set was also well-defined, i.e., the error ratio of electron temperature was smaller than 0.1, because the electron density was high and its density profile smoothly connected at each altitude. Thus, this event is worth analyzing how the fast upflow could remain molecular ions. As described in Section 2.3.2, starting with the density or flux observed by EISCAT at 280 km altitude, its decrease in the course of the ion upflow with the observed velocity to 350 km altitude was estimated. As shown in Figure 3.3c-d, the density decrease due to the dissociative recombination loss was approximately two orders of magnitude from 280 km to 350 km for O_2^+, and the remaining density and upward flux at 350 km altitude were ~10^8 m^{-3} and ~10^{10} $m^{-2}s^{-1}$, respectively. The resultant O_2^+ density of ~10^8 m^{-3} at 350 km altitude transported by the ion upflow from the low altitude was much higher than that expected from an empirical ionospheric model such as the IRI 2016 model [Bilitza et al, 2016]. The results also indicated that the loss of NO^+ due to the dissociative recombination was much faster than that of O_2^+. It should be noted that the author did not consider any ion production in the estimation and the resultant remaining density or flux at the altitude of 350 km should be regarded as the minimum value for the molecular ions transported to the source region of the ion outflows. Additionally, note that the effects of recombination loss became less important at altitudes above 350 km due to the low electron density.

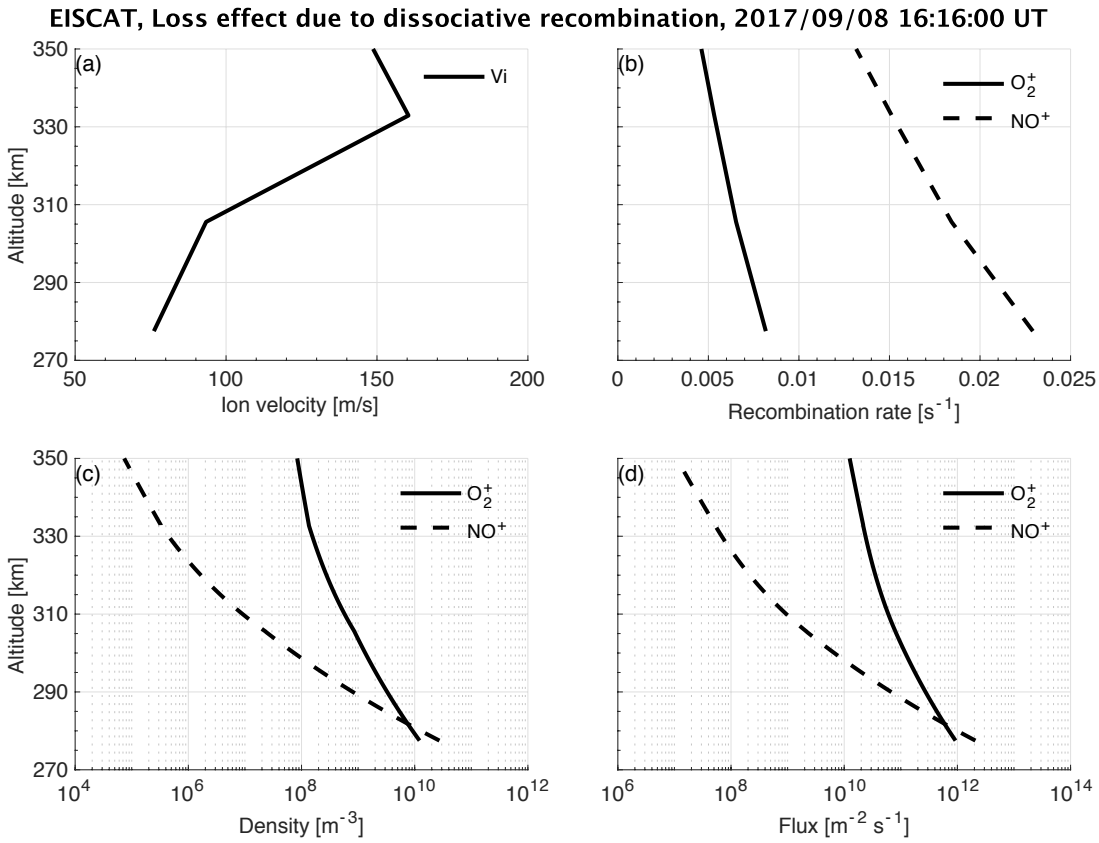

Figure 3.3: Estimation of the O_2^+ and NO^+ density decreases due to dissociative recombination against altitude at 16:16 UT on September 8, 2017 based on EISCAT observations indicated by red triangles in Figure 3.2. The top two panels show the ion velocity (a) and the recombination rate (b), which was used in each estimation for O_2^+ (solid line) and NO^+ (dashed line). The ion velocity in panel (a) was derived by interpolation of EISCAT data, while the recombination rate in panel (b) was calculated based on the models [Terada et al., 2009] by using observational electron temperature and density. The solid (dashed) lines in the bottom two panels show the estimated O_2^+ (NO^+) density (c) and flux (d). Note that, no production of ions is considered in the estimation.

3.2.4 Evaluation of the ions' momentum equation

The analysis method is described in Section 2.3.3.

As shown in Figure 3.4a-b, the density and temperature observations during the time period are smooth enough to take their gradients. In Figure 3.4c, the author can see the positive velocity (~50-150 m/s) between 250 and 350 km altitudes. This suggests that the ion upflow can transport molecular ions upward since the empirical atmospheric model indicates that there are significant molecular ions at an altitude of 250 km. In Figure 3.4d, the black line indicates that the ion and electron pressure gradients can almost balance with the gravitational force. On one hand, the collisional effect shown by the green line is strong enough to stop the ion upflow, if the author assumes no neutral velocity ($V_n \sim 0$ m/s) in the low-altitude ionosphere, where the neutral density is high. Note that, the author assumed no neutral wind in estimation of Figure 3.4d due to the lack of the neutral wind observations.

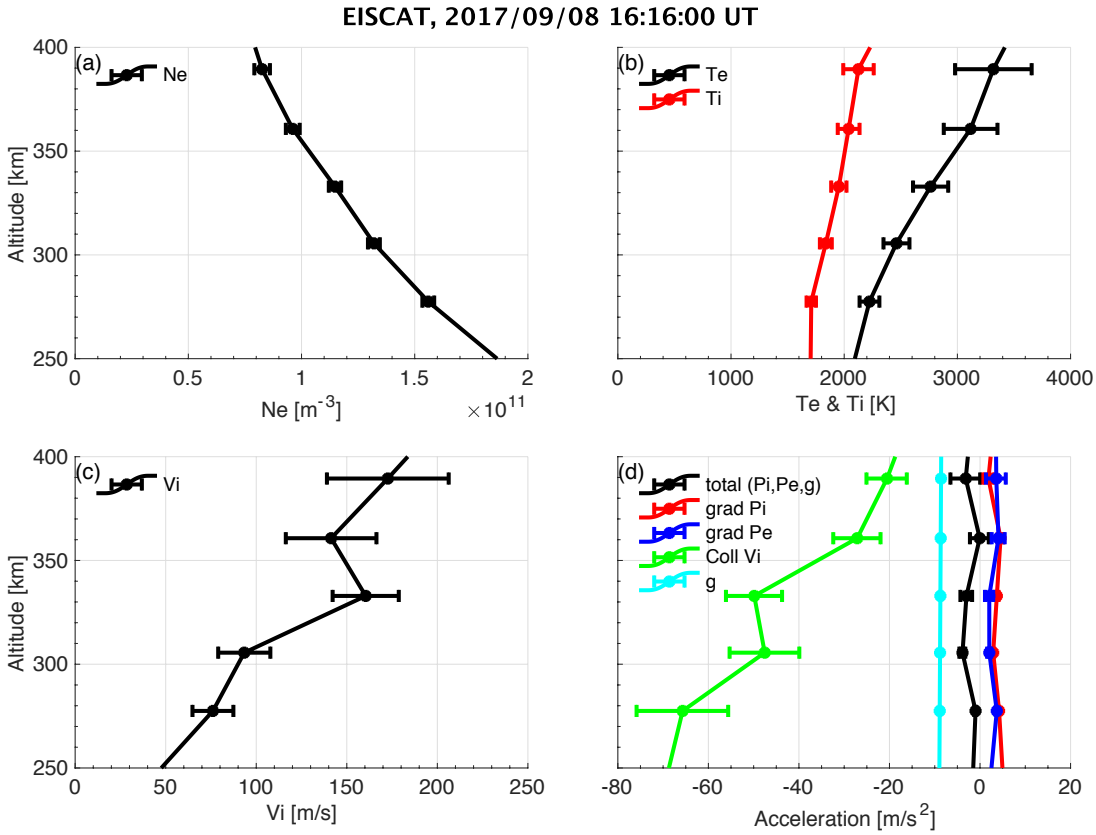

Figure 3.4: Summary of evaluation of each term in the ion momentum equation based on the EISCAT observations of the ion upflow at 16:16 UT on September 8, 2017. The electron density (a), electron and ion temperature (b) and ion velocity (c) observed by EISCAT are plotted against altitude. The right bottom panel (d) shows acceleration terms in the equation of motion [Eq. 2.17 in the text]: the ion (red line) and electron (blue) pressure gradients, neutral collisional effect (green), gravitational force (light blue), and total acceleration except for the neutral collision effect (black)

Section 3.3 Discussion

Figure 3.4 shows that the strong downward force could affect the ion upflow when the author assumed no neutral velocity. If this situation continued, the downward drag force decelerated the ion upflow and stopped it in several tens of seconds. However, Arase observed the ion upflow in several minutes, as shown in Figure 3.2. Thus, the existence of the ion upflow might mean that the neutral atmosphere also had a similar upward velocity at the point of the ion upflow observation and keep the stable condition between pressure gradients and gravitational force.

This result suggests the different formation mechanisms of the low-altitude ion upflow from those in the higher altitude region (> 400 km). Kosh et al. [2010] reported that the electron pressure gradient with electron heating mainly caused the ion upflow above 400 km, where the ion-neutral collisional effect is negligible. However, the EISCAT observation reported here shows that enhanced ion and electron pressure gradients were not sufficient conditions to form the ion upflow in the low-altitude ionosphere. Neutral atmospheric dynamics are also important to generate the ion upflow. If it is assumed that neutrals had collided with ions very frequently and reached almost the same velocity as ions, the collisional effect could be negligible, and the pressure gradients of the ion and electron could be balanced with gravitational force, as shown by the black line in Figure 3.4d. This assumption is consistent with the observational result in Figure 3.2 because it is reasonable that ions were heated well in such a collisional case. In addition to that, the simulation study [Deng et al., 2019] showed that the neutral wind reached ~30 m/s at 300 km altitude with the increase of the neutral density under the ~1000 m/s westward convection flow, which means the existence of the several tens mV/m electric field. Thus, the assumption is not so unrealistic. In fact, the neutral wind could reach ~100 m/s within several seconds based on the order estimation of the momentum equation by using observed velocity ($V_i \sim 100$ m/s) and ion-neutral collisional frequency based on MSIS model ($\nu_{in} \sim 1\ \mathrm{s}^{-1}$) between 250 and 300 km. These discussions indicate the possibility that pressure gradients of the ions and electrons that were balanced with the gravitational force created the ion upflow under stable conditions after frequent collisions between ions and neutrals.

As introduced in Section 3.1, some heating mechanisms such as ion frictional heating

(Joule heating), electron heating by particle precipitation, and small or large scale plasma instabilities are candidates to form the ion upflow in the low-altitude ionosphere. The observational results suggest that the ion frictional heating was an important mechanism in this event. The ions were heated at a wide altitude range from ~200 to 400 km and the electric field was enhanced, as shown in Figure 3.2. Ions and neutrals frequently collide and can be heated if there is velocity difference in the region. The author considered that the enhanced electric field and the resultant $E \times B$ drift of ions initially created the velocity difference between ions and neutrals, and the drag force accelerated neutrals along the southward direction. Neutrals were heated and the enhanced neutral pressure gradient by heating and diffusion processes [c.f. Schunk, 1977; Zettergren et al., 2011; Strangeway, 2012] caused acceleration along the magnetic field line. The field-aligned component of neutral wind accelerated ions along the magnetic field until both ions and neutrals obtained the similar velocity. At the same time, ions were heated. The enhanced temperature resulted in an enhanced pressure gradient. Thus, the upward pressure gradient was almost balanced with the downward gravitational force when EISCAT observed the ion upflow in the low-altitude ionosphere.

A possible cause of the strong electric field enhancement is Sub Auroral Polarization Stream (SAPS), reported previously during magnetic disturbance periods [e.g. Foster et al., 2002; Kataoka et al., 2007; Clausen et al., 2012; Obana et al., 2019]. SAPS is the westward flow resulting from the $E \times B$ drift caused by enhanced global electric fields. The velocity reaches several hundred m/s and sometimes exceeds 1000 m/s. There were not any other optical observations around Tromsø in this event, and the author could not analyze more details. However, when the electric filed was globally enhanced as large as in Figure 3.2f, it was expected that the velocity of SAPS reached a typical velocity (~800-1600 m/s) from the IGRF model [Thébault et al., 2015]. This suggests a possibility that the ion upflow structure was related to SAPS. In addition, the downward velocity can be seen just before the ion upflow event in Figure 3.2. This structure reflected local convection with strong electric filed or soft precipitation of electrons. Such a spatial structure is part of the evidence that EISCAT observed a part of the ion upflow structure, which was globally transported due to the strong enhanced convection electric fields during the magnetic storm.

As pointed out by Peterson et al. [1994], it is usually difficult to transport significant molecular ions upward to the higher altitude above 300 km in the ionosphere since one

needs fast ion upflow to overcome the rapid loss by the dissociative recombination. In this event, the ion upflow continued from 250 to 400 km altitudes (Figure 3.2) and the estimated density ratio of molecular ions to O^+ was ~0.1% at 350 km (See Figure 3.3). This is much larger than the value obtained in the IRI model [Bilitza et al, 2016]. It means that the observed ion upflow could transport some molecular ions overcoming the dissociative recombination. Note that, the author here did not include a change in the ion composition ratio from the IRI model by heating and transporting the ions when the author derived the ionospheric plasma parameters in Figure 3.2, although it is expected that the density ratio of molecular ions to O^+ increased by the ion upflow. Some models of the ion temperature or composition should be included to determine the ion composition since we can derive only the ratio of the ion temperature to mass from the measurement of the ion acoustic lines by using the incoherent scatter technique, as reported in previous studies [e.g. Blelly et al., 2010; Zettergren et al., 2011]. However, there is still no definitive way to apply the models of the ion composition ratio to the incoherent scatter radar data analysis. Developing the models is not quite simple and requires many peripheral discussions on the effects of ion upflow. The composition change can be important. If the effect of molecular ion ratio increase is considered, it is expected that the ion and electron temperature will increase [Zettergren et al., 2011]. Thus, the ion and electron pressure gradients increase and the total force balance without a neutral collisional effect can become higher than in Figure 3.4. This is, however, not shown in this study. Further development of ion composition models and information about neutral wind will be needed if we determine the driving force more strictly as an observational result in the low-altitude ionosphere.

The estimated density ratio of molecular ions to O^+ was ~0.1% in the low-altitude ionosphere (Figure 3.3). On the other hand, the energy density ratio of molecular ions to O^+ reached several percent in the inner magnetosphere (Figure 3.1). This value is consistent with the result reported by Seki et al. [2019], where Dst was below -100 nT, which corresponds to a larger magnetic storm case in the statistical study. The molecular ion ratio to O^+ in the magnetosphere was larger than that estimated in the ionosphere. This might indicate that there are some selective acceleration mechanisms of molecular ions during the course of transport from the ionosphere to the magnetosphere. To estimate the necessary energy gain, the author compared the phase space density of molecular ions between EISCAT and Arase. The author estimated the O_2^+ phase space density in the

ionosphere assuming the Maxwellian distribution function or kappa distribution function of $\kappa = 3$ with the estimated O_2^+ density in Figure 3.3c ($\sim 1\times10^8$ m^{-3}), ion temperature ($\sim 2\times10^3$ K), and velocity ($\sim 2\times10^2$ m/s) observed by EISCAT around 350 km altitude at 16:16 UT on September 8, 2017. The O_2^+ phase space density in the ring current is estimated as ~8×10^{-13} s^3m^{-6} at their typical energy (~42 keV) from the Arase/MEP-i TOF-mode data observed between 16:00 and 16:30 UT (See Figure 3.1g). According to Liouville's theorem, the phase space density should be preserved throughout the path from the ionosphere into the inner magnetosphere without collisional processes. The observed phase space density value at the typical energy of ~42 keV in the ring current corresponded to that at ~10 eV (~100 eV) of the Maxwellian (kappa) distribution function in the ionosphere. This indicates that the molecular ions have undergone about three orders of magnitude acceleration on their way from the ionosphere to the inner magnetosphere. It is larger than the typical acceleration by the auroral potential drops [e.g. Carlson et al., 1998]. A possible scenario might be that these ions experienced multiple acceleration processes as there were transported into the magnetotail plasma sheet and then to the inner magnetosphere. However, it should be noted that the ring current ions can undergo collisional loss process such as the charge exchange and the above comparison based on Liouville's theorem process might be too simplified. Usage of a phase space density peak, ignoring the pitch angle distribution, in the ring current may result in overestimation of the phase space density. Thus, the necessary acceleration may be smaller than the above estimation. Further investigations by a simulation will be needed for more quantitative comparisons.

Figure 3.2 also shows the upward velocity without enhancement of the ion temperature and electric field after the featured upflow event. In particular, the electron density was strongly enhanced at 16:20 UT. This enhancement was caused by precipitation but the fast upflow (~100 m/s) occurred above 330 km. This fact indicates that the precipitation does not always correlate the low-altitude ion upflows, which can transport the molecular ions.

Section 3.4 Summary

The author investigated molecular ions (O_2^+/NO^+/N_2^+) observed by the Arase (ERG) satellite and EISCAT radar during the magnetic storm starting on September 7, 2017.

Arase observed molecular ions in four orbits in the inner magnetosphere during the magnetic storm. This indicates that there was a continuous molecular ion supply from the ionosphere. In particular, EISCAT radar observed an ion upflow in the low-altitude (<300 km) ionosphere during the storm main phase around the second Dst minimum on September 8, which can be one of the sources of molecular ions in the magnetosphere. During this event, the Dst and AE indices were ~-100 nT and ~1000 nT, respectively. The author analyzed EISCAT data and revealed mechanisms of the ion upflow. The results can be summarized as follows:

- The EISCAT radar observed an ion upflow event ($V_i \cong 100$ m/s) in the low-altitude (250–350 km) ionosphere.
- High ion temperature ($T_i > 2000$ K) in the altitude range between 250-400 km, where the ion upflow occurred, and high electron temperature ($T_e \cong 1500$ K) at 110 km altitude were observed with the ion upflow.
- The convective electric field estimated from the T_e at ~110 km shows a significant enhancement by $E_\perp \cong 80$ mV/m.
- The estimation of upward O_2^+(NO^+) flux based on the observational upflow velocity and the loss rate due to the dissociative recombination indicates that the molecular ion flux at 350 km altitude can remain high (>10^{10} m^{-2} s^{-1}).

The evaluation of each term in the momentum equation of ions along the field aligned direction indicates that a possible formation scenario of the low-altitude ion upflows is: Enhancement of the convection electric field and resultant frictional heating associated with SAPS and drag acceleration of neutrals reached an equilibrium to cause the ion upflow where the upward ion and electron pressure gradients are balanced with the downward gravitational force and the neutral velocity almost equals to ion velocity. These results suggest that rapid upward transportation of the molecular ions from the low-altitude ionosphere due to the ion upflow caused by the strong ion frictional heating during the magnetic storm provides a source of molecular ion outflows at higher altitudes to supply these ions to the magnetosphere.

Chapter 4 Statistical study

Section 4.1 Introduction

A large number of studies for O^+ have investigated ion upflow and outflow since the first discovery of significant O^+ fluxes escaping from the ionosphere [e.g. Shelley et al., 1972; Yau et al., 1997; André et al., 1997; Ogawa et al., 2009; Ji et al., 2019]. In particular, their dependence on solar activities is one of the important properties to understand formation mechanisms of the ion upflows. In a previous study by Ogawa et al. [2019], the characteristics of O^+ ion upflows in the polar ionosphere were investigated during CIR- and CME-driven magnetic storms by using EISCAT radars. They reported that the upflows during CIR- and CME-driven storms have different dependence on magnetic local time as introduced in Section 1.3.1. Their study focused on the ion upflows in the altitude range between 400 and 500 km, where O^+ is the dominant species, and responses of the ion upflows to the different type of magnetic storms in the low-altitude ionosphere, where molecular ions exist, are far from understood.

It is also important to reveal the fundamental mechanisms of the ion upflows for the escape process. The candidate mechanisms of ion upflows can be mainly categorized into two types: Type1 ion upflows by the ion-neutral frictional heating and Type2 upflows by the particle precipitation. For the case of Type1 upflows, the difference between ion and neutral velocities caused by the enhancement of the electric field heated up the ions and the vertical ion pressure gradient increase. For the case of Type2 upflows, precipitations of energetic particles such as high-energy electrons from the nightside inner magnetosphere ionize ionospheric atmosphere and moving upward electrons pull up ions via the ambipolar electric field [c.f., Section 1.3.2]. Regarding to general properties in the polar ionosphere, Ogawa et al. [2019] suggested that the precipitation affected the generation of the ion upflows around the auroral oval and the development of the global currents such as Region1 field-aligned currents caused frictional heating during CIR- and CME- driven magnetic storms. Those mechanisms are often considered for O^+ ion upflows in the higher altitude ionosphere (> 400km) but the mechanisms are also effective for molecular ions, which exist in the low-altitude

ionosphere (< 300 km). For example, Takada et al. [2021] revealed that the frictional heating caused ion upflows in the low-altitude ionosphere, which was enough rapid to transport molecular ions upward overcoming the dissociative recombination. However, the general properties of the mechanisms such as dependence on MLT and the magnetic storm type have been not investigated in the low-altitude ionosphere during storm time periods.

The purpose of this study is thus to understand effects of CIR- and CME-driven magnetic storms on ion upflows and their mechanisms in the low-altitude ionosphere based on long-term observations of the EISCAT radars in 20 years. The explanation of instrumentation and the data analysis method are introduced in Section 2.4, the observational results are shown in Section 4.2, followed by discussion in Section 4.3 and our conclusions in Section 4.4.

Section 4.2 Result

4.2.1 Examples of the Type1 and Type2 upflows

The instrumentation and data set are described in Section 2.4.1.

Figure 4.1 shows the examples of Type 1 and Type 2 ion upflows in the lower ionosphere (100-400km), where molecular ion exists. As shown in Figure 4.1d, Type 1 upflow was observed between 19:40-19:50 UT on October 13, 2018 (seen in the left figure) and the Type 2 upflow was observed between 01:14-01:22 UT on September 24, 2019. Comparing with Type 1 and Type 2 ion upflows, Type 1 upflow was characterized by the strong ion temperature enhancement with the enhancement of the electron temperature at 110 km as shown in Figure 4.1c and Figure 4.1f. The enhancement of the electron temperature at ~110 km corresponds to convection electric fields [c.f., Section 2.2.3]. On the other hand, Type 2 upflow was characterized by the enhancement of electron density and electron temperature as shown in Figure 4.1a-b.

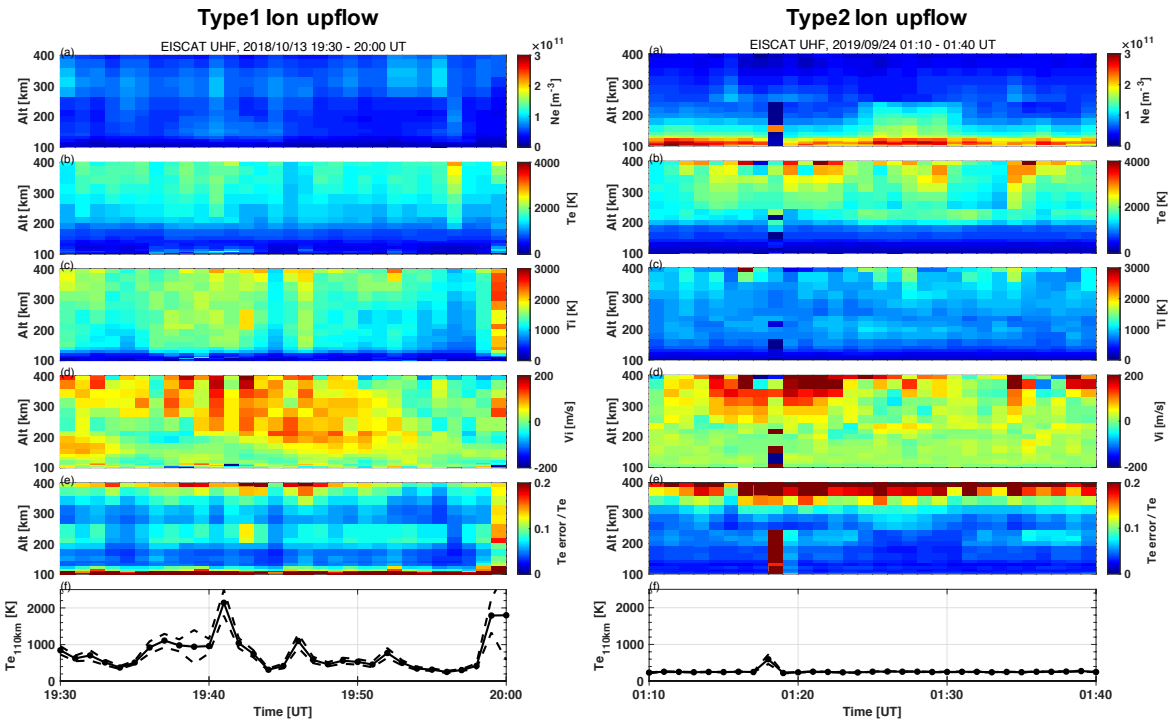

Figure 4.1: The example of type 1 and type 2 ion upflows in the lower ionosphere observed by the EISCAT UHF radar. From top to bottom, each panel shows (a) electron density, (b) electron temperature, (c) ion temperature, (d) ion velocity, (e) error ratio of electron temperature, and (f) electron temperature at 111 km altitude.

4.2.2 Super epoch analysis

The analysis method is described in Section 2.4.2.

The author investigated the low-altitude ionospheric parameters during magnetic storms and its dependence on the Days from storm. The definitions and derivation techniques of each data point and parameters such as Days from storm and MLT are same as used in the previous study [Ogawa et al., 2019] except for altitudes and prepared data set after screening, which was introduced in Section 2.4.2. For example, the onset time is defined as the arrival time of the shocks (stream interface) for CIR-/CME- driven storms.

Figure 4.2 shows results of the epoch analysis on CIR-driven storm cases at Tromsø. The author classified the magnetic storms by the value of Dst minimum. The number of data is 440-1640 for each point. An averaged value was derived from the data during more than two magnetic storms for each point, that is, a blank means only one or two magnetic storms, or even no storms. The author defined CIR-driven small magnetic storms at Tromsø as the value of Dst minimum is more than -60 nT and large magnetic storms as less than -60 nT. Top (bottom) four panels a1-d1 (a2-d2) show the results about ion velocity, ion flux, ion temperature, and electron temperature during CIR-driven small (large) magnetic storms. As shown in Figure 4.2a1 and Figure 4.2b1, ion upward velocity ($Vi \sim 37$ m/s) and flux ($Flux \sim 3\times10^{12}$ m^{-2}/s) were generated after storm onset during CIR-driven small storms in nightside (black line). These upwelling occurred with the ion temperature enhancement and strong enhancement of the electron temperature as shown in Figure 4.2c1 and Figure 4.2d1. The similar increase on temperatures could be detected in duskside (cyan line) but it just generated ion upward velocity slightly and even no flux on average. During large magnetic storms (Figure 4.2a2-d2), also the ion upward velocity and flux were generated with the enhancement of ion and electron temperatures in nightside. In addition to that, ion upflows were detected in dawnside with only ion temperature enhancement.

Figure 4.3 is same as Figure 4.2 except for CME-driven magnetic storms and the criteria on the Dst minimum. The number of data is 130-740 for each point. An averaged value was derived from the data during more than two magnetic storms for each point, that is, a blank means only one or two magnetic storms, or even no storms. The author defined CME-driven small magnetic storms at Tromsø as the value of Dst minimum is

more than -150 nT and large magnetic storms as less than -150 nT. During small magnetic storms (Figure 4.3a1-d1), the similar characteristics can be seen as shown in Figure 4.2a1-d1. The ion velocity (flux) reached ~51 m/s (~10×10^{12} m^{-2}/s) with the ion temperature enhancement and strong enhancement of the electron temperature in nightside after the storm onset. Figure 4.3a2-d2 shows the results from the larger magnetic storm cases. The ion upflows were detected in nightside and dawnside. The ion velocity (flux) reached ~58 m/s (~7×10^{12} m^{-2}/s) with only ion temperature enhancement in nightside. The ion velocity (flux) reached ~46 m/s (~4×10^{12} m^{-2}/s) with only ion temperature enhancement in dawnside. The dayside velocity and flux indicate the downward flow even after the storm when the ion temperature was enhanced.

Figure 4.4 shows the results from the ESR42m radar during CIR-driven magnetic storms. The format is the same as Figure 4.2. The number of data is 370-1190 for each point. An averaged value was derived from the data during more than two magnetic storms for each point. The author defined CIR-driven small magnetic storms at Svalbard as the value of Dst minimum is more than -50 nT and large magnetic storms as less than -50 nT. During small magnetic storms (Figure 4.4a1-d1), the small enhancements of the ion velocity and flux can be seen in dawnside. The ion velocity (flux) reached ~22 m/s (~2×10^{12} m^{-2}/s) with the ion and electron temperature enhancement. On the other hand, Figure 4.4a2-d2 shows that there was no ion upflow on average during large storms. In particular, there was no enhancement of the electron temperature in dawnside compared with small cases. In addition to those features, there are common characteristics on enhancements of the ion and electron temperatures during both small and large storms in dayside even if there was no upflow.

Figure 4.5 is the same as Figure 4.4 except for CME-driven magnetic storms and no classification based on Dst index due to the small number of data set. The number of data is 190-750 for each point. An averaged value was derived from the data during more than two magnetic storms for each point. Almost all available data were obtained during large magnetic storms when the author set the criteria as Dst index equals to -100 nT, which was used in Ogawa et al. [2019]. Figure 4.5 indicates that there were upflows in nightside after storm onset. The averaged ion velocity was ~31 m/s and the flux was ~9×10^{12} m^{-2}/s. The downward velocity and flux become stronger with the ion temperature enhancement after storm onset.

Finally, the author estimated the effect of the convection electric fields on the

ion upflow to determine the mechanisms. The author investigated the enhancement of electron temperature at ~110 km as the index of the electric fields' enhancement [cf., Section 2.2.3]. The author defined the effective convection electric fields as the electron temperature at ~110 km is higher than 400 K, which corresponds to ~40 mV/m of the electric fields based on the previous work by Davies and Robinson [1997]. Figure 4.6a-d show the results of the estimation based on observations by the UHF radar at Tromsø. As shown in Figure 4.6a-b, the effect of electric fields during storm time was remarkable in duskside during both CIR-driven small and large storms and the enhancement in dawnside and duskside during CIR-driven large storms was more remarkable than during small storms. On the other hand, during CME- driven magnetic storms (see Figure 4.6c-d), the electric fields could strongly affect the ionospheric condition in dayside. The effect was also remarkable in dawnside and nightside during CME-driven large magnetic storms. Figure 4.6e-g show the results from the ESR42m radar at Svalbard. Figure 4.6e indicates that the electric fields were effective at all regions, especially for the dawnside and dayside cases, during small CIR-driven magnetic storms at Svalbard. As shown in Figure 4.6g, it was also remarkable during CME-driven storms in dawnside and dayside. However, the tendency in dawnside and duskside was more moderate for the large storm case in Figure 4.6f.

Figure 4.7 is the same as Figure 4.6 except for the criteria of electron temperature at ~110 km. In Figure 4.7, the author defined the effective convection electric fields as the electron temperature at ~110 km is higher than 800 K, which corresponds to ~60 mV/m of the electric fields based on the previous work by Davies and Robinson [1997]. Thus, Figure 4.7 represents the results when electric fields were strongly enhanced. The results show that the tendency of electric fields' enhancement is almost the same between moderately and strongly enhanced cases. However, there are small differences between them. One is shown in the case of the CIR-driven large storms at Tromsø. Figure 4.7b shows that there was little enhancement of electric fields after storm onset in dawnside and nightside although the enhancement is clearly shown in Figure 4.6b. The other is shown in the case of the CME-driven storms at Svalbard. Figure 4.7g shows that there was a peak after the storm onset in nightside although there was no clear enhancement of electric fields in Figure 4.6g. These results suggest that not strongly but moderately enhanced electric fields play an important role in those cases.

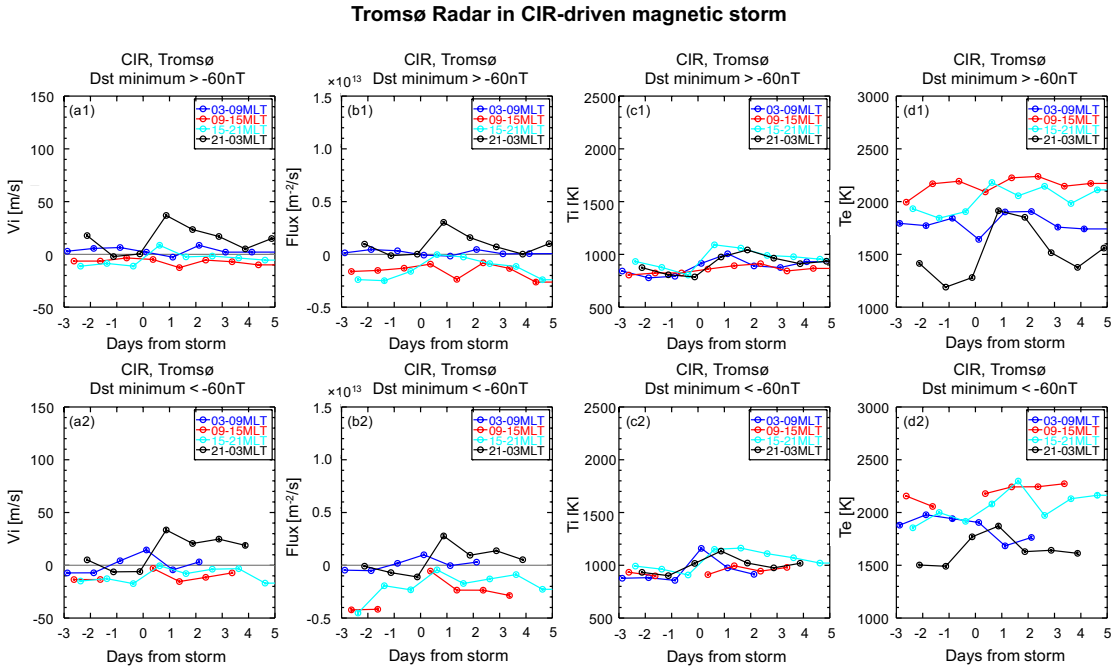

Figure 4.2: The results from the epoch analysis based on the data obtained from the EISCAT UHF radar at Tromsø during CIR-driven magnetic storms between 1996 and 2015. Top side panels show averaged (a1) ion velocity, (b1) ion flux, (c1) ion temperature, and (d1) electron temperature during small magnetic storms (Dst minimum > -60 nT). Bottom panels show averaged (a2) ion velocity, (b2) ion flux, (c2) ion temperature, and (d2) electron temperature during large magnetic storms (Dst minimum < -60 nT). The epoch days start with the moment when the shock reached. Averaged values at 03–09, 09–15, 15–21, and 21–03 MLT are plotted with blue, red, cyan, and black colors, respectively. Vertical bars indicate the standard errors of the mean. MLT at Tromsø is UT plus 2.5 hours. CIR = Corotating Interaction Region; MLT = Magnetic Local Time; UT = Universal time.

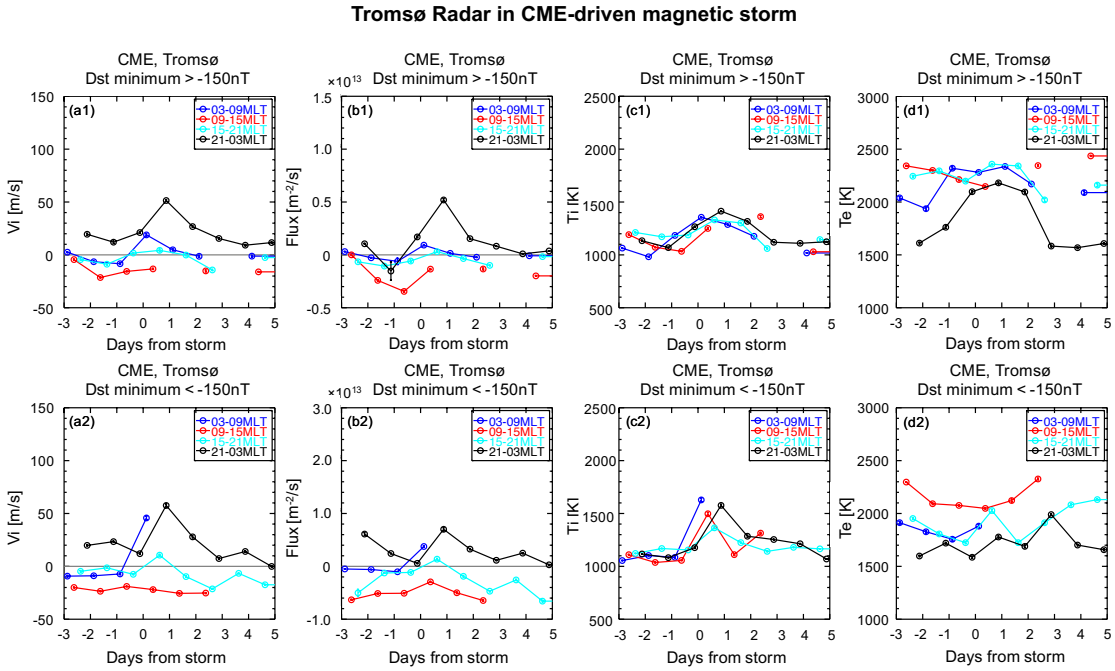

Figure 4.3: Same as Figure 4.2 except for CME-driven magnetic storms and the criteria on the Dst minimum: small storms are defined as Dst minimum > -150 nT and large storms are defined as Dst minimum < -150 nT. CME = Coronal Mass Ejection; MLT = Magnetic Local Time.

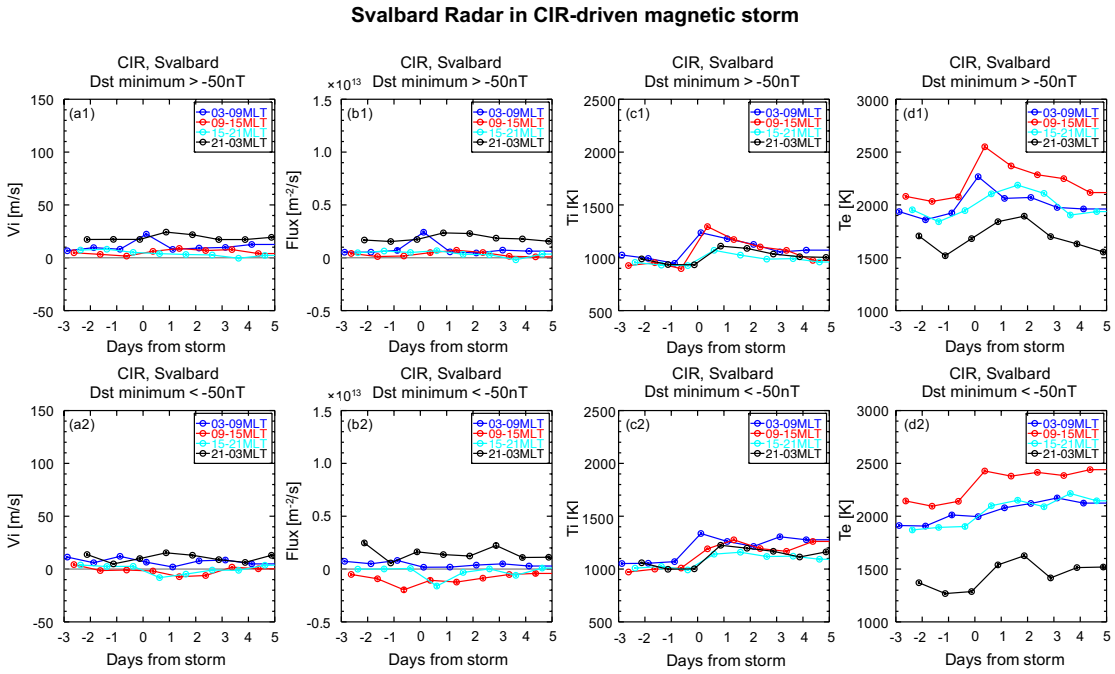

Figure 4.4: The results from the epoch analysis based on the data obtained from the EISCAT ESR radar at Svalbard during CIR-driven magnetic storms between 1996 and 2015. Top side panels show averaged (a1) ion velocity, (b1) ion flux, (c1) ion temperature, and (d1) electron temperature during small magnetic storms (Dst minimum > -50 nT). Bottom panels show averaged (a2) ion velocity, (b2) ion flux, (c2) ion temperature, and (d2) electron temperature during large magnetic storms (Dst minimum < -50 nT). The epoch days start with the moment when the shock reached. Averaged values at 03–09, 09–15, 15–21, and 21–03 MLT are plotted with blue, red, cyan, and black colors, respectively. Vertical bars indicate the standard errors of the mean. MLT at Svalbard is UT plus 2.8 hours. CIR = Corotating Interaction Region; MLT = Magnetic Local Time; UT = Universal time.

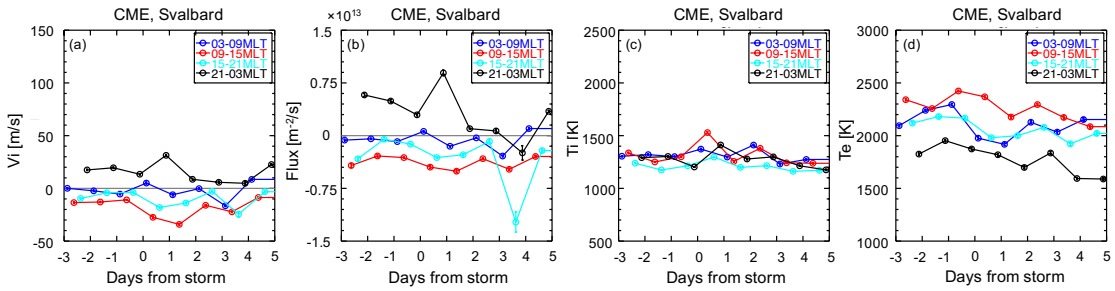

Figure 4.5: Same as Figure 4.4 except for CME-driven magnetic storms and no classification based on Dst index. CME = Coronal Mass Ejection; MLT = Magnetic Local Time.

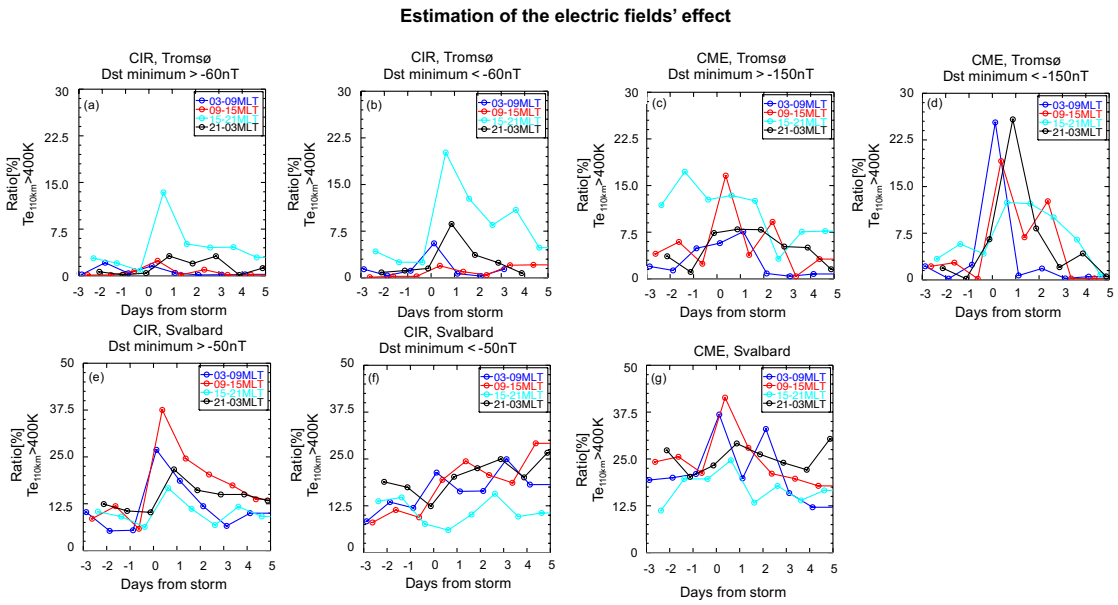

Figure 4.6: Estimations about the enhancement of convection electric fields. Each panel shows the ratio of the electron temperature at ~110 km higher than 400 K, which corresponds to the convection electric fields are higher than ~40 mV/m [Davies and Robinson, 1997], at each condition; in case of observations at Tromsø during CIR-driven (a) small magnetic storms, (b) large storms, CME-driven (c) small storms, and (d) large storms; at Svalbard during CIR-driven (e) small storms, (f) large storms, and (g) CME-driven storms. The epoch days start with the moment when the shock reached. Averaged values at 03–09, 09–15, 15–21, and 21–03 MLT are plotted with blue, red, cyan, and black colors, respectively. CIR = Corotating Interaction Region; CME = Coronal Mass Ejection; MLT = Magnetic Local Time.

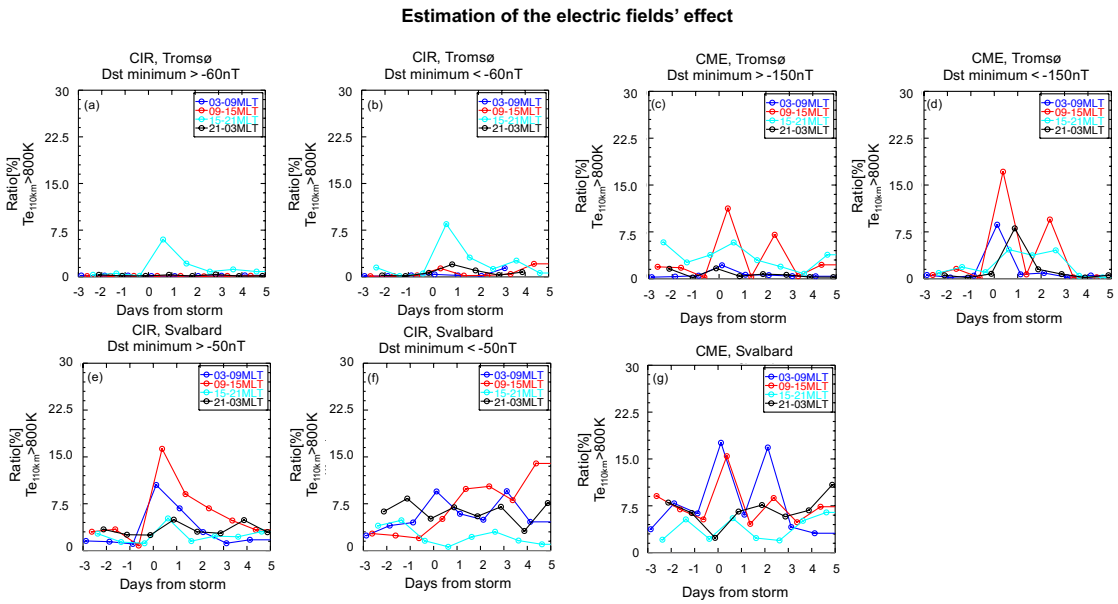

Figure 4.7: Estimations about the enhancement of convection electric fields. Each panel shows the ratio of the electron temperature at ~110 km higher than 800 K, which corresponds to the convection electric fields are higher than ~60 mV/m [Davies and Robinson, 1997], at each condition. Each panel has the same format as in Figure 4.6. CIR = Corotating Interaction Region; CME = Coronal Mass Ejection; MLT = Magnetic Local Time.

4.2.3 Summary tables for each MLT

The results during CIR-/CME-driven small and large storms, which were mentioned from Figure 4.2 to Figure 4.6 and reported by the previous study [Ogawa et al., 2019], are summarized from Table 4.1 to Table 4.4. Each table corresponds to the summary at each MLT. Table 4.1, Table 4.2, Table 4.3, and Table 4.4 are summary for the analysis respectively in dawnside, dayside, duskside, and nightside. Vi ($Flux$) refers to the value of ion velocity (flux) on 0 Days from storm, which indicate the upflows in the geomagnetically disturbing ionosphere during storm time periods. The low-altitude ionospheric parameters are based on from Figure 4.2 to Figure 4.5 in this study. The high-altitude ionospheric parameters have been reported in the previous study (See Figure 3, 5, and 6 in Ogawa et al. [2019]). "--" means no averaged data due to the small number of the data points or magnetic storms and "×" indicates that averaged ion velocity (flux) was less than ~10 m/s (~1×10^{12} m^{-2}/s). ΔTi (ΔTe) is defined as the difference about ion (electron) temperatures between after and before storm onset. The positive value means increase after storm onset compared to the pre-storm time. The ion temperature after storm onset refers to the value on 0 Days from storm and the ion temperature before storm refers to the averaged value from -3 to -1 Days from storm. The same definition is adopted for electron temperature. $\frac{Ti_{after}}{Ti_{before}}$ ($\frac{Te_{after}}{Te_{before}}$) is defined as the ratio of the ion (electron) temperature after storm onset to before storm onset. $R_{Te_{110km}}$ is the index of the electric fields' enhancement and refers to the value on the 0 Days from storm in Figure 4.6. $R_{Te_{110km}}$ is the ratio, where the electron temperature at ~110 km is higher than 400 K, which corresponds to ~40 mV/m of the electric fields based on the previous work by Davies and Robinson [1997]. A large $R_{Te_{110km}}$ when ion upflows were observed means the ion upflows were often detected with enhanced electric fields. $R_{Vi_{50}}$ ($R_{Vi_{100}}$) are the ratios of ion velocity, which are faster than 50 (100) after storm onset. If the ion upflow has a constant velocity ~50 (~100) m/s between 250-350 km, the upward O_2^+ flux remains $\sim7\times10^7$ ($\sim1\times10^{10}$) m^{-2}/s as a minimum value of the source of molecular ion upflow and outflow in the high-altitude ionosphere, where the author assumed the same condition in Section 3.2.3 except for the velocity. The author also investigated the conditional occurrence ratio (R_c) of the enhancement of the electron temperature at ~110 km under the fast upflows to reveal effect of the electric field on the ion upflows more precisely.

R_c is defined as the probability of the enhancement of the electron temperature at ~110 km ($T_{e_{110km}}$ > 400 K) when ions move upward with the velocity ($Vi > 50$ m/s). Note that, the data points are too limited to analyze the case of the upflows which are faster than 100 m/s and the author focused on the only fast upflows ($Vi > 50$ m/s).

Table 4.1: Summary table on the characteristic of ion upflows and mechanisms during CIR-/CME- driven magnetic storms on dawnside.

03-09 MLT	Parameter	TroUHF CIR small	TroUHF CIR large	TroUHF CME small	TroUHF CME large	ESR42m CIR small	ESR42m CIR large	ESR42m CME (large)*
Low-altitude Ion upflow	Vi (m/s)	×	15	19	46	22	×	×
	$Flux$ (m^{-2}/s)	×	1×10^{12}	2×10^{12}	4×10^{12}	2×10^{12}	×	×
High-altitude Ion upflow (cf., Ogawa et al., 2019)	Vi (m/s)	14	38	15	--	48	35	33
	$Flux$ (m^{-2}/s)	1×10^{12}	1×10^{12}	2×10^{12}	--	3×10^{12}	1×10^{12}	3×10^{12}
Ion temperature enhancement	ΔTi (K)	+110	+290	+280	+550	+250	+280	+64
	$\frac{Ti_{after}}{Ti_{before}}$	1.14	1.33	1.26	1.51	1.25	1.26	1.05
Electron temperature enhancement	ΔTe (K)	-160	-28	+180	+48	+360	+52	-230
	$\frac{Te_{after}}{Te_{before}}$	0.91	0.99	1.09	1.03	1.19	1.03	0.89
Electric field enhancement	$R_{Te_{110km}}$ (%,>400K)	1.6	5.5	5.7	25	27	21	37
Electric field enhancement	R_C (%)	15	50	4.3	74	44	60	51
Ratio of Vi >50 m/s	$R_{Vi_{50}}$ (%,>50m/s)	2.4	5.4	11	17	22	9.9	9.8
Ratio of Vi >100 m/s	$R_{Vi_{100}}$ (%,>100m/s)	0.12	0.57	2.1	4.8	2.6	0.66	1.3
Mechanism	**F**rictional / **P**recipitation	--	**F**?	**??**	**F**	**F** & **P**	--	--

***"(large)" means that available data were almost classified as large magnetic storms if the same criteria as Ogawa et al., [2019] is used, however, the author did NOT use any criteria in the case of results obtained by the ESR42m radar during CME-driven magnetic storms in this study.**

Table 4.2: Summary table on the characteristic of ion upflows and mechanisms during CIR-/CME- driven magnetic storms on dayside.

09-15 MLT	Parameter	TroUHF CIR small	TroUHF CIR large	TroUHF CME small	TroUHF CME large	ESR42m CIR small	ESR42m CIR large	ESR42m CME (large)*
Low-altitude Ion upflow	Vi (m/s)	×	--	×	×	×	×	×
	$Flux$ (m^{-2}/s)	×	--	×	×	×	×	×
High-altitude Ion upflow (cf., Ogawa et al., 2019)	Vi (m/s)	28	33	23	20	108	58	20
	$Flux$ (m^{-2}/s)	1×10^{12}	1×10^{12}	2×10^{12}	×	12×10^{12}	4×10^{12}	×
Ion temperature enhancement	ΔTi (K)	+43	--	+150	+430	+370	+200	+230
	$\frac{Ti_{after}}{Ti_{before}}$	1.05	--	1.14	1.40	1.40	1.20	1.18
Electron temperature enhancement	ΔTe (K)	-27	--	-140	-110	+490	+300	+28
	$\frac{Te_{after}}{Te_{before}}$	0.99	--	0.94	0.95	1.24	1.14	1.01
Electric field enhancement	$R_{Te_{110km}}$ (%,>400K)	2.4	20	17	19	38	19	41
Electric field enhancement	R_C (%)	20	100	60	100	61	48	53
Ratio of Vi >50 m/s	$R_{Vi_{50}}$ (%,>50m/s)	0.71	0.97	0.95	1.1	14	4.9	5.6
Ratio of Vi >100 m/s	$R_{Vi_{100}}$ (%,>100m/s)	0	0.19	0	0	2.2	0.17	1.0
Mechanism	**F**rictional / **P**recipitation	--	--	--	--	--	--	--

*“(large)” means that available data were almost classified as large magnetic storms if the same criteria as Ogawa et al., [2019] is used, however, the author did NOT use any criteria in the case of results obtained by the ESR42m radar during CME-driven magnetic storms in this study.

Table 4.3: Summary table on the characteristic of ion upflows and mechanisms during CIR-/CME- driven magnetic storms on duskside.

15-21 MLT	Parameter	TroUHF CIR small	TroUHF CIR large	TroUHF CME small	TroUHF CME large	ESR42m CIR small	ESR42m CIR large	ESR42m CME (large)*
Low-altitude Ion upflow	Vi (m/s)	×	×	×	11	×	×	×
	$Flux$ (m^{-2}/s)	×	×	×	2×10^{12}	×	×	×
High-altitude Ion upflow (cf., Ogawa et al., 2019)	Vi (m/s)	35	60	33	40	20	×	×
	$Flux$ (m^{-2}/s)	2×10^{12}	3×10^{12}	2×10^{12}	4×10^{12}	1×10^{12}	×	×
Ion temperature enhancement	ΔTi (K)	+220	+200	+140	+220	+130	+130	+90
	$\frac{Ti_{after}}{Ti_{before}}$	1.25	1.21	1.12	1.19	1.14	1.13	1.07
Electron temperature enhancement	ΔTe (K)	+290	+160	+110	+200	+190	+210	-180
	$\frac{Te_{after}}{Te_{before}}$	1.15	1.08	1.05	1.11	1.10	1.11	0.92
Electric field enhancement	$R_{Te_{110km}}$ (%,>400K)	13	20	13	12	17	6.0	25
Electric field enhancement	R_C (%)	21	19	17	43	33	20	0
Ratio of Vi >50 m/s	$R_{Vi_{50}}$ (%,>50m/s)	4.2	3.6	7.0	5.1	5.2	2.0	0.3
Ratio of Vi >100 m/s	$R_{Vi_{100}}$ (%,>100m/s)	1.1	0.28	0	0	0.66	0	0
Mechanism	**F**rictional / **P**recipitation	--	--	--	**F**	--	--	--

*“(large)” means that available data were almost classified as large magnetic storms if the same criteria as Ogawa et al., [2019] is used, however, the author did NOT use any criteria in the case of results obtained by the ESR42m radar during CME-driven magnetic storms in this study.

Table 4.4: Summary table on the characteristic of ion upflows and mechanisms during CIR-/CME- driven magnetic storms on nightside.

21-03 MLT	Parameter	TroUHF CIR small	TroUHF CIR large	TroUHF CME small	TroUHF CME large	ESR42m CIR small	ESR42m CIR large	ESR42m CME (large)*
Low-altitude Ion upflow	Vi (m/s)	37	33	51	58	(24)	(15)	31
	$Flux$ (m^{-2}/s)	3×10^{12}	3×10^{12}	10×10^{12}	7×10^{12}	(2×10^{12})	(1×10^{12})	9×10^{12}
High-altitude Ion upflow (cf., Ogawa et al., 2019)	Vi (m/s)	80	70	60	55	(25)	(10)	35
	$Flux$ (m^{-2}/s)	3×10^{12}	3×10^{12}	11×10^{12}	33×10^{12}	1×10^{12}	×	13×10^{12}
Ion temperature enhancement	ΔTi (K)	+150	+180	+260	+450	+160	+210	+150
	$\frac{Ti_{after}}{Ti_{before}}$	1.18	1.19	1.22	1.40	1.17	1.20	1.12
Electron temperature enhancement	ΔTe (K)	+620	+280	+360	+140	+210	+230	-65
	$\frac{Te_{after}}{Te_{before}}$	1.48	1.18	1.20	1.09	1.13	1.18	0.97
Electric field enhancement	$R_{Te_{110km}}$ (%,>400K)	3.2	8.7	8.0	26	22	20	29
Electric field enhancement	R_C (%)	17	30	15	50	40	39	30
Ratio of Vi >50 m/s	$R_{Vi_{50}}$ (%,>50m/s)	13	17	22	30	15	10	27
Ratio of Vi >100 m/s	$R_{Vi_{100}}$ (%,>100m/s)	2.5	3.5	4.9	7.3	1.4	0.7	4.3
Mechanism	**F**rictional / **P**recipitation	**P**	**F**? & **P**	**P**	**F**	--	--	**F**?

*“(large)” means that available data were almost classified as large magnetic storms if the same criteria as Ogawa et al., [2019] is used, however, the author did NOT use any criteria in the case of results obtained by the ESR42m radar during CME-driven magnetic storms in this study.

Section 4.3 Discussion

From those results mentioned above, the mechanisms can be identified. As shown in the Figure 4.1, the low-altitude ionospheric upflows can be classified as the classical Type1 or Type2 case based on the observational data from EISCAT as well as high-altitude ionospheric upflows. The ion frictional heating cause Type1 upflow and particle precipitation cause Type2 upflows in principle. Thus, the author can estimate mechanisms at each radar site during small and large CIR-/CME- driven magnetic storms. The author assessed contribution from the frictional heating with ion temperature increase by >15% ($\frac{Ti_{after}}{Ti_{before}} > 1.15$) and the ratio of enhancement on electron temperature at ~110km, which indicates the enhancement of the electric fields, were more than 10% during storm time ($R_{Te_{110km}} > 10\ \%$). On one hand, contribution of the particle precipitation is assessed with electron temperature increase by >15% ($\frac{Te_{after}}{Te_{before}} > 1.15$). If both conditions are satisfied, it is concluded that both frictional heating and precipitation contributed to the generation of the ion upflows. Note that, the author did not use the electron density because it can dramatically change depending on the seasonal and solar cycle variations. The results were summarized in the bottom lines from Table 4.1 to Table 4.4. **F** is corresponding to the Type1 upflows mainly caused by the frictional heating and **P** is corresponding to the Type2 upflows mainly caused by the precipitation.

R_c is useful to confirm the effect of electric fields on the ion upflows driven by the frictional heating more precisely. In fact, the ion upflows faster than 50 m/s were observed with the enhanced electron temperature at 110 km (> 400 K) at Tromsø during CME-driven large magnetic storms, in which the frictional heating mainly contribute to the upflows: R_c is 74% in dawnside, 43% in duskside, and 50 % in nightside (See Table 4.1, Table 4.3, and Table 4.4). On the other hand, ion upflows caused by the precipitation had small R_c at Tromsø in nightside: 17% during CIR-driven small storms and 15 % during CME-driven storms.

Three cases described as the mechanisms of the frictional heating with a single question mark (**F**?) cannot be determined by using the above criteria. One is for the case of the analysis with the EISCAT UHF radar at Tromsø during CIR-driven large magnetic storms in dawnside (See Table 4.1). In this case, the ion temperature was strongly

enhanced but the index of the electric fields' enhancement is not so high ($R_{Te_{110km}}$~5.5). However, the index of the electric fields' enhancement increased in Figure 4.6b and R_c was 50% after storm onset. In addition to that, the electron temperature did not change in Figure 4.2d2 and even decrease under the effect of the magnetic storms on Table 4.1. Thus, it is concluded that the moderately enhanced electric fields probably generate ion upward transportation throughout the frictional heating during CIR-driven large magnetic storms. Another is the case of the analysis with the EISCAT UHF radar at Tromsø during CIR-driven large magnetic storms in nightside (See Table 4.4). In this case, the electron temperature was enhanced, so that the precipitation contributed to the ion upflows. In addition to that, the ion temperature was also enough enhanced but the index of the electric fields' enhancement is little smaller than the criteria ($R_{Te_{110km}}$~ 8.7). However, the index of the electric fields' enhancement increased in Figure 4.6b and R_c was 30% after storm onset. Thus, it is concluded that the moderately enhanced electric fields probably generate ion upward transportation during CME-driven small magnetic storms. The other is the case of the analysis with the EISCAT ESR radar at Svalbard during CME-driven magnetic storms in nightside (See Table 4.4). In this case, the index of the electric fields' enhancement is enough high but the ratio of the ion temperature enhancement is less than 15% ($\frac{Ti_{after}}{Ti_{before}}$~1.12). However, it is so close to the value of the criteria that ion temperature might be enough enhanced and R_c is 30%. In addition to that, the electron temperature did not change in Figure 4.5d and even decrease under the effect of the magnetic storms on Table 4.4. Thus, it is concluded that the frictional heating caused by moderately enhanced electric fields mainly contributed to the upflows. These conclusions are consistent with results on the differences of strength of the effective electric fields from Figure 4.6 and Figure 4.7.

In the case of the EISCAT UHF radar at Tromsø during CME-driven small magnetic storms in dawnside, the mechanism is described as unclear with double question marks (??). In this case, the ion temperature was strongly enhanced. The electron temperature was also slightly enhanced but smaller than the criteria. These results suggest that the relative contribution of each mechanism is not clear, but the frictional heating may contribute to some of the ion upflows. On the other hand, the index of the electric fields' enhancement is not so large ($R_{Te_{110km}}$~5.7) and there was no distinctive enhancement after storm onset (See Figure 4.6c). In addition to that, R_c was 4.3% and the ratio was

too small to support that the frictional heating mainly caused the upflows. Thus, it is difficult to conclude the mechanism with an absolute certainty but it is suggested that the frictional heating might contribute to the ion upflows because of the strong ion temperature enhancement and weak electron temperature enhancement.

Further discussions are needed for the case of the results with the EISCAT ESR radar at Svalbard in nightside shown in Figure 4.4 and Figure 4.5, and on Table 4.4. It is true that the analysis results about ion velocity and flux in the low-altitude ionosphere indicate upward ion transportations, but the characteristic continued in all days, that is, did not depend on the effect of the magnetic storms. This apparent upward ion transportation might be caused by the neutral wind [Yamazaki et al., 2017]. The convection of the neutral wind created strong drag force and ions moved into the same direction in the low-altitude ionosphere. The transportation was projected onto the field-aligned direction and then the EISCAT ESR radar at Svalbard observed apparent ion upward flows. However, ion upflows were not actually generated by the geomagnetic disturbance. This characteristic is unique for positions of the radar sites so that it cannot be observed at Tromsø.

In summary described from Table 4.1 to Table 4.4 , it is concluded that the frictional heating mainly caused upflows during CME-driven magnetic storms at both locations and possibly in dawnside during CIR-driven storms at Svalbard, whereas the particle precipitation mainly caused upflows during CIR-driven magnetic storms at both locations and possibly in nightside during small CME-driven storms at Tromsø.

Moreover, the author estimated the enhancement of the ratio of fast upflows in the low-altitude ionosphere. $R_{Vi_{50}}$ ($R_{Vi_{100}}$) means the ratio of averaged ion velocity between 250 and 350 km, which is faster than 50 (100) m/s. Faster upflows can transport molecular ions into high-altitude. Thus, this ratio indicates the supply ability of molecular ions. The estimation of the remaining flux in Section 4.2.3 resulted in that 50 m/s upward velocity could not provide enough molecular ions as the source for high-altitude upflow. Thus, the value of $R_{Vi_{100}}$ is important for the supply process of the molecular ions. In particular, $R_{Vi_{100}}$ reached several % after storm onset in several cases. In dawnside, the frictional heating mainly contributed to the very fast upflows (> 100 m/s). It is revealed that the very fast ion upflows were observed during CME-driven storms more frequently than CIR-driven storms. In nightside, the same tendency was confirmed for the upflows driven by the precipitation and frictional heating. This result indicates that CME-driven storms can create the faster upflows than CIR-driven storms and much molecular ions can be

transported. Molecular ions were often observed with large storms [c.f., Seki et al., 2019] and CME-driven storms typically have smaller minimum Dst index than CIR-driven storms [c.f., Borovsky and Denton, 2006]. This result is consistent with the previous studies. On the other hand, the $R_{Vi_{100}}$ in duskside is smaller than in dawnside and nightside. It indicates that duskside upflows less contributed to the supply of molecular ions into high-altitude than dawnside and nightside, even though the ion upflow exist in the low-altitude ionosphere. Note that, the result just suggests that there are a few fast upflows to supply molecular ions but most of them could not provide enough molecular ions based on the simple estimations of minimum value of remaining flux in Section 4.2.3.

It is important to consider relative positions of the radar sites to the auroral oval. The EISCAT UHF radar at Tromsø measured the geomagnetic latitude of 66.2 °N, which is a typical region located within nightside auroral oval and subauroral region in the dayside. The auroral oval expands to the equatorward and even poleward during magnetic storms. Thus, the EISCAT ESR radar at Svalbard, which locates 75.2° geomagnetic latitude, has a high chance to measure the polar cap region after storm onset and edge of the auroral oval in nightside.

By using Weimer model, Ogawa et al. [2019] revealed that joule heating rate increased with development of the field-aligned currents and convection electric fields around the huge area from duskside to dawnside (0-9, 15-24 MLT) during CIR- and CME-driven magnetic storms at Tromsø and in all MLT sectors during CME-driven storms at Svalbard (See Figures 7 and 8 of Ogawa et al., 2019). They also suggested that the area was under expanding auroral oval. In fact, the ion velocity was not so fast in the high-altitude ionosphere during CME-driven magnetic storms, but the flux in the high-altitude ionosphere during CME-driven storms was stronger than during CIR-driven storms due to the enhancement of the electron density caused by the soft particle precipitations (< ~500 eV) especially in nightside. Also, larger CME-driven storms had a stronger flux in the high-altitude ionosphere, which is larger flux compared with CIR-driven storm cases.

In this study, the frictional heating contributed to the ion upflows during large CME-driven magnetic storms and CIR-driven large magnetic storms from duskside to dawnside at Tromsø, and during CME-driven storms in nightside at Svalbard, and also contributed during CIR-driven large magnetic storms shown in Table 4.1 to Table 4.4. These results are consistent with the enhancement of joule heating rate reported by the previous study on high-altitude ionosphere [Ogawa et al., 2019]. As introduced Section 1.1.3, Pedersen

conductivity is effective in the low-altitude ionosphere. Once the ion temperature is enhanced in the low-altitude region, the temperature is enhanced in the wide range and pressure gradient is also enhanced in the high-altitude ionosphere. Thus, it is considered that the frictional heating occurred in the low-altitude ionosphere and connected high-altitude ionosphere. However, the ion flux enhancements in the CME-driven magnetic storms in nightside, which is remarkable in the high-altitude case, were not detected in the low-altitude ionosphere. The actual value of the averaged ion flux in the low-altitude ionospheric upflows caused by the frictional heating was less than in the high-altitude cases during CME-driven storms, although it was almost the same between high and low altitude cases in the upflows caused by the precipitation during CIR-driven magnetic storms. According to the previous study [Caton et al., 1996], the energy order of magnitude for electrons to generate the ion upflows by the precipitation seems to need ~1 keV at least in the low-altitude ionosphere. Thus, it is suggested that Joule heating (the frictional heating) with development of the field-aligned currents is important to generate ion upflows and the energy of precipitating particles is not enough high to affect the ion upflows in the low-altitude ionosphere around auroral oval from duskside to dawnside. On the other hand, the contribution of the precipitation is remarkable in nightside during CIR-driven magnetic storms and small CME-driven storms in nightside on Table 4.4. It is considered that these upflows were mainly caused by the high-energy (> ~1 keV) electron precipitation from the plasma sheet / ring current [Hardy et al., 1987; Kataoka and Miyoshi, 2006]. For large CME-driven cases, the magnetic field line observed by the EISCAT UHF radar at Tromsø in the inner magnetosphere shifted outside such region along with the extremely equatorward expansion of the auroral oval.

When focusing on the case of the duskside, there are different features from those in nightside and dawnside during large CME-driven storms. The averaged ion upward velocity and flux were detected during only CME-driven large magnetic storms and the ion velocity and flux is smaller than those in nightside and dayside. The difference may result from the dawn-dusk asymmetry for ion upflows, which is mentioned in several previous studies in high-altitude ionosphere [e.g., Liu et al., 2000; Aikio and Selkälä, 2009; Ogawa et al., 2019]. It is consistent with those previous studies even in the low-altitude ionosphere that the upward ion flux in the dawnside was larger than in the duskside. In particular, Aikio and Selkälä [2009] reported that the joule heating rate in dawnside is higher than in duskside during solar active periods. There is a possibility that

the development of the electric fields could not provide enough energy to generate ion upflows in the low-altitude ionosphere in duskside during small storms. In addition to that, there are several studies on the relationship between ion upflows and Subauroral Polarization Stream (SAPS). SAPS is the westward flow resulting from the $E \times B$ drift caused by enhanced electric fields. Zhan et al. [2020] reported that ion upflows can occur with SAPS because of the frictional heating caused by the velocity difference between neutrals and ions. The EISCAT UHF radar at Tromsø has a chance to observe the subauroral region in duskside, where SAPS often develop along with the magnetic disturbance. There is a possibility that these ion upflows with smaller flux result from the localized electric fields' enhancement by SAPS in duskside.

There were upward velocity and flux in dayside in high-altitude ionosphere as shown in Ogawa et al. [2019] especially at Svalbard. However, any ion upflows were not detected in the low-altitude ionosphere in dayside (see Table 4.2). There are three reasons why there is such a difference between low and high altitude cases. One is that the ion upflows in dayside were caused by soft particle precipitations. Ogawa et al., [2019] suggested that the EISCAT ESR radar at Svalbard located auroral oval and the soft particle precipitations caused ion upflows in the high-altitude ionosphere. However, the energy is not enough high to affect the low-altitude ionospheric ion upflows as mentioned above. Another reason is direction of the ion pressure gradient, which is important force to drive ion upflows throughout an acceleration process by the frictional heating. Yamazaki et al., [2017] reported that the averaged ion velocity at Tromsø and Svalbard directs downward below ~350-450km in dayside under the high solar activity. The direction is determined by the peak altitude of the electron density, which results in the direction of the ion pressure gradient. In fact, the author can confirm the clear enhancement of the downward ion flow with the enhancement of the ion temperature and electric fields as characteristics on the frictional heating in Figure 4.4a-d and Table 4.2. The other possibility is that upflow region moves with the dayside auroral oval expansion. The scenario has been proposed in the higher altitude case [Ogawa et al., 2019]. They suggested that auroral oval extremely expands to equatorward and the ion upflow region move equatorward, and then upflowing / downflowing ions convect poleward with globally developed electric field during larger CME storms. Thus, the downward ion motion was observed at Svalbard. These stories are not contradictory one another.

In terms of the duration of ion upflows, the differences between CIR- and CME-

driven storms are remarkable. To minimize the influence of Dst index the case of CIR-large storms must be compared with the case of CME-small storms at Tromsø, as mentioned in Ogawa et al. [2019]. The ion upflows continue over 3 days after the storm onset during CIR-storms, whereas the upward velocity was suddenly enhanced and rapidly decrease within 1 day during CME-driven storms (See Figure 4.2 and Figure 4.3). The upward velocity and flux on the first day of the storm was strongly enhanced during CME-driven storms. These upflows were triggered by the precipitations in the nightside (See Table 4.4). Thus, it is considered that the strong and concentrated precipitations occurred during CME-driven storms. In fact, it is reported that the bursty strong auroral emission was more pronounced during CME-driven storms than CIR-driven storms [Borovsky and Denton, 2006]. These phenomenological aspects can be understood by difference in characteristics of solar wind drivers, i.e., CIR and CME. As summarized in Kataoka and Miyoshi [2006], the CIR-storms are characterized by successive substorm activities during recovery phase of the storm due to the Alfven wave chain in the solar wind after the CIR passage, while recovery phase of the CME-storms is characterized by relatively rapid recovery and less substorm activities. On the other hand, the frictional heating mainly caused ion upflows both during CIR-large and CME-large storms. It indicates that the frictional heating is well related to the Dst index. The large storms can develop strong magnetospheric convection which results in strong enhancement of the ring current, enhanced electric fields in the ionosphere, and auroral oval expansion.

For CIR-driven magnetic storms at Svalbard on Table 4.1, it is difficult to estimate the reason why only small storms cause the ion upflows on average. The EISCAT ESR radar at Svalbard possibly located auroral oval in dawnside, but the same situation could occur in duskside and the issue on effective energy limitation will remain. In addition to that, the frictional heating seems to be more effective during CIR-larger storms in Figure 4.6 and Table 4.1. One possibility is some localized effect but further investigation will be needed.

Section 4.4 Summary

The author investigated the effects of the CIR-/CME-driven magnetic storms on the ion upflows in the low-altitude ionosphere (250-350 km) with EISCAT data from 1996-2015. The results show that ion upflows in the low-altitude ionosphere were observed mainly in dawnside and nightside at Tromsø and Svalbard during both CIR- and CME-driven magnetic storms, and also observed in duskside by the Tromsø UHF radar during only CME-driven large magnetic storms. The ion upflows were not detected in dayside at Svalbard in the low-altitude ionosphere although they were remarkable in the high-altitude (400-500 km) ionosphere. Also, the author analyzed mechanisms of the ion upflows focusing on the Type1 and Type2 upflows. The results can be summarized as follows:

- The frictional heating mainly caused upflows during CME-driven magnetic storms at both locations and possibly in dawnside during CIR-driven storms at Svalbard.
- The particle precipitation mainly caused upflows during CIR-driven magnetic storms at both locations and possibly in nightside during small CME-driven storms at Tromsø.

Figure 4.8 shows the schematic drawing of characteristics on the ion upflows which were mentioned above. Each mechanism in every 6 MLT sector is summarized for each storm size and type. From this result, the following scenario is plausible: (1) During CIR-storms, the precipitations caused by successive auroral substorms leads to the moderate but continuous ion upflows. (2) During CME-driven storms, the enhancement of auroral activities concentrated during the storm main phases leads to the concentrated and busty precipitations and causes the strong upflows just after the storm onset. (3) Strong enhancement of the magnetospheric convections during the large magnetic storms and resultant current system development in the magnetosphere-ionosphere coupled system globally develop the convection electric field in the ionosphere, and cause the upflows by the frictional heating. In particular, large CME-storms dramatically disturb the geomagnetic field, thus, the frictional heating frequently causes the upflows in wide area around auroral oval. However, it is not revealed why CIR-small storms cause the ion

upflows caused by the frictional heating at Svalbard. One possibility is some localized effects such as localized electric field enhancement. For further investigation, simultaneous observations with SuperDARN radar networks might be useful.

Those conclusions play an important role to understand comprehensive properties of the transportation mechanisms of molecular ions into the high-altitude ionosphere and even into the magnetosphere during magnetic storms.

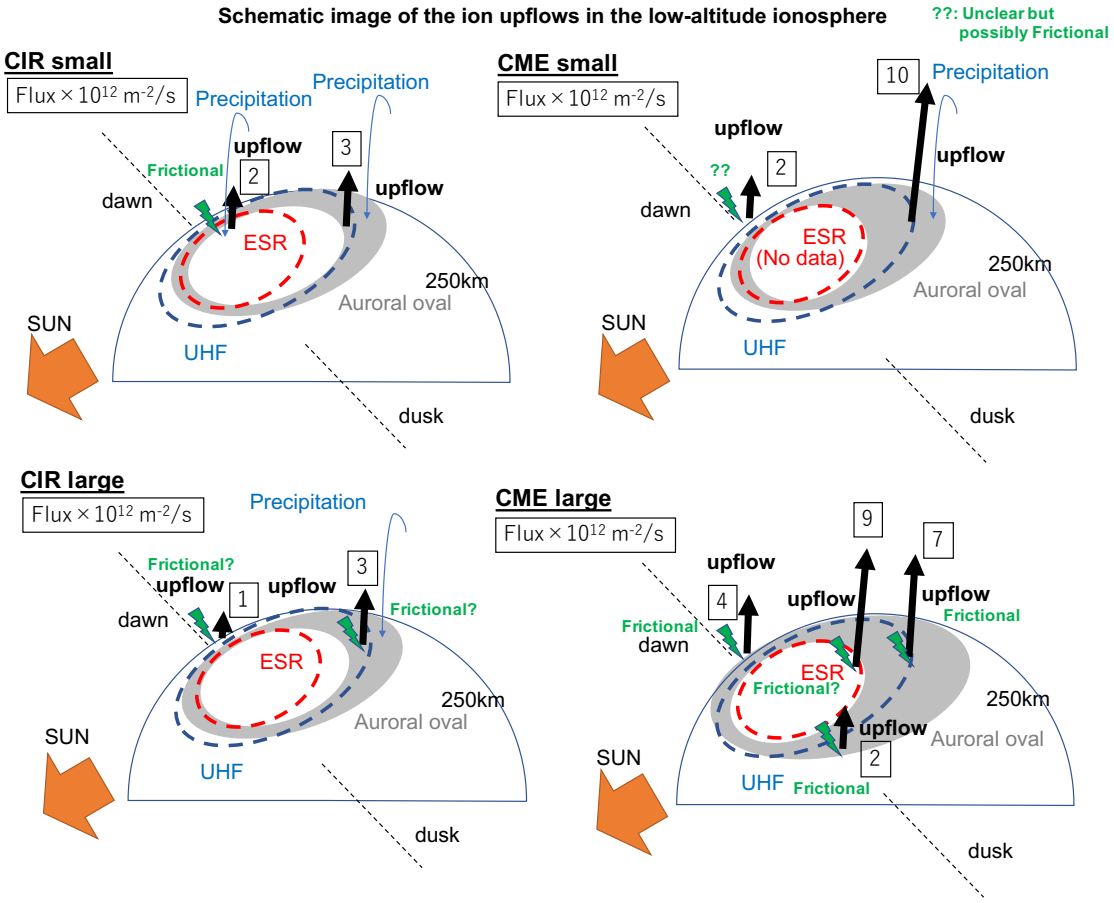

Figure 4.8: Schematic drawing of the ion upflows in the low-altitude ionosphere (250-350 km) during CIR- and CME-driven magnetic storms based on Table 4.1 to Table 4.4 and discussions in Section 4.3. The results from 03-09 MLT corresponds to the dawnside, 09-15 MLT corresponds to the dayside (Sunward), 15-21 MLT corresponds to the duskside, 21-03 MLT corresponds to the nightside. CIR = Corotating Interaction Region; CME = Coronal Mass Ejection; MLT = Magnetic Local Time. Note that, the value and mechanism in the case of ESR and CME large storms refer to the results during all magnetic storms because any classifications using Dst index were not considered due to the lack of data points during small storms.

Chapter 5 General discussion

The author firstly aimed at investigating which mechanisms can cause the ion upflows in the low-altitude ionosphere, where molecular ions exist. As introduced in Section 1.3.2, there are several mechanisms such as the ion frictional heating and particle precipitation, which can drive the ion upflows. However, Peterson et al., [1994] reported that the candidate mechanisms could not give enough energy to generate rapid upward flows overcoming the loss due to the dissociative recombination (Question (1) in Section 1.4). In the event study, EISCAT radar observed the ion upflow during magnetic storm started on September 7, 2017, while the Arase satellite observed the molecular ions in the ring current. The analysis results suggested that ion and electron pressure gradients enhanced by the ion frictional heating with the strong convective electric field contributed to the rapid ion upflows, which could transport ions upward overcoming dissociative recombinations as discussed in Section 3.3.

EISCAT observed not only Type1 upflows, which is caused by the frictional heating, but also Type2 upflows caused by the particle precipitation in the low-altitude ionosphere. An example of observed Type1 and Type2 upflows in the low-altitude ionosphere was shown in Section 4.2.1. The properties of Type1 and Type2 upflows during magnetic storms are important. Ogawa et al. [2019] investigated the dependences of ion velocity and flux on CIR- and CME-driven magnetic storms in the high-altitude ionosphere as introduced in Section 1.3.1. However, there were no study to reveal such dependences in the low-altitude ionosphere and it was unknown how the properties of ion upflows and their generation mechanisms change depending on the size and type of magnetic storms (Question (2) in Section 1.4). In the statistical study, the dependence of ion upflows in the low-altitude ionosphere on the CIR-/CME-driven magnetic storms was investigated. The results were summarized on the tables in Section 4.2.3. The detailed comparisons between low- and high-altitude cases at each MLT have been already described in Section 4.3. Here, the summary results on the ion flux in the low-altitude ionosphere shown in Figure 4.8 are mainly compared with those in the high-altitude case (See Table 1.2 and Figure 1.15) in order to achieve the comprehensive understanding of supply mechanisms of heavy ions in the ionosphere.

During CIR-driven magnetic storms, heavy ions are mainly transported upward in

nightside around auroral oval. The upflows can be caused by the particle precipitation from the low-altitude and smoothly connect the upflows in the high-altitude ionosphere because the flux is almost constant ($\sim 3\times10^{12}$ m^{-2}/s). In dawnside, there are also upward flows from the low-altitude ionosphere but not too much flux can be transported ($\sim 1\times10^{12}$ m^{-2}/s). The frictional heating, which is driven by the enhancement of the convection electric fields, contribute to upflows in dawnside as well as the particle precipitation.

During small CME-driven magnetic storms, almost the same characteristics as observed during CIR-driven storms around auroral oval in the low-altitude ionosphere. However, the escape flux is larger than during CIR-driven cases ($\sim 10\times10^{12}$ m^{-2}/s) and the steep peak on the ion upward velocity and flux can be detected after storm onset (Compared Figure 4.3 to Figure 4.2). It means that the energy from the precipitations is high and concentrating during CME-driven storms. This characteristic is also detected in the high-altitude ionosphere [Ogawa et al., 2019]. Thus, strong precipitations can affect the ionospheric atmosphere and generate upflows and the almost same ion flux are transported from the low-altitude to high altitude ionosphere in nightside during CME-driven storms. At the same time, upflows by frictional heating occur in dawnside.

During CME-large storms, the strongly developed field-aligned currents and convection electric fields contribute to the ion upflows in the huge area from dusk to dawn sectors. Region 1 field aligned current contribute to the upflows both Svalbard and Tromsø latitude and Region 2 field aligned current mainly contribute to the mid-latitude region, that is, partially at Tromsø. In particular, Region 2 field aligned current is involved in the SAPS in duskside. These dramatically developed current systems cause the ion disturbance and upflows in the polar ionosphere. However, the supplied ion flux become smaller than during small storms at Tromsø and it is possibly considered that the auroral oval extremely expanded and soft particle precipitations cannot affect the low-altitude ionosphere [Caton et al., 1996], whereas it more efficiently affects the high-altitude ionosphere as discussed in Section 4.3. In addition to that, there are small ion upward flux ($\sim 2\times10^{12}$ m^{-2}/s) from the low-altitude ionosphere in duskside. Only large storms can cause upflows in the low-altitude ionosphere in duskside, whereas small upward flux could be detected in the both low- and high-altitude ionosphere during smaller storms due to the difference on joule heating rate between dawnside and duskside [Aikio and Selkälä, 2009]. Zhan et al., [2020] reported that the upflows with SAPS are detected during high

solar activities at the Tromsø latitude. The result in this study suggest the similar relationship between upflows and geomagnetic activity even in the low-altitude case.

In dayside, the ion upflows in the high-altitude ionosphere are significantly detected but no upflows in the low-altitude case during both CIR- and CME-driven storms. It is considered that the peak altitude for the electron density and effects of neutral wind result in the difference [Yamazaki et al., 2017] or the soft precipitations did not provide enough energy to the low-altitude ionosphere [Caton et al., 1996]. Thus, molecular ions are hardly supplied into the magnetosphere via the dayside outflow, although O^+ can escape so much.

Chapter 6 General conclusion

In this study, the author investigated the ion upflows in the low-altitude ionosphere and their effects on the supply of terrestrial heavy ions to the magnetosphere based on the Arase satellite and EISCAT radar observations. As described in Section 1.4, there are two outstanding questions aimed to solve in this study: What is the mechanisms to achieve rapid upward transport of ions in the low-altitude (< 300 km) ionosphere overwhelming the rapid decrease of molecular ions by the dissociative recombination (Question 1), and How the generation mechanism and properties of the low-altitude ion upflows, which can include molecular ions, change with the size and types of the magnetic storms (Question 2). The results are summarized as below:

- The event study during September 7, 2017 magnetic storm shows that the frictional heating can cause the fast ion upflow in the low-altitude ionosphere. Continuous observations of the molecular ions by the Arase satellite suggest that the fast upflow facilitate the rapid transport of molecular ions to the magnetosphere overcoming the loss effect due to the dissociative recombination. (Question 1 related).
- In the nightside, the statistical analysis reveals that the particle precipitation from the magnetosphere to the ionosphere mainly cause the low-altitude ion upflows during CIR-driven magnetic storms and small CME-driven storms around the auroral oval (Question 2 related).
- From the duskside to dawnside, the frictional heating causes low-altitude ion upflows along with the enhancement of the convection electric field in a wide area of the polar ionosphere during large CME-driven magnetic storms (Question 2 related).
- In the dawnside, the frictional heating caused by the convection electric field contributes to the low-altitude ion upflows even during the small storms. In the duskside, only large CME-driven storms can supply ions from the low-altitude ionosphere around the subauroral region, which can be related to the SAPS (Question 2 related).

- In the dayside, no ion upflows from the low-altitude ionosphere are observed, although the soft particle precipitation around the cusp region causes strong ion upflows in the high-altitude ionosphere (Question 2 related).

Table 6.1 summarizes these main results of this thesis. Since the molecular ions usually exist only in the low-altitude ionosphere, the results give the answer to explain the supply mechanisms of unexpected frequent observations of the molecular ions in the inner magnetosphere during magnetic storms [Seki et al., 2019]: The results reveal that the particle precipitation around the nightside auroral oval frequently contributes to the supply of ions from the low-altitude ionosphere to the magnetosphere during magnetic storms regardless of the size and types of the storms. It is also indicated that the frictional heating causes additional supply of ions from the low-altitude ionosphere in the wide local time range from dusk to dawn during the large CME-driven magnetic storms and in the dawnside for all size of the storms. This conclusion suggests that the magnetic storms are the effective driver of the ion escape from the collisional low-altitude ionosphere to space for the magnetized terrestrial planets.

The author obtained the general properties of molecular ion escape from the deep ionosphere through the detailed analysis. EISCAT cannot observe the ionosphere every time during geomagnetic disturbance periods. However, we can now estimate the ionospheric escape process and mechanisms from the types and size of magnetic storms based on those results and steady observation of the solar wind. Moreover, we can apply these results to another magnetized terrestrial planet, where it is difficult to observe ionosphere directly with ground observation, if we know the environmental information about atmospheric compositions and how the planet is magnetized.

Table 6.1: Summary tables on the ion upflow flux and candidate heating mechanisms.

Ion Upflow Flux in the low-altitude ionosphere on the First Day of Magnetic Storm				
66.2° mlat. (Tromsø)	CIR		CME	
	Small storm	Large storm	Small storm	Large storm
Dawnside (03-09 MLT)	×	0.1 / **F**?	0.2 / ??	0.4 / **F**
Dayside (09-15 MLT)	×	--	×	×
Duskside (15-21 MLT)	×	×	×	0.2 / **F**
Nightside (21-03 MLT)	0.3 / **P**	0.3 / **F**?&**P**	1.0 / **P**	0.7 / **F**
75.2° mlat. (Svalbard)	CIR		CME	
	Small storm	Large storm	All (Large) storms	
Dawnside	0.2 / **F**&**P**	×	×	
Dayside	×	×	×	
Duskside	×	×	×	
Nightside	(0.2)	(0.1)	0.9 / **F**?	
Note. The unit of the ion flux is ($\times 10^{13}$ m^{-2}/s). **F**: Frictional heating, **P**: Particle precipitation, **F**?: Frictional heating (probably), ??: Unclear but possibly Frictional heating				

Acknowledgements

This thesis was written with much corporation; in particular, thanks to Prof. Kanako Seki, Prof. Yasunobu Ogawa, Prof. Shoichiro Yokota, Prof. Satoshi Kasahara, Assoc. Prof. Kunihiro Keika, Prof. Masahiro Hoshino, Assoc. Prof. Takanobu Amano.

Prof. Kanako Seki is my supervisor in University of Tokyo. She gave me a lot of support about not only study but also my life work. The author is very grateful for her advice. Thank you very much, Prof. Kanako Seki.

Prof. Yasunobu Ogawa is a member of the National Institute of the Polar Research (NiPR). He taught me the fundamental knowledge on Incoherent Scatter radar. In particular, a course in the University of Tokyo in 2018 and experiences at the EISCAT Tromsø radar site and University of Tromsø in 2019 remarkably helps my works including this thesis. He also helped the analysis using the EISCAT PSD data in NiPR. This thesis would not be completed without his corporation. Furthermore, the author would like to acknowledge the all members of EISCAT radar (GUISDAP developer) team.

Prof. Shoichiro Yokota, Prof. Satoshi Kasahara and Assoc. Prof. Kunihiro Keika are main members participating in the MEP-i instrument development. In this study, the TOF data obtained Arase satellite is necessary to discuss the molecular ions. The author would like to be indebted to these members and also acknowledge ERG science team too.

Prof. Masahiro Hoshino and Assoc. Prof. Takanobu Amano discussed this observational study in terms of the theoretical method. The author is grad to their precise suggestions.

Moreover, the author appreciates all members belong to the same course and laboratory in the University of Tokyo. Special thanks to my parents because of the continuous support for me in ten-years college life.

References

[1] Aikio, A. T., & Selkälä, A. (2009). Statistical properties of Joule heating rate, electric field and conductances at high latitudes. *Ann. Geophys.*, 27, 2661–2673. https://doi.org/10.5194/angeo-27-2661-2009

[2] Akbari. (2015). Beam plasma interactions and langmuir turbulence in the auroral ionosphere, https://doi.org/10.13140/RG.2.2.30381.28641

[3] André, M., & Yau, A. W. (1997). Theories and observations of ion energization and outflow in the high latitude magnetosphere, *Space Sci. Rev.*, 80, 27-48. https://doi.org/10.1023/A:1004921619885

[4] Bilitza, D., Altadill, D., Truhlik, V., Shubin, V., Galkin, I., Reinisch, B., & Huang, X. (2017). International Reference Ionosphere 2016: From ionospheric climate to real-time weather predictions, *Space Weather*, 15, 418–429. https://doi.org/10.1002/2016SW001593

[5] Blelly, P.-L., Alcaydé, D., & van Eyken, A. P. (2010). A new analysis method for determining polar ionosphere and upper atmosphere characteristics from ESR data: Illustration with IPY period, *J. Geophys.* Res., 115, A09322. https://doi.org/10.1029/2009JA014876

[6] Borovsky, J. E., & Denton., M. H. (2006), Differences between CME-driven storms and CIR-driven storms, *J. Geophys. Res.*, 111, A07S08, https://doi.org/10.1029/2005JA011447

[7] Brekke, A. (2013). Physics of the Upper Polar Atmosphere, *Springer Berlin, Heidelberg,* https://doi.org/10.1007/978-3-642-27401-5

[8] Burch, J. L., Torbert, R. B., Phan, T. D., Chen, L.-J., Moore, T. E., Ergun, R. E., Eastwood, J. P., et al. (2016), Electron-scale measurements of magnetic reconnection in space, *Science,* https://doi.org/10.1126/science.aaf2939

[9] Burchill, J. K., Knudsen, D. J., Clemmons, J. H., Oksavik, K., Pfaff, R. F., Steigies, C. T., et al. (2010). Thermal ion upflow in the cusp ionosphere and its dependence on soft electron energy flux, *J. Geophys. Res. Space Physics*, *115(A5)*. https://doi.org/10.1029/2009JA015006

[10] Carlson, C. W., McFadden, J. P., Ergun, R. E., Temerin, M., Peria, W., Mozer, F. S. et al. (1998). FAST observations in the downward auroral current region:

Energetic upgoing electron beams, parallel potential drops, and ion heating, *Geophys. Res. Lett.*, *25(12)*, 2017-2020. https://doi.org/10.1029/98GL00851

[11] Nathan, Case. (2014). Solar Wind-Magnetosphere Interactions: A Statistical Analysis of Spacecraft Measurements. https://doi.org/10.13140/2.1.2588.8321

[12] Caton, R., Horwitz, J. L., Richards, P. G., & Liu, C. (1996). Modeling of F-region ionosphere upflows observed by EISCAT. *Geophys. Res. Lett*, 23, 1537. https://doi.org/10.1029/96GL01255

[13] Christon, S. P., Gloeckler, G., Williams, D. J., Mukai, T., McEntire, R. W., Jacquey, C., et al. (1994). Energetic atomic and molecular ions of ionospheric origin observed in distant magnetotail flow-reversal events, *Geophys. Res. Lett.*, 21, 3023-3026. https://doi.org/10.1029/94GL02095

[14] Clausen, L. B. N., Baker, J. B. H., Ruohoniemi, J. M., Greenwald, R. A., Thomas, E. G., Shepherd, S. G., et al. (2012). Large-scale observations of a subauroral polarization stream by midlatitude SuperDARN radars: Instantaneous longitudinal velocity variations, *J. Geophys. Res.*, *117*, A05306. doi:10.1029/2011JA017232

[15] Daglis, I. A., Thorne, R. M., Baumjohann, W., & Orsini, S. (1999). The terrestrial ring current: Origin, formation, and decay, *Rev. Geophys.*, 37(4), 407–438. https://doi.org/10.1029/1999RG900009

[16] Davies, J. A., & Robinson, T., R. (1997). Heating of the high-latitude ionospheric plasma by electric fields, *Adv. Space Res., 20(6)*, 1125-l 128. https://doi.org/10.1016/S0273-1177(97)00755-2

[17] Deng, Y., Heelis, R., Lyons, L. R., Nishimura, Y., & Gabrielse, C. (2019). Impact of flow bursts in the auroral zone on the ionosphere and thermosphere. *J. Geophys. Res. Space Physics*, *124*, 10459– 10467. https://doi.org/10.1029/2019JA026755

[18] Ebihara, Y. and Y. Miyoshi, (2011). Dynamic inner magnetosphere: Tutorial and recent advances, in Dynamic Magnetosphere, *IAGA Special Sopron Book Series*, 3, 145-187. https://doi.org/10.1007/978-94-007-0501-2

[19] Foster, J. C., & Vo, H. B. (2002). Average characteristics and activity dependence of the subauroral polarization stream, *J. Geophys. Res. Space Physics*, *107(A12)*, SIA 16-1-SIA 16-10. https://doi.org/10.1029/2002JA009409

[20] Ganushkina, N. Y., Liemohn, M. W., Dubyagin, S., Daglis, I. A., Dandouras, I., De Zeeuw, D. L., et al. (2015). Defining and resolving current systems in

geospace, *Ann. Geophys.*, 33, 1369–1402, https://doi.org/10.5194/angeo-33-1369-2015

[21] Ghuratia, R., Pandey, A., & Dhurve, A. (2022). Current system perspective of earth magnetosphere. *Int. J. Innovat. Res. Growth*, 11, 74-82. https://doi.org/10.26671/IJIRG.2022.3.11.105

[22] Hardy, D. A., Gussenhoven, M. S., Raistrick, R., & McNeil, W. J. (1987). Statistical and functional representation of the pattern of auroral energy flux, number flux, and conductivity. *J. Geophys. Res.*, 92, 12275–12294. https://doi.org/10.1029/JA092iA11p12275

[23] Hedin, A. E. (1991), Extension of the MSIS Thermospheric Model into the Middle and Lower Atmosphere, *J. Geophys. Res. 96(A2)*, 1159-1172. https://doi.org/10.1029/90JA02125

[24] Hui, Y., T. E. Cravens, N. Ozak, and D. R. Schultz. (2010). What can be learned from the absence of auroral X-ray emission from Saturn?, *J. Geophys. Res.*, 115, A10239. https://doi.org/10.1029/2010JA015639

[25] Ichimaru, S., (2004). Statistical Plasma Physics, Volume I: Basic Principles (Frontiers in Physics). *Westview Press*.

[26] Ieda, A., Kauristie, K., Nishimura, Y., Miyashita, Y., Frey, H. U., Juusola, L., et al. (2018). Simultaneous observation of auroral substorm onset in Polar satellite global images and ground-based all-sky images. *Earth Planets Space*, 70, 73, https://doi.org/10.1186/s40623-018-0843-3

[27] Ji, E.-Y., Jee, G., & Lee, C. (2019). Characteristics of the occurrence of ion upflow in association with ion/electron heating in the polar ionosphere, *J. Geophys. Res. Space Physics*, 124(7), 6226–6236. https://doi.org/10.1029/2019JA026799

[28] Kataoka, R., & Miyoshi, Y. (2006), Flux enhancement of radiation belt electrons during geomagnetic storms driven by coronal mass ejections and corotating interaction regions, *Space Weather*, *4*, S09004, https://doi.org/10.1029/2005SW000211.

[29] Kataoka, R., Nishitani, N., Ebihara, Y., Hosokawa, K., Ogawa, T., Kikuchi, T., & Miyoshi, Y. (2007). Dynamic variations of a convection flow reversal in the subauroral postmidnight sector as seen by the SuperDARN Hokkaido HF radar, *Geophys. Res. Lett.*, *34(21)*, L21105. https://doi.org/10.1029/2007GL031552

[30] Keika, K., Kistler, L. M., & Brandt, P. C. (2013). Energization of O+ ions in the Earth's inner magnetosphere and the effects on ring current buildup: A review of previous observations and possible mechanisms, *J. Geophys. Res. Space Physics*, 118(7), 4441–4464. https://doi.org/10.1002/jgra.50371

[31] Kelley, M. C. (2009). The Earth's Ionosphere: Plasma Physics and Electrodynamics (2nd ed.). *London: Elsevier. Academic Press.*

[32] Kistler, L. M., Mouikis, C. G., Asamura, K., Yokota, S., Kasahara, S., Miyoshi, Y., et al. (2019). Cusp and Nightside Auroral Sources of O+ in the Plasma Sheet, *J. Geophys. Res.*, *124(12)*, 10036-10047. https://doi.org/10.1029/2019JA027061

[33] Klecker, B., Möbius, E., Hovestadt, D., Scholer, M., Gloeckler, G., Ipavich, F. M. (1986). Discovery of energetic molecular ions (NO+ and O2+) in the storm time ring current, *Geophys. Res. Lett.*, 13(7), 632-635. https://doi.org/10.1029/GL013i007p00632

[34] Kosch, M. J., Ogawa, Y., Rietveld, M. T., Nozawa, S., & Fujii R. (2010). An analysis of pump-induced artificial ionospheric ion upwelling at EISCAT, *J. Geophys. Res.*, 115(A12), A12317. https://doi.org/10.1029/2010JA015854

[35] Kulsrud, R.M. (2001). Magnetic reconnection: Sweet-Parker versus Petschek. *Earth Planet Sp53*, 417–422. https://doi.org/10.1186/BF03353251

[36] Lin., M.-Y., & Ilie, R. (2022). A Review of Observations of Molecular Ions in the Earth's Magnetosphere-Ionosphere System. *Front. Astron. Space Sci*., 8:745357. https://doi.org/10.3389/fspas.2021.745357

[37] Lehtinen, M. S., & Huuskonen, A. (1996). General incoherent scatter analysis and GUISDAP, *Journal of Atmospheric and Terrestrial Physics*, *58(1–4)*, 435-452. https://doi.org/10.1016/0021-9169(95)00047-X

[38] Liu, Chao, Horwitz, J. L., & Richard, P.G. (1995). Effects of frictional ion heating and soft-electron precipitation on high-latitude F-region upflows, *Geophys. Res. Lett*., *22(20)*, 2713-2716. https://doi.org/10.1029/95GL02551

[39] Liu, H., Schlegel, K., & Ma, S.-Y. (2000). Combined ESR and EISCAT observations of the dayside polar cap and auroral oval during the May 15, 1997 storm, *Ann. Geophys*., 18, 1067–1072. https://doi.org/10.1007/s00585-000-1067-x

[40] Liu, H., & Lu, G. (2004). Velocity shear-related ion upflow in the low-altitude ionosphere. *Ann. Geophys*., 22(4), 1149–1153. https://doi.org/10.5194/angeo-22-1149-2004

[41] Liu, L., Zhao, B., Wan, W., Ning, B., Zhang, M.-L., & He, M. (2009). Seasonal variations of the ionospheric electron densities retrieved from constellation observing system for meteorology, ionosphere, and climate mission radio occultation measurements. *J. Geophys. Res.*, 114, A02302. https://doi.org/10.1029/2008JA013819

[42] Liu, J., Lyons, L. R., Wang, C.-P., Ma, Y., Strangeway, R. J., Zhang, Y., et al. (2021). Embedded Regions 1 and 2 field-aligned currents: Newly recognized from low-altitude spacecraft observations. *J. Geophys. Res. Space Physics*, 126, e2021JA029207. https://doi.org/10.1029/2021JA029207

[43] Mcllwain, C. E. (1961). Coordinates for mapping the distribution of magnetically trapped particles, J. Geophys. Res., 66(11), 3681–3691. https://doi.org/10.1029/JZ066i011p03681

[44] Milan, S. E., Clausen, L. B. N., Coxon, J. C., Carter, J. A., Walach, M.-T., Laundal, K., et al. (2017). Overview of solar wind-magnetosphere-ionosphere-atmosphere coupling and the generation of magnetospheric currents. *Space Science Reviews*, 206, 547– 573. https://doi.org/10.1007/s11214-017-0333-0

[45] Miyoshi, Y., Hori, T., Shoji, M., Teramoto, M., Chang, T.-F., Segawa, T., et al. (2018a). The ERG Science Center, Earth, Planets and Space, 70:96. https://doi.org/10.1186/s40623-018-0867-8

[46] Miyoshi, Y., Shinohara, I. & Jun, C.-W. (2018b), updated daily. The Level-2 orbit data of Exploration of energization and Radiation in Geospace (ERG) Arase satellite, Version v03. ERG Science Center, Institute for Space-Earth Environmental Research, Nagoya University. https://doi.org/10.34515/DATA.ERG-12000 Accessed 2020-11-18.

[47] Miyoshi, Y., Shinohara, I., Takashima, T., Asamura, K., Higashio, N., Mitani, T., et al. (2018c). Geospace Exploration Project ERG, *Earth, Planets and Space*, 70:101. https://doi.org/10.1186/s40623-018-0862-0

[48] Nose´, M., Taguchi, S., Hosokawa, K., Christon, S. P., McEntire, R. W., Moore, T. E., & Collier, M. R. (2005). Overwhelming O+ contribution to the plasma sheet energy density during the October 2003 superstorm: Geotail/EPIC and IMAGE/LENA observations, *J. Geophys. Res. Space Physics*, 110(A9), A09S24. https://doi.org/10.1029/2004JA010930

[49] Nygrén, T. (1996). Introduction to incoherent scatter measurements. *Invers Publications*

[50] Obana, Y., Maruyama, N., Shinbori, A., Hashimoto K. K., Fedrizzi. M., Nosé, M., et al. (2019). Response of the Ionosphere-Plasmasphere Coupling to the September 2017 Storm: What Erodes the Plasmasphere so Severely?, *Space Weather*, *17(6)*, 861–876. https://doi.org/10.1029/2019SW002168

[51] Ogawa, Y., Seki, K., Hirahara, M., Asamura, K., Sakanoi, T., Buchert, S. C., et al. (2008). Coordinated EISCAT Svalbard radar and Reimei satellite observations of ion upflows and suprathermal ions, *J. Geophys. Res.*, 113(A5), A05306. https://doi.org/10.1029/2007JA012791

[52] Ogawa, Y., Buchert, S. C., Fujii, R., Nozawa, S., & van Eyken, A., P. (2009). Characteristics of ion upflow and downflow observed with the European Incoherent Scatter Svalbard radar, *J. Geophys. Res.*, *114(A5)*, A05305. https://doi.org/10.1029/2008JA013817

[53] Ogawa, Y., Sawatsubashi, M., Buchert, S. C., Hosokawa, K., Taguchi, S., Nozawa, S., et al. (2013). Relationship between auroral substorm and ion upflow in the nightside polar ionosphere, *J. Geophys. Res. Space Physics*, *118(11)*, 7426–7437. https://doi.org/10.1002/2013JA018965

[54] Ogawa, Y., Seki, K., Keika, K., & Ebihara, Y. (2019). Characteristics of CME- and CIR-driven ion upflows in the polar ionosphere, *J. Geophys. Res. Space Physics*, 124, 3637–3649. https://doi.org/ 10.1029/2018JA025870

[55] Peterson, W. K., Abe, T., Fukunishi, H., Greffen, M. J., Hayakawa, H., Kasahara, Y., et al. (1994). On the sources of energization of molecular ions at ionospheric altitudes, *J. Geophys. Res.*, 99(A12), 23257-23274. https://doi.org/10.1029/94JA01738

[56] Picone, J. M., Hedin, A. E., Drob, D. P., & Aikin A. C. (2002). NRLMSISE-00 empirical model of the atmosphere: Statistical comparisons and scientific issues, *J. Geophys. Res.*, *107(A12)*, 1468. https://doi.org/10.1029/2002JA009430.

[57] Pollock, C. J., C:son-Brandt, P., Burch, J., Henderson, M. G., Jahn, J.-M., McComas, D.J., et al. The Role and Contributions of Energetic Neutral Atom (ENA) Imaging in Magnetospheric Substorm Research. *Space Science Reviews* 109, 155–182 (2003). https://doi.org/10.1023/B:SPAC.0000007518.93331.d5

[58] Remya, B., R. V. Reddy, B. T. Tsurutani, G. S. Lakhina, & E. Echer (2013), Ion temperature anisotropy instabilities in planetary magnetosheaths, *J. Geophys. Res. Space Physics*, 118, 785–793, https://doi.org/10.1002/jgra.50091

[59] Schunk, R. W. (1977). Mathematical structure of transportequations for multispecies flows, *Rev. Geophys. Space Phys.*, 15, 429-445. https://doi.org/10.1029/RG015i004p00429

[60] Schunk, R. W., & Nagy, A. F. (2009). *Ionospheres: Physics, Plasma Physics, and Chemistry.* Cambridge, UK: Cambridge Univ. Express.

[61] Strangeway, R. J. (2012). The equivalence of Joule dissipation and frictional heating in the collisional ionosphere, *J. Geophys. Res.*, *117(A2)*, A02310. https://doi.org/10.1029/2011JA017302

[62] Seki, K., Keika, K., Kasahara, S., Yokota, S., Hori, T., Asamura, K., et al. (2019). Statistical Properties of Molecular Ions in the Ring Current Observed by the Arase (ERG) Satellite, *Geophys. Res. Lett.*, 46, 8643-8651. https://doi.org/10.1029/2019GL084163

[63] Sergeev, V. A. (1990). Polar cap and cusp boundaries at day and night. *J. Geomag. Geoelectr.,* 42, 683–695. https://doi.org/10.5636/jgg.42.683

[64] Sergeev, V. A., Pulkkinen, T. I., & Pellinen, R. J. (1996). Coupled-mode scenario for the magnetospheric dynamics. *J. Geophys. Res.*, 101(A6), 13047–13066. https://doi.org/10.1029/95JA03192

[65] Shelly., E., G., Johnson, R. G., & Sharp, R. D. (1972). Satellite observations of energetic heavy ions during a geomagnetic storm. *J. Geophys. Res*., 77(31), 6104-6110. https://doi.org/10.1029/JA077i031p06104

[66] Takada, M., Seki, K., Ogawa, Y., Keika, K., Kasahara, S., Yokota, S., et al. (2021). Low-altitude ion upflow observed by EISCAT and its effects on supply of molecular ions in the ring current detected by Arase (ERG). *J. Geophys. Res. Space Physics*, 126, e2020JA028951. https://doi.org/10.1029/2020JA028951

[67] Terada, N., Shinagawa, H., Tanaka, T., Murawski, K., & Terada, K. (2009). A three-dimensional, multispecies, comprehensive MHD model of the solar wind interaction with the planet Venus, *J. Geophys. Res.*, *114(A9)*, A09208. https://doi.org/10.1029/2008JA013937

[68] Thébault, E., Finlay, C. C., Beggan, C.D., et al. (2015). International Geomagnetic Reference Field: the 12th generation, *Earth Planet and Space,* 67:79. https://doi.org/10.1186/s40623-015-0228-9

[69] Wahlund, J.-E., Opgenoorth, H. J., Haggstrom, I., Winser, K. J., & Jones, G. O. L. (1992). EISCAT observations of topside ionospheric ion outflows during auroral activity: Revisited, *J. Geophys. Res. Space Physics*, *97(A3)*, 3019–3037. https://doi.org/10.1029/91JA02438

[70] Weimer, D. R. (2005). Improved ionospheric electrodynamic models and application to calculating Joule heating rates. *J. Geophys. Res.*,110, A05306. https://doi.org/10.1029/2004JA010884

[71] Wilson, G. R., & Craven, P. (1999). Molecular ion upflow in the cleft ion fountain, *J. Geophys. Res.*, *104(A3)*, 4437-4446. https://doi.org/10.1029/1998JA900070

[72] Woch, J., & Lundin, R. (1992). Magnetosheath plasma precipitation in the polar cusp and its control by the interplanetary magnetic field. *J. Geophys. Res*, 97(A2), 1421– 1430. https://doi.org/10.1029/91ja02487

[73] Wurz, P. (2005). Solar wind composition, *Dyn. Sun*, 600,

[74] Xiong, C., Lühr, H., Wang, H., & Johnsen, M. G. (2014), Determining the boundaries of the auroral oval from CHAMP field-aligned current signatures – Part 1, *Ann. Geophys*., 32, 609–622. https://doi.org/10.5194/angeo-32-609-2014

[75] Yamazaki, Y., M. J. Kosch, & Y. Ogawa (2017), Average field-aligned ion velocity over the EISCAT radars, *J. Geophys. Res. Space Physics*, 122, 5630–5642, https://doi.org/10.1002/2017JA023974

[76] Yau, A. W., & André, M. (1997). Sources of ion outflow in the high latitude ionosphere, *Space Sci. Rev, 80*, 1-25. https://doi.org/10.1023/A:1004947203046

[77] Yokota, S., Kasahara, S., Mitani, T., Asamura, K., Hirahara, M., Takashima, T., et al. (2017). Medium-energy particle experiments–ion mass analyzer (MEP-i) onboard ERG (Arase), *Earth Planets Space*, 69:172. https://doi.org/:10.1186/s40623-017-0754-8

[78] Yokota, S., Kasahara, S., Hori, T., Keika, K., Miyoshi, Y., & Shinohara, I. (2019), updated daily. The MEP-i instrument Level-2 TOF mode data of Exploration of energization and Radiation in Geospace (ERG) Arase satellite, Version v01_01.

ERG Science Center, Institute for Space-Earth Environmental Research, Nagoya University. https://doi.org/10.34515/DATA.ERG-03002 Accessed 2020-11-18.

[79] Zettergren, M., Semeter, J., Heinselman, C., & Diaz, M. (2011). Incoherent scatter radar estimation of F region ionospheric composition during frictional heating events. *J. Geophys. Res.*, 116, A01318. https://doi.org/10.1029/2010JA016035

[80] Zhang, Q., Liu, Y. C.-M., Zhang, Q.-H., Xing, Z.-Y., Wang, Y., & Ma, Y.-Z. (2020). Statistical study of ion upflow associated with subauroral polarization streams (SAPS) at substorm time. *J. Geophys. Res. Space Physics*, 125, e2019JA027163. https://doi.org/10.1029/2019JA027163